이학박사 학위논문

탄소점 하이브리드 나노물질 및 산화구리 복합체의 제조와 응용

Fabrication and Application of Cdots-Based Hybrid Nanomaterials and Cu_2O/CuO composites

2019년 8월

서울대학교 대학원

화학부 물리화학 전공

최 다 연

A ph. D. Dissertation

Fabrication and Application of Cdots-Based Hybrid Nanomaterials and Cu_2O/CuO composites

By Dayeon Choi

Supervisor: Professor Du-Jeon Jang

Major: Physical Chemistry

Department of Chemistry

Graduate School of Seoul National University

August 2019

Abstract of Dissertation

In this dissertation, facile synthesis and application of Cdots based hybrid nanomaterials are mainly discussed. Cdots have been synthesized facilely by hydrothermal method and incorporated with semiconductor nanomaterials, such as TiO_2 and SiO_2, to produce hybrid nanostructures. The incorporated Cdots can act as photosensitizers for photocatalytic systems and also act as electron donors for photodeposition systems. Furthermore, Cdots played a role as a phosphor in fluoremetric detection systems. In addition, the morphology-controlled Cu_2O/CuO composites have been prepared and the morphology-dependent catalytic properties of the prepared composites have been investigated for potential applications. Brief overviews of the Chapter 1-5 mentioned in this dissertation are given below.

Chapter 1 reports a brief overview of nanosized materials having unique optical properties depending on their sizes. Nanomaterials show markedly different chemical and physical properties from those bulk size materials. Especially, the properties of carbon nanodots as well as their fabrication and application have been described.

Chapter 2 presents that carbon quantum dots (CQDs)-decorated TiO_2 (C/TiO_2) nanocomposites with various dosages of CQDs having photocatalytic activities of

Cr(VI) reduction have been fabricated via hydrothermal process. Under visible-light irradiation, the photocatalytic activities of Cr(VI) reduction via C/TiO_2 nanocomposites have been monitored and found to depend highly on the dosage of CQDs. When CQDs are excited by visible light, photo-generated electrons transfer from CQDs into the conduction band of TiO_2 and the transferred electrons are subsequently captured by Cr(VI) ions, reducing Cr(VI) into Cr(III). CQDs act as sensitizers to provide visible-light response to the TiO_2 nanoparticles of C/TiO_2 dyade structures, leading to the highly efficient photocatalytic reduction of Cr(VI). Our as-prepared C/TiO_2 nanocomposites are applicable in an inexpensive way to treat wastewater by utilizing solar energy without employing electron donors.

Chapter 3 described that carbon dots (Cdots) were prepared on SiO_2 nanospheres by a hydrothermal method to produce Cdots-SiO_2 nanocomposites, then gold nanoparticles were directly photodeposited on the surfaces of silica nanospheres to produce Au/Cdots-SiO_2 nanocomposites finally. Under light irradiation, the photoinduced electrons of Cdots could reduce the gold precursor of $AuCl_4^-$ on the surfaces of SiO_2 nanospheres; Cdots could act as electron donors and reaction sites simultaneously. Overall, the adoption of Cdots as electron donors and nucleation sites has been proved to be an efficient way to prepare metal-semiconductor hybrids, where the semiconductor may be photoactive or not.

Chapter 4 described that gold nanoparticles have been facilely prepared on Cdots/SiO_2 nanocomposites by a photodeposition method to fabricate Au-C/SiO_2 nanocomposites. Photodeposited gold nanoparticles have shown commendable peroxidase-like activity, so they can oxidize 3,3',5,5'-tetramethylbenzidine effectually in the presence of H_2O_2; Au-C/SiO_2 nanocomposites can be used for the colorimetric detection of H_2O_2 . In addition, Au-C/SiO_2 nanocomposites also can be used for the fluorometric detection of H_2O_2 because photodeposited gold nanoparticles act as light absorbers of Cdots. Taken together, H_2O_2 can be detected quantitatively via dual-signal modes, colorimetric and fluorometric methods, with Au-C/SiO_2 nanocomposites. Thus, it is suggested that our Au-C/SiO_2 nanocomposites have a wide range of applications in bio-detection, catalysis, and clinical diagnostics.

Chapter 5 present that diverse morphologies of Cu_2O/CuO composites having good catalytic properties for the reduction of 4-nitrophenol in the presence of $NaBH_4$ have been controlled facilely by adjusting the concentrations of NaOH during the wet etching of Cu_2O cubes. The catalytic activity of Cu_2O/CuO composites is found to depend highly on their morphologies. Regarding to the highest catalytic activity of the composites with cavities surrounded by CuO flakes, confinement effect is considered to expedite electron transfer from BH_4^- to the dye molecule enormously by reducing the activation energy largely. Thus, it is

suggested that Cu_2O/CuO may be applied to treat wastewater in an inexpensive way without employing commonly used noble-metal catalysts.

Keywords: Carbon dots, Gold nanoparticles, Hybrid nanostructures, Photocatalysts, Photodeposition

Student Number: 2013-22943

Table of Contents

List of Figures and Tables

Figure 2-10 Absorption spectrum of as prepared CQDs dispersed in water.

Figure 2-11 Diffuse-reflectance spectra of C/TiO_2 nanocomposites decorated with respectively indicated weight percentages of CQDs. The 3% (mix) and 3% indicate physically mixed and hydrothermally treated 3% C/TiO_2 nanocomposites, respectively.

Figure 2-12 Emission spectrum of as-prepared CQDs (yellow circles) dispersed in ethanol with excitation at 266 nm. The solid lines correspond to the deconvoluted Gaussian curves (violet, blue, green, and red) and the integral of the fitted curves (black).

Figure 2-13 Emission spectra of C/TiO_2 nanocomposites decorated with respectively indicated weight percentages of CQDs. 0.50 mg of each sample was dispersed in 1.0 mL of ethanol and excited at 266.

Figure 2-14 Maximum-normalized emission spectra of as-prepared CQDs (black), 3% (mix) C/TiO_2 nanocomposites (purple), and 3% C/TiO_2 nanocomposites (green) dispersed in ethanol with excitation at 266 nm.

Figure 2-15 PL decay profiles of C/TiO_2 nanocomposites decorated with respectively indicated weight percentages of CQDs. The samples were dispersed in ethanol, excited at 266 nm, and monitored at 450 nm.

Figure 2-16 Time-dependent concentration changes of aqueous Cr(VI) via indicated photocatalysts.

Figure 2-17 First-order kinetic profiles (a) and reduction rate constants (b) of Cr(VI) via indicated catalysts under visible light.

and (e) TMB + H_2O_2.

Figure 4-5 First-order kinetics, absorbance vs t, for the catalytic oxidation of TMB varied with (a) pH values, (b) temperatures, (c) catalyst amounts, and (d) TMB concentrations.

Figure 4-6 Relative rate constants for the peroxidase-like activity of Au-C/SiO_2 nanocomposites, depending on (a) pH values, (b) temperatures, (c) catalysts amounts, and (d) TMB concentrations.

Figure 4-7 (a) First-order kinetics, absorbance vs t, for the catalytic oxidation of TMB under the indicated concentrations of H_2O_2; the rate constant, k, of the reaction has been obtained from the slope of the first-order kinetics. (b) Relative rate constants dependent on H_2O_2 concentrations. The photograph shows the representative colors of TMB_{ox} developed under the indicated concentrations in μM of H_2O_2.

Figure 4-8 Steady-state kinetic analysis utilizing (a,b) the Michaelis-Menton model and (c,d) the Lineweaver-Burk double-reciprocal model for Au-C/SiO_2 nanocomposites with (a,c) H_2O_2 and (b,d) TMB.

Figure 4-9 Influence of H_2O_2 concentrations on the fluorescence-based detection of H_2O_2 in the presence of TMB and Au-C/SiO_2 nanocomposites.

Figure 4-10 Emission spectra of Au-C/SiO_2 nanocomposites etched (red) with and (black) without CTAB.

Figure 5-1 Schematic for the synthesis of CuO/Cu_2O composites via the simple top-down wet etching of Cu2O cubes.

Figure 5-2 TEM images of pristine Cu_2O cubes (a) and CuO/Cu_2O composites prepared at respectively indicated concentrations of NaOH(aq) (b-f). Each scale bar indicates 1 μm.

Figure 5-3 FE-SEM images of pristine Cu_2O cubes (a), and CuO/Cu_2O composites prepared at respectively indicated concentrations of NaOH(aq) (b-f). Each scale bar indicates 1 μm.

Figure 5-4 TEM images of CuO/Cu_2O(0.3 M) composites prepared via the wet etching of Cu_2O cubes for indicated durations.

Figure 5-5 HRTEM image (a), enlarged HRTEM image (b), FFT pattern (c), and SAED pattern (d) of a CuO/Cu_2O(0.3 M) composite.

Figure 5-6 XRD patterns of pristine Cu_2O cubes (a) and CuO/Cu_2O(0.1 M) (b), CuO/Cu_2O(0.2 M) (c), CuO/Cu_2O(0.3 M) (d), and CuO/Cu_2O(0.4 M) (e) composites. The standard diffraction patterns of cubic Cu_2O and monoclinic CuO are also shown for comparison.

Figure 5-7 Cu 2p XPS curves of pristine Cu_2O cubes (red) and CuO/Cu_2O(0.3 M) composites (green).

Figure 5-8 Deconvoluted Cu 2p3/2 XPS curves of pristine Cu_2O cubes (a), and CuO/Cu_2O(0.3 M) composites

Figure 5-9 Absorption spectra at 30 ºC of $NaBH_0$-added aqueous 4-NP solutions, measured at elapsed times indicated in the units of min after adding aqueous colloidal solutions of pristine Cu_2O cubes (a) and CuO/Cu_2O(0.3 M) composites (b).

Figure 5-10 ln(A/A0) vs t for the catalytic reduction of 80 µM 4-NP(aq) in the presence of 2.0 mM $NaBH_4$ at 30 ºC, via pristine Cu_2O cubes (squares) and CuO/Cu_2O composites prepared at NaOH concentrations of 0.1 M (crosses), 0.2 M (circles), 0.3 M (triangles), and 0.4 M (diamonds).

Figure 5-11 First-order kinetics, ln(A/A0) vs t, for the catalytic reduction of 80 µM 4-NP(aq) in the presence of 2.0 mM $NaBH_4$ at temperatures indicated in ºC via pristine Cu_2O cubes (a) and CuO/Cu_2O(0.3 M) composites.

Figure 5-12 Arrhenius plots for the catalytic reduction reaction of 80 µM 4-NP(aq) in the presence of 2.0 mM $NaBH_4$ via pristine Cu_2O cubes (squares) and CuO/Cu_2O composites prepared at NaOH concentrations of 0.1 M (crosses), 0.2 M (circles), 0.3 M (triangles), and 0.4 M (diamonds) (a), and compensation law plot of the activation energies and the frequency factors obtained from the Arrhenius plots (b).

Figure 5-13 Eyring plot for the catalytic reduction reactions of 80 µM 4-NP(aq) catalyzed via pristine Cu_2O cubes (closed) and CuO/Cu_2O(0.3 M) composites (open) in the presence of NaBH4.

Figure 5-14 Schematically proposed mechanism for the catalytic reduction of 4-NP via CuO/Cu_2O composites in the presence of $NaBH_4$.

Table 5-1 Crystallite sizes (D) and plane distances (d) in the units of nm, calculated from XRD patterns

Table 5-2 Rate constants (k) at 30 ºC, activation energies (E_a), frequency factors (A), activation enthalpies ($\Delta H‡$), and activation entropies ($\Delta S‡$) for the catalytic reduction of 4-NP

Chapter 1. General Introduction

1.1 Properties of nanomaterials

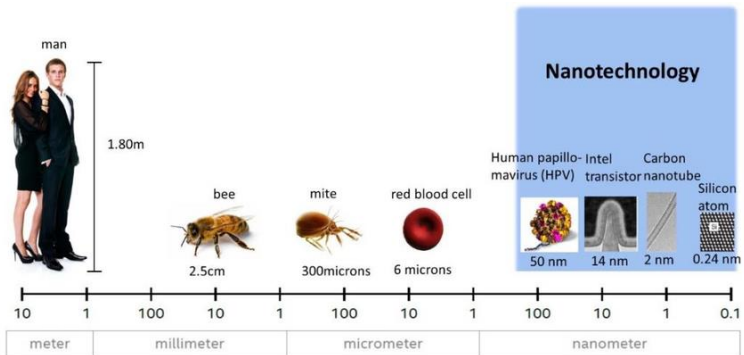

Figure 1-1 Scale of dimensions from meter down to nanometer. Reproduced from ref. 1.

The "Nano" term is typically used to refer to objects having 10^{-9} m length scale (Figure 1-1). With the great growth of interest in the field of nanochemistry, the study of nanosized semiconductors has become increasingly important over a few decades due to their unique optical and electrical properties compared with the respective ones of bulk semiconductors. The bulk properties of macro-scale materials could often change dramatically when their dimensions are aggressively scale down. In nanosized materials, completely different phenomena are observed; their electrical, mechanical, optical and chemical properties are changed, thus many researchers call these nanomaterials "wonder materials".[1] There are typically two main size effects: quantum-confinement effect and the fraction of atoms at the surfaces.

Quantum-confinement effect

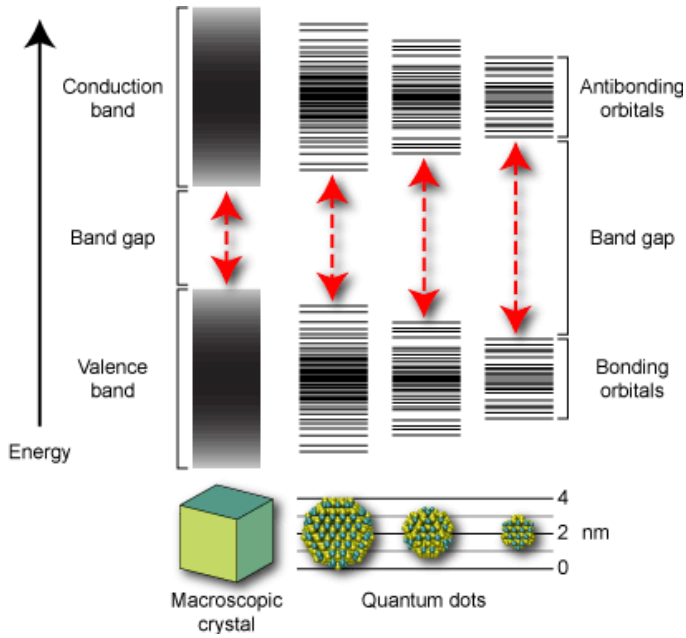

Figure 1-2 Quantum size effect in nanomaterials.

Nanomaterials have shown different properties from those observed in bulk matter. In intermediate size rage between molecular and bulk matter, continuous energy bands of solids become discrete and their energy preparations display an analytic dependence on the spatial dimension of the materials. This is illustrated conceptually in Figure 1-2, which expresses the transformation of energy band structures of valence and conduction bands in macroscopic semiconductors from continuous to discrete to individual in bulk, which is called as quantum-confined

effects. Quantum confinement effects can be observed when the diameter of a materials have similar magnitude as the de Broglie wavelength of the electron wave function. As the length of confining quantum well decreases and reach a certain limit, called the exciton Bohr radius, the energy spectrum, become discrete, exhibiting that their electronic and optical properties deviate substantially from those of bulk materials.

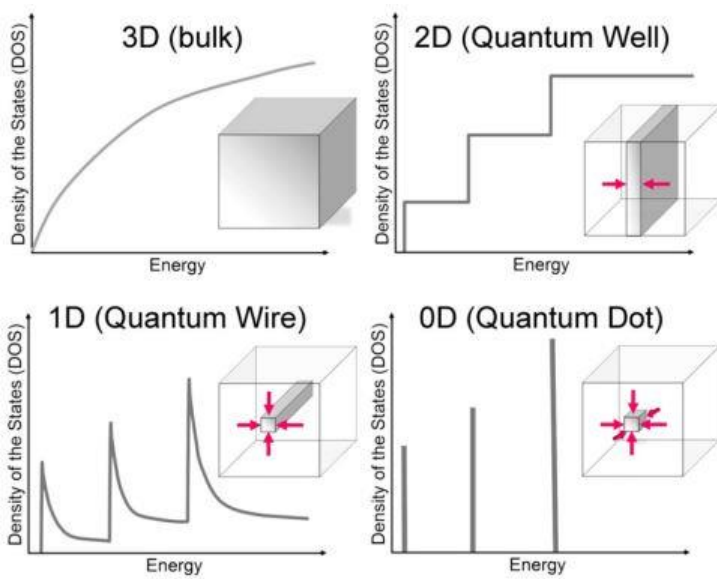

Figure 1-3 Electronic DOS for a bulk 3D crystalline material, a 2D QW, a 1D NW or NT, and 0D QD. The insets report a cartoon showing the corresponding spatial confinement: confinement directions are directions are defined by arrows. Reproduced from ref. 2.

The most typical demonstration of the size-dependent characteristics of nanocrystals is quantum dots (QDs) whose continuous fluorescent emission convers the entire visible spectrum as a function of their sizes. Especially, quantum-confinement in semiconductors results also from the direction-dependent quantum confinement of electrons and holes as bound pairs known as excitons or as independently acting ‘wave-particles’, the representative scheme is shown in Figure 1-3. The exciton Bohr radius provides as approximate dimension for the onset of quantum-confinement effects. When an electron-hole pair is squeezed into a nanocrystal within the bulk exciton Bohr radius, the effective bandgap of the semiconductor increases. The smaller the nanocrystals, the larger the effective bandgap, and the greater the energy of optical emission resulting from effective electron-hole recombination.

Surface effects

The characteristic feature of nanomaterials is the large surface-to-volume ratios. One-dimensional and two-dimensional materials have a relatively large surface area when compared to the same mass of materials produced in a large form. For example, a single sugar cube with edges 1 cm in length can be divided into 10^{21} sugar nanocubes with edges 1 nm in length. The number of individual cubes and their total surface area increases dramatically; the total surface area of 6000 m^2 for the 10^{21} nanocubes is comparable to the area of a football game field of 7000 m^2.

Namely, a particles having size of 30 nm has 5% of its atoms on its surface, at 10 nm 20% of its atoms and at 3 nm 50% of its atoms on its surface. Nanoparticles are strongly influenced by their surface areas, unsaturated bonding sites and unoccupied coordination sites on their surfaces. For this reason, the surface atoms generally exhibit the highest affinity to form bonds to adsorbate molecules, followed by the edge and the in-plane surface atom, a fact that is of utmost importance for the catalytic activity. Therefore, the increasing exposed surface atoms are directly affected to properties of nanoparticles.

1.2 Carbon dots

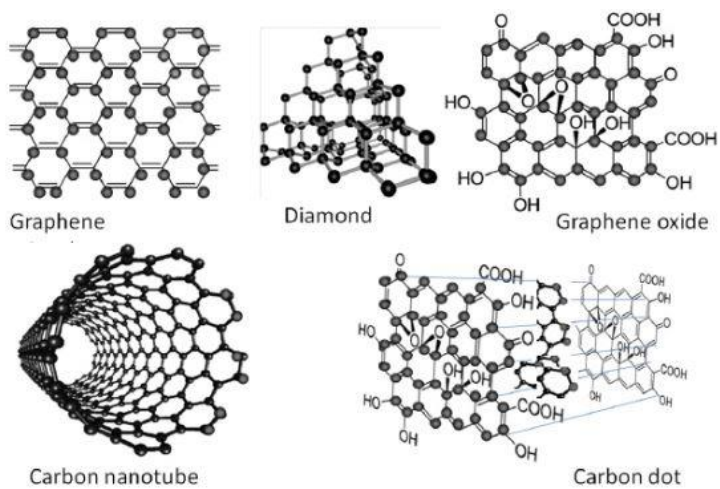

Figure 1-4 The schematic structures of nanoscale carbon materials. Reproduced from ref. 3.

The discovery and investigation of unusual properties of pure carbon realized in smart nanoscale materials attracts increasing attention in the scientific world. This has resulted in many publications with an exponential growth in recent years. Basic graphene 2D and diamond 3D structures together with graphene oxides Go-dots, carbon nanotubes and carbon dots are schematically presented in Figure 1-4. 2D graphene and 3D diamond are basically non-fluorescent. Graphene emission appears on reduction of its size to several nanometers and it is enhanced by attachment of polar groups to its edges. In graphene oxide the polar groups are bound throughout the plane, disrupting the π-electronic conjugation within the plane and forming elements of structure that are fluorescence emitters.[3] Short carbon nanotubes attain the same fluorescence properties as graphene oxides after attachment of polar groups. Carbon dots are composed of graphene and graphene oxide sheets fused by diamond-like insertions and containing amorphous structural elements.[3] Among them, fluorescent Carbon dots are versatile and less defined nanocarbon materials. They have attracted many researchers just because of their simple syntheses achievable by many approaches from a variety of starting materials.

1.2.1. Fabrication of carbon dots

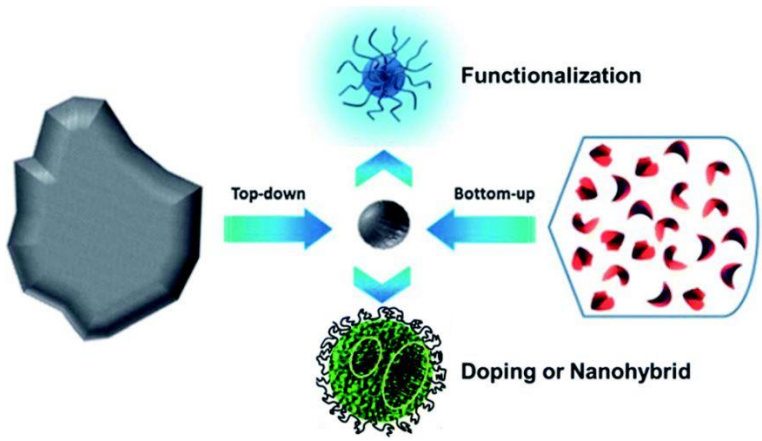

Figure 1-5 Schematic illustration of Carbon dots preparing via "top-down" and "bottom-up" approaches, and modification including functionalizing. Reproduced from ref. 4.

Many methods have been proposed to prepare carbon dots during the last decade, which can be roughly classified into "Top-down" and "Bottom-up" approaches, and they can be modified during preparation or post-treatment (Figure 1-5). Three problems facing carbon dots preparation need to be noticed: (1) carbonaceous aggregation during carbonization, which can be avoided by using electrochemical synthesis, confined pyrolysis or solution chemistry methods, (2) size control and uniformity, which is important for uniform properties and mechanistic study, and can be optimized *via* post-treatment, such as gel electrophoresis, centrifugation, and dialysis and (3) surface properties that are critical for solubility and selected applications, which can be tuned

during preparation or post-treatment.[4]

Top-down synthetic routes

Electrochemical carbonization. Electrochemical soaking is a powerful method to prepare carbon dots using various bulk carbon materials as precursors.[5,6] However, there are only a few reports about electrochemically carbonizing small molecules to carbon dots. The sizes and graphitization degrees of these carbon dots increase with the increasing applied potential. The resultant carbon dots with amorphous core exhibited excellent excitation- and size-dependent PL properties without complicated purification and passivation procedures.

Laser ablation. In this process, a carbon target in the presence of water vapor with an inert gas as a carrier under high temperature and pressure is irradiated with laser beam.[7,8] In a typical procedure, carbon precursor is dispersed in some solvent by ultrasonication, and the suspension is dropped into a glass cell for laser irradiation. Advantages of the laser irradiation technique are that it is a fast synthetic route and environmentally friendly approach for the synthesis of carbon quantum dots, but this method is economically not favorable, skilled personal is necessary to conduct the synthesis and post synthetic process such as surface passivation is necessary to impart fluorescent nature

Bottom-up synthetic routes

Microwave pyrolysis. This method involves the microwave irradiation of organic compounds in presence of reaction medium. This is a rapid and low-cost method to prepare carbon quantum dots, and in general, sugar moieties were used as a carbon source and polymeric oligomers as reaction media and amine molecules play a role of nitrogen dopants and surface-passivating agents in order to improve the emission quantum yields. Advantages of microwave pyrolysis route are as follows: simple, rapid and efficient method for the synthesis of carbon quantum dots. At the same time, there are few limitations: being costly and the presence of harmful microwave radiation, which is to be handled with precautions.[9]

Hydrothermal/solvothermal synthesis. This is the most popular and facile method for the synthesis of fluorescent carbon quantum dots in which various sources such as chemical as well as green precursor can be used for the synthesis of carbon quantum dots.[10-12] This technique involves a solution of organic precursor in the presence of either water or some organic solvent sealed in an autoclave and reacted at high temperature. After complete carbonization, it is autoclaved to allow cooling down to room temperature naturally, and the products can be extracted with an organic solvent. By adopting this technique, one can synthesis both hydrophilic and hydrophobic fluorescent carbon quantum dots simply by selecting the appropriate precursors.

Compared with other routes, the hydrothermal carbonization process has some of the advantages such as low toxicological impact of materials and processes, the use of renewable resources, facile instrumentation techniques and high atom economy. This method is cost effective, ecofriendly and nontoxic. Using this technique, large-scale production is possible and reaction conditions such as time and temperature are adjustable. Post synthetic surface passivation is not necessary. The only limitation of this method is poor control over particle sizes.

1.2.2. Optical properties of carbon dots

Absorption

Carbon dots typically show optical absorption in the UV region with a tail extending to the visible range (Figure 1-6). There may be some absorption shoulders attributed to the π–π* transition of the C=C bonds, the n–π* transition of C=O bonds and other oxygen carbon-containing functional groups.[14]

Fluorescence

One of the most fascinating features of carbon dots, both from fundamental and application-oriented perspectives, is their PL. In most cases of early study, one unique feature of the PL of carbon dots was the clear λ_{ex} dependence of the emission

wavelength and intensity. Whether this occurs because of optical selection of differently sized nanoparticles (quantum effect) and/or different emissive traps on the carbon dots surface or another mechanism is currently unresolved.[15] Although there have been many efforts focused on the physicochemical properties of carbon dots, the origin of the observed optoelectronic behavior is a topic of discussion to date.

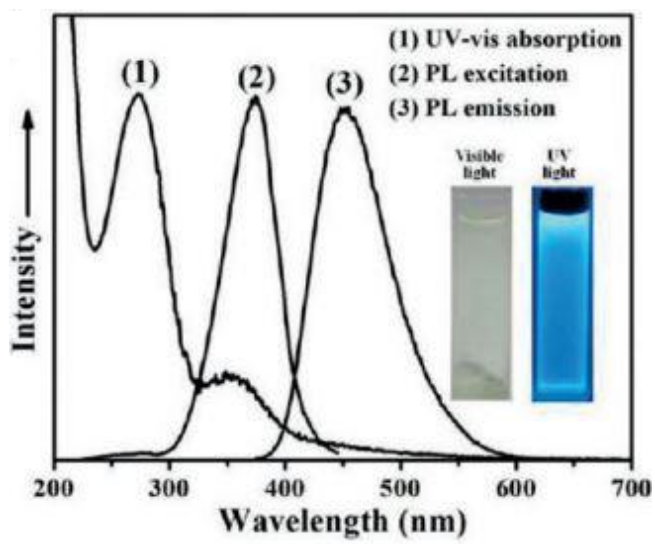

Figure 1-6 Absorption, excitation, and emission bands of carbon quantum dots. Reproduced from ref. 13.

1.2.3. Application of carbon dots

Bio-applications

As fluorescent nanomaterials with biocompatibility and low bio toxicity, Carbon dots show great potential for fluorescent bioimaging,[16] and multimodal bio imaging of cells and tissue.[17] Carbon dots have been also used as biosensor carriers for their high solubility in water, flexibility in surface modification, nontoxicity, excitation-dependent multicolor emission, excellent biocompatibility, good cell permeability, and high photostability. The carbon dots -based biosensors can be used for visual monitoring of glucose,[18] cellular copper,[19] and phosphate.[20]

Chemical sensing

An interesting application of carbon dots is in the field of chemical sensing. Carbon dots were used for chemical sensing due to their low toxicity, water solubility, high photostability and superior chemical stability. One of the first attempts of utilizing carbon dots in chemical sensing is the selective detection of Hg^{2+} in aqueous solutions and live cells.[21] Goncalves and colleagues demonstrated that the fluorescence emissions of both carbon dots solution and carbon dots immobilized in sol–gel are sensitive to the presence of Hg^{2+}.[22,23] Other applications of CQDs in chemical sensing included the

detections of Cu^{2+},[24] Fe^{3+},[25] Pb^{2+},[26] and Cr(VI).[27] Similar to the Hg^{2+} sensing, most of the procedures proposed are based on the above-mentioned fluorescence quenching by the metal ions.

Photocatalysis

In recent years, photocatalytic processes have gained tremendous momentum as greener alternatives in organic synthesis. Interest in photocatalysis has been motivated in part by the realization that sunlight is effectively an inexhaustible energy source. However, the high energy of UV and short wavelength visible light may adversely damage organic compounds. The demonstrated capability of harnessing long wavelength light and energy exchange with solution species of carbon dots offers an excellent opportunity for their use as photocatalysts in organic synthesis. Indeed, a recent study has indicated that smaller carbon dots (1–4 nm) are effective NIR light-driven photocatalysts for selective oxidation of alcohols to benzaldehydes with good conversion efficiency (92%) and selectivity (100%).[28] Apart from harvesting visible light and converting it to shorter wavelength light through up-conversion, it is believed that the carbon dots in the nanocomposites facilitate the transfer of electrons from semiconductors and the electrons can be shuttled freely along the conducting paths of the carbon dots, allowing charge separation, stabilization and hindering recombination,

thereby generating long-lived holes on the semiconductor surface.[29] The longer-lived holes then account for the much enhanced photocatalytic activity of the nanocomposites.

1.3. Photocatalysis and photodeposition

Photocatalysis

In chemistry, photocatalysis is the acceleration of a photoreaction in the presence of a catalyst. In catalysed photolysis, light is absorbed by an adsorbed substrate. In photogenerated catalysis, the photocatalytic activity depends on the ability of the catalyst to create electron–hole pairs, which generate free radicals able to undergo secondary reactions. The earliest mention of photocatalysis dates back to 1911, when German chemist Dr. Alexander Eibner integrated the concept in his research of the illumination of zinc oxide on the bleaching of the dark blue pigment, Prussian blue. There are two types of photocatalysis, homogeneous photocatalysis and heterogeneous photocatalysis, and they have been applied to various field (Figure 1-7). In homogeneous photocatalysis, the reactants and the photocatalysts exist in the same phase. The most commonly used homogeneous photocatalysts include ozone and photo-

Fenton systems (Fe^{+} and Fe^{+}/H_2O_2). The reactive species is the •OH which is used for different purposes. Heterogeneous catalysis has the catalyst in a different phase from the reactants. Heterogeneous photocatalysis is a discipline which includes a large variety of reactions: mild or total oxidations, dehydrogenation, hydrogen transfer, and deuterium-alkane isotopic exchange, metal deposition, water detoxification, gaseous pollutant removal, etc.

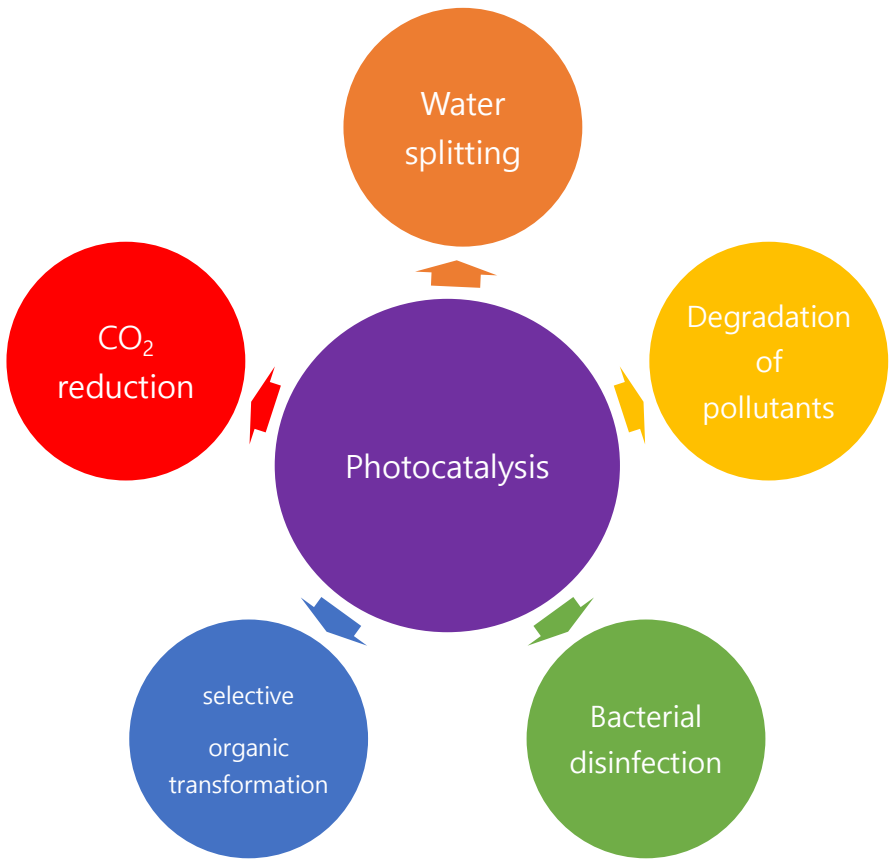

Figure1-7 Schematic of applications in photocatalysis research field.

Photodeposition

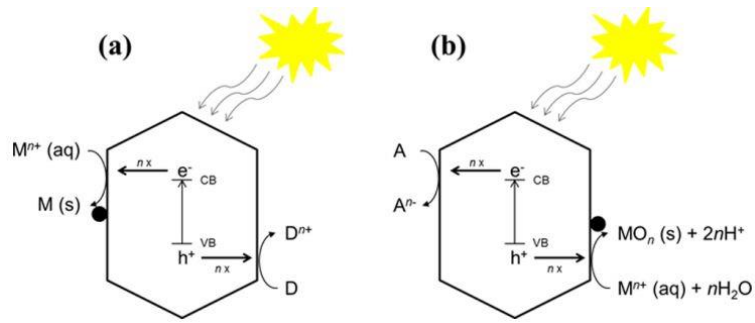

Figure 1-8 Schematics of (a) reductive photodeposition and (b) oxidative photodeposition. VB, valence band; CB, conduction band; M, metal; D, electron donor, A, electron acceptor; n, number of electrons or holes involved. Reproduced from ref. 30.

Illumination of a slurry of semiconductor particles in an aqueous phase solution of a metal salt often results in deposition of well-defined metal (oxide) nanoparticles on the surface of the semiconductor: this phenomenon is generally known as photodeposition. Thus, photodeposition is based on light-induced electrochemistry. A generalized equation for reductive photodeposition of a metal M is

$$M^{n+}(aq) + ne^- \rightarrow M(s) \quad (1)$$

Its counterpart, oxidative photodeposition, is the formation of metal oxide nanoparticle deposits, for example, through eq 2:

$$M^{n+}(aq) + nh^{+} + nH_2O \rightarrow MO_n(s) + 2nH^{+} \quad (2)$$

A schematic overview of both reductive and oxidative photodeposition is provided in Figure 1-8. To allow photodeposition, the reduction/oxidation potential of the metal (oxides) to be deposited must be at favorable positions with regard to the energy-band positions of the semiconductor; that is, the conduction band (E vs NHE scale) must be more negative than the reduction potential of metals, and the valence band must be more positive (E vs NHE scale) than the oxidation potential of the species to be oxidized, being a metal (ion), water, or sacrificial agent.[30]

1.4. References

[1] A.M. lonescu, *Connections QJ*, **2016**, 15, 31.

[2] T. Laaksonen, V. Ruiz, P. Lilijeroth and B. M. Quinn, *Chem, Soc, Rev*., **2008**, 37, 1836.

[3] Demchenko AP, Dekaliuk MO. *J. Mater. Chem. C*, 2013, ***1***, 042001.

[4] B. Zhu, S. Sun, Y. Wang, S. Deng, G. Qian, M. Wang and A. Hu, *J. Mater. Chem. C*, **2013**, 1, 580.

[5] J. Zhou, C. Booker, R. Li, X. Zhou, T.-K. Sham, X. Sun and Z. Ding, *J. Am. Chem. Soc.*, **2007**, 129, 744.

[6] D. B. Shinde and V. K. Pillai, *Chem.–Eur. J.*, **2012**, 18, 12522.

[7] Y.-P. Sun, B. Zhou, Y. Lin, W. Wang, K. S. Fernando, P. Pathak, M. J. Meziani, B. A. Harruff, X. Wang and H. Wang, *J. Am. Chem. Soc.*, **2006**, 128, 7756.

[8] X. Li, H. Wang, Y. Shimizu, A. Pyatenko, K. Kawaguchi and N. Koshizaki, *Chem. Commun.*, **2011**, 47, 932.

[9] Y. Liu, N. Xiao, N. Gong, H. Wang, X. Shi, W. Gu and L. Ye, *Carbon*, **2014**, 68, 258.

[10] B. Hu, K. Wang, L. Wu, S. H. Yu, M. Antonietti and M. M. Titirici, *Adv. Mater.*, **2010**, 22, 813.

[11] M.-M. Titirici and M. Antonietti, *Chem. Soc. Rev.*, **2010**, 39, 103.

[12] Z.-C. Yang, M. Wang, A. M. Yong, S. Y. Wong, X.-H. Zhang, H. Tan, A. Y. Chang, X. Li and J. Wang, *Chem. Commun.*, **2011**, 47, 11615.

[13] Yue X, Chun-Jing T, Hong H, Chao-Qun S, Ya-Kun Z, Qun-Feng Y, Ai-Jun W. *Chinese Journal of Analytical Chemistry*. **2014**, 42,1252.

[14] D. Choi, S. Ham, D.-J. Jang, *J. Environ. Chem. Eng.*, **2018**, 6, 1.

[15] Q.-L. Zhao, Z.-L. Zhang, B.-H. Huang, J. Peng, M. Zhang and D.-W. Pang, *Chem. Commun.*, **2008**, 5116.

[16] B. Chen, F. Li, S. Li, W. Weng, H. Guo, T. Guo, X. Zhang, Y. Chen, T. Huang and X. Hong, *Nanoscale*, **2013**, 5, 1967.

[17] A. B. Bourlinos, A. Bakandritsos, A. Kouloumpis, D. Gournis, M. Krysmann, E. P.

Giannelis, K. Polakova, K. Safarova, K. Hola and R. Zboril, *J. Mater. Chem.*, **2012**, 22, 23327.

[18] W. Shi, Q. Wang, Y. Long, Z. Cheng, S. Chen, H. Zheng and Y. Huang, *Chem. Commun.*, **2011**, 47, 6695.

[19] A. Zhu, Q. Qu, X. Shao, B. Kong and Y. Tian, *Angew. Chem., Int. Ed.*, **2012**, 124, 7297.

[20] H. X. Zhao, L. Q. Liu, Z. De Liu, Y. Wang, X. J. Zhao and C. Z. Huang, *Chem. Commun.*, **2011**, 47, 2604.

[21] F. Y. Yan, Y. Zou, M. Wang, X. L. Mu, N. Yang and L. Chen, *Sens. Actuators, B*, **2014**, 192, 488–495.

[22] H. M. Goncalves, A. J. Duarte and J. C. E. da Silva, *Biosens. Bioelectron.*, **2010**, 26, 1302.

[23] S. Barman and M. Sadhukhan, *J. Mater. Chem.*, **2012**, 22, 21832.

[24] J. M. Liu, L. P. Lin, X. X. Wang, S. Q. Lin, W. L. Cai, L. H. Zhang and Z. Y. Zheng, *Analyst*, **2012**, 137, 2637.

[25] Y.-L. Zhang, L. Wang, H.-C. Zhang, Y. Liu, H.-Y. Wang, Z.-H. Kang and S.-T. Lee, *RSC Adv.*, **2013**, 3, 3733.

[26] S. S. Wee, Y. H. Ng and S. M. Ng, *Talanta*, **2013**, 116, 71.

[27] M. Zheng, Z. G. Xie, D. Qu, D. Li, P. Du, X. B. Jing and Z. C. Sun, *ACS Appl. Mater. Interfaces*, **2013**, 5, 13242.

[28] S. Kumar, T. Ye, T. Takami, B. C. Yu, A. K. Flatt, J. M. Tour and P. S. Weiss, *Nano Lett.*, **2008**, 8, 1644.

[29] Y. Yao, G. H. Li, S. Ciston, R. M. Lueptow and K. A. Gray, *Environ. Sci. Technol.*, **2008**, 42, 4952.

[30] K. Wenderich, G.o Mul *Chem. Rev.* **2016**, 11623, 14587.

Chapter 2. Visible-light Photocatalytic Reduction of Cr(VI) via Carbon Quantum Dots-decorated TiO_2 Nanocomposites†

† This is reproduced from Dayeon Choi, Sooho Ham, and Du-Jeon Jang, *J. Environ. Chem. Eng.*, **2018,** *6*, 1-8. ⓒ 2018 Elsevier Inc.

2.1. Abstract

Carbon quantum dots (CQDs) having sizes of 5-10 nm have been prepared facilely by a hydrothermal method and incorporated with TiO_2 nanoparticles to produce CQDs-decorated TiO_2 (C/TiO_2) nanocomposites with various dosages of CQDs. Under visible-light irradiation, the photocatalytic activities of Cr(VI) reduction via C/TiO_2 nanocomposites have been monitored and found to depend highly on the dosage of CQDs. In particular, the photocatalytic rate constant (0.0449 min^{-1}) of C/TiO_2 nanocomposites with 3 wt% CQDs is 8.6 times higher than that of pure TiO_2 nanoparticles. When CQDs are excited by visible light, photo-generated electrons transfer from CQDs into the conduction band of TiO_2 on the time scale of 1500 ps. Transferred electrons are subsequently captured by Cr(VI) ions, reducing Cr(VI) into Cr(III). Thus, π-conjugated CQDs act as sensitizers to provide visible-light response to the TiO_2 nanoparticles of C/TiO_2 dyade structures, leading to the highly efficient photocatalytic reduction of Cr(VI). Our as-prepared C/TiO_2 nanocomposites are applicable in an inexpensive way to treat wastewater by utilizing solar energy without employing electron donors.

2.2. Introduction

Water pollution is known as one of the top ten problems that humanity is facing in this century. The effective removal of hazardous contaminants is the key issue for recycling of wastewater.[1] Industrial and other anthropogenic processes have been constantly releasing heavy metal ions into the environment, among which hexavalent chromium Cr(VI) is hazardous to public health due to its greater mobility and carcinogenic properties.[2,3] Cr(VI) has been recognized as one of the world's most hazardous pollutants arising from various industrial processes such as electroplating, mining, leather tanning, and dye manufacturing; the maximum permissible concentration of Cr(VI) in drinking water is 0.05 ppm.[4-6] In aqueous solutions, Cr(VI) does not form insoluble compounds in aqueous solutions. Thus, it tends to be accumulated in living organisms through food chains.[3] Thus, it is necessary to remove Cr(VI) facilely from wastewater. A general way to reduce the toxicity of Cr(VI) is to convert Cr(VI) into less toxic trivalent chromium Cr(III), which can be easily precipitated out of solutions in the form of $Cr(OH)_3$.[7] Numerous researchers have strived to reduce Cr(VI) contaminants into Cr(III) species at low cost with minimal use of chemicals and additional environmental impacts. Cr(VI) can be reduced to Cr(III) by using diverse methods such as direct electric current, iron-salt reduction, sulfur-compound reduction, and

photocatalysis.[3] Except photocatalysis, the methods usually suffer from high cost, large chemical dosage, and secondary pollution; the technology of photocatalysis is a highly attractive environment-friendly approach for practical applications since it achieves the one-step reduction of Cr(VI) by utilizing sunlight as the energy source. In the photocatalytic process, electrons and holes are generated by absorption of photons having equal or higher energy than the semiconductor bandgap. The photocatalytic activity depends on the ability of the catalyst to create electron-hole pairs, which subsequently generate reactive species such as hydroxyl radicals to undergo secondary reactions.[4]

Recently, considerable efforts have been devoted to exploring efficient photocatalysts for Cr(VI) reduction;[1-9] for example, titanium dioxide could effectively reduce Cr(VI) to Cr(III).[1,4,7,9] Due to good photodurability, nontoxicity, chemical inertness, and low cost, TiO_2 has been one of the most important semiconductors being commonly used in heterogeneous photocatalysis.[10-12] Despite good performances and stabilities, TiO_2-based photocatalysts have limited applications because they lack visible-light responsivity due to their large band-gap energy (3.2 eV) and the fast recombination of photoexcited electrons and holes restricts the solar-energy conversion efficiency.[10-12] To solve these problems, many strategies have been developed, such as loading of noble metals, doping with metallic and nonmetallic elements, sensitization with organics, and coupling with

narrow band-gap semiconductors.[13-17]

Carbon quantum dots (CQDs), whose spherical nanocarbons have small sizes below 10 nm, are an attractive kind of recently discovered carton materials.[18] These CQDs were discovered accidentally during the purification of single-walled carbon nanotubes prepared by arc-charged methods.[19] CQDs can be prepared with various methods, which are normally classified into two main groups: top-down and bottom-up methods.[18,19] Top-down methods, where CQDs are broken off from large carbon materials, consist of arc discharge, electrochemical oxidation, and laser ablation. Bottom-up methods, where CQDs are formed from simple molecular carbon precursors, consist of combustion- or heat-supported synthetic routes and microwave-assisted methods. Most CQDs contain carboxylic acid moieties at their surfaces, resulting in excellent aqueous solubility and suitability for subsequent functionalization with various organic, polymeric, inorganic, or biological species.[20-22] CQDs also have other unique properties such as outstanding electronic properties (electron donors and acceptors), up-converting and size-dependent photoluminescence, chemical inertness, photostability, and low cytotoxicity.[23,24] Thus, they have been employed in bio-imaging, sensing, and electronics.[20-23] With concerns of health, environment, and biological hazards, CQDs are fascinative alternatives for metal-based quantum dots (QDs). CQDs can be facilely synthesized and functionalized. Moreover, the absorption of CQDs covers a broad

UV-IR spectral range due to their conjugated π-domains. Thus, CQDs-TiO_2 dyade structures can be ideal systems to extend the visible-light photocatalytic activity of TiO_2.[13,17,24]

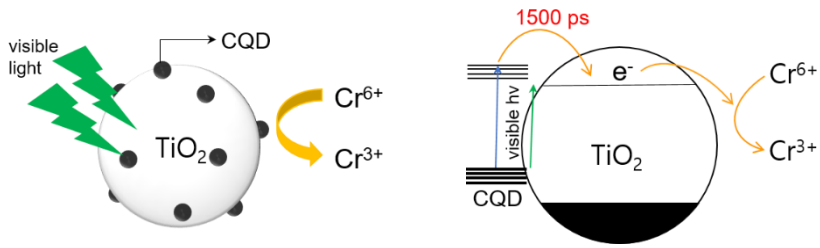

Figure 2-1 Schematic (left) and proposed mechanism (right) for the photocatalytic reduction of Cr(VI) over a C/TiO_2 nanocomposite under visible-light irradiation.

In this work, we have synthesized dyade structures of CQDs-decorated TiO_2 (C/TiO_2) nanocomposites with various dosages of CQDs via a simple hydrothermal method. There are a number of ways by which two components of a hybrid structure can be synthesized separately and then linked together with a suitable ligand. However, the methods usually lead to an insulating organic layers that hinder charge transfer at the interfaces of the two components. In comparison, the hydrothermal reaction is an eco-friendly method to attach two materials without using any other chemical linker materials. Direct contact at interfaces without insulating layers is beneficial to charge transfer in dyade structures.[25] The photocatalytic activity of C/TiO_2 nanocomposites under visible light has been

found to be much higher than that of TiO_2 nanoparticles. When C/TiO_2 nanocomposites are exposed to visible light ($\lambda \geq 420$ nm), photo-generated electrons transfer from the excited states of CQDs to the conduction band of TiO_2 nanoparticles, and then they are captured by Cr(VI) ions on the time scale of 1500 ps, reducing Cr(VI) into Cr(III) (Figure 2-1). Owing to the heterojunction of TiO_2 and CQDs, the absorption of visible light and the separation of consequently photo-generated charges are promoted, resulting in the improved photocatalytic reduction of Cr(VI). Our prepared C/TiO_2 nanocomposites are suggested to be applicable as photocatalysts in the field of Cr(VI) elimination.

2.3. Experimental

2.3.1. Materials

Chemicals were used without further purificatoin: citric acid (s, 99.5%), sodium dichromate dihydrate (s, 99.5%), and sodium dichromate dihydrate (s, 99.5%) from Sigma-Aldrich; ethylenediamine (l, 99%) and sodium sulfite (s, 98%) from Alfa-Aesar. Ultrapure deionized water (>15 MΩ cm) from an Elga PURELAB Option-

S system was used throughout the experiments. Commercially available P25 TiO_2 nanoparticles were obtained from Degussa.

2.3.2. Preparation

CQDs. Following to Zhu et al.,[23] CQDs were synthesized by a hydrothermal method. 1.05 g of citric acid was added into 10 mL of water and stirred for 10 min. Then, 335 µL of ethylenediamine was added slowly and stirred for 1 h, and the mixed transparent solution was maintained at 200 °C for 5 h. After the reaction, the autoclave was naturally cooled down to room temperature. The transparent solution turned into a dark blown solution, which was then centrifuged at 10,000 rpm for 10 min. The supernatant was filtered using a filter with 200 nm pores and the subsequent filtrate containing CQDs was dialyzed in a dialysis bag (cutoff M_n: 1.0 kDa) against water for a day to remove small-size side products. The dialyzed aqueous colloidal solution of CQDs was freeze-dried at -63 °C for 3 days to obtain solid CQDs.

C/TiO_2 nanocomposites. 10 mL of ethanol was mixed with 20 mL of an aqueous solution containing 30 mg of P25 TiO_2 nanoparticles and a specifically varied volume of an aqueous 1.0 mg mL^{-1} CQD solution. The mixture was stirred at room temperature for 2 h, transferred into a Teflon-lined stainless-steel autoclave, and

maintained at 140 °C for 4 h. The autoclave was cooled down to room temperature naturally and centrifuged at 8,000 rpm for 10 min. Collected products were washed with water and ethanol several times and dried at 60 °C for 5 h. Hereafter, the products decorated with indicated *x* weight percentages of CQDs will be designated as *x*% C/TiO_2 nanocomposites, where 100% C/TiO_2 and 0% C/TiO_2 nanocomposites represent pure CQDs and pure TiO_2 nanoparticles, respectively.

2.3.3. Characterization

Transmission electron microscopy (TEM) images were measured using a Hitachi H-7600 microscope operating at 100 kV, and high-resolution TEM (HRTEM) images and energy-dispersive X-ray (EDX) elemental mappings were measured utilizing a JEOL JEM-2100F microscope. While UV-vis absorption spectra were measured using a Scinco S-3000 spectrophotometer, UV-vis diffuse reflectance spectra were collected using a StellaNet US/EPP 2000C spectrometer. Detailed procedures for the measurement of photoluminescence (PL) spectra, PL decay kinetics profiles, X-ray diffraction (XRD) patterns, and X-ray photoelectron spectroscopy (XPS) data have already been reported [25]. Fourier transform infrared (FTIR) spectra were conducted using a Thermo Scientific Nicolet 6700 spectrometer. Thermogravimetric analysis (TGA) curves were collected with a TA

Instruments DCT Q600 analyzer. Inductively coupled plasma mass spectroscopy (ICP-MS) data were measured using a Varian 820-MS spectrometer.

2.3.4. Photocatalytic reduction experiments

The photocatalytic reduction activity of C/TiO_2 nanocomposites were evaluated by measuring the photoreduction of Cr(VI) under ambient conditions. Sodium dichromate dihydrate was used as the source of Cr(VI). In a typical procedure, 50 mg of a catalyst and 2.52 g of sodium sulfite were added to 39.75 mL of water, which was sonicated for 5 min and then stirred for 30 min. Then, the above solution was mixed with 0.25 mL of a 20 mM Cr(VI) aqueous solution and stirred for 1 h in the dark to establish an adsorption-desorption equilibrium of Cr(VI) on the surface of the catalyst. The suspension in a glass reactor was then irradiated under visible light using a 420+ nm cutoff filter, and an aliquot of 3.0 mL was taken at every 10 min and centrifuged to separate the supernatant. The absorption spectrum was measured to probe the decay of the absorbance at 372 nm to quantify the concentration of remnant Cr(VI). Control photocatalytic experiments in the absence of any catalysts as well as in the dark with 3% C/TiO_2 nanocomposites have also been conducted.

2.4. Results and discussion

2.4.1. HRTEM image and EDX elemental maps

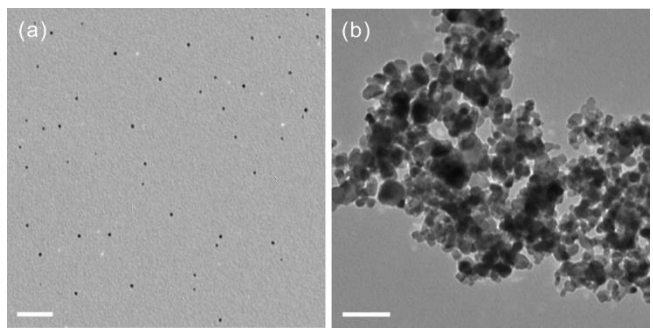

Figure 2-2 TEM images of CQDs (a) and 3% C/TiO_2 nanocomposites (b). Each scale bar indicates 100 nm.

Figure 2-2a shows that as-prepared CQDs have spherical shapes with diameters of 5-10 nm and that they are uniformly dispersive without forming apparent aggregates in water. With various dosages of CQDs, C/TiO_2 nanocomposites have been synthesized by a hydrothermal method. However, it is hard to discriminate CQDs from supporting TiO_2 nanoparticles using normal TEM images due to the small sizes and amount of CQDs (Figure 2-2b). Therefore, EDX elemental maps have been explored to confirm the respective distributions of the compositional elements. Figure 2-3 clearly shows that CQDs have been loaded successfully into

TiO_2 nanoparticles with good dispersion. Due to the low crystallinity of CQDs, it was not possible for us to confirm their intrinsic lattice with HRTEM images even at high magnification.

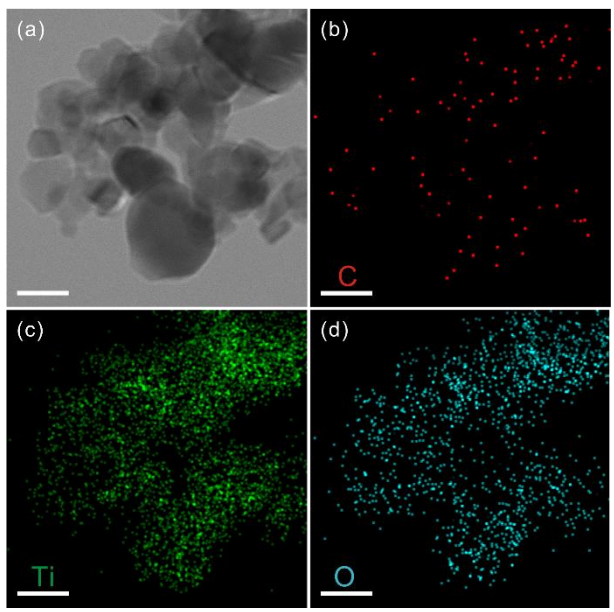

Figure 2-3 HRTEM image (a) and EDX elemental maps (b-d) of 3% C/TiO_2 nanocomposites. Each scale bar indicates 50 nm.

2.4.2. Structural characteristics

As shown in Figure 2-4, the XRD pattern of as-prepared CQDs with sizes of 5-10 nm has two superimposed broad reflections: these two broad peaks can be

attributed to amorphous carbon composed of aromatic carbon sheets oriented in a random way. This suggests that CQDs are composed of disordered and amorphous carbon.[23] While a relatively sharp peak at 2θ of 21.2° indicates the (002) planes of graphite, a broad one centered at 38.9° arises from the (004) planes of graphite.[16,20] Assuming that the peak broadening of an XRD pattern is induced by the size effect of crystals, we have estimated the mean crystal diameter of CQDs as ~0.5 nm using the Scherrer's formula.[26] This indicates that the average crystal size of CQDs is much smaller than the average crystal size of supporting P25 TiO_2 nanoparticles in 3% C/TiO_2 nanocomposites.

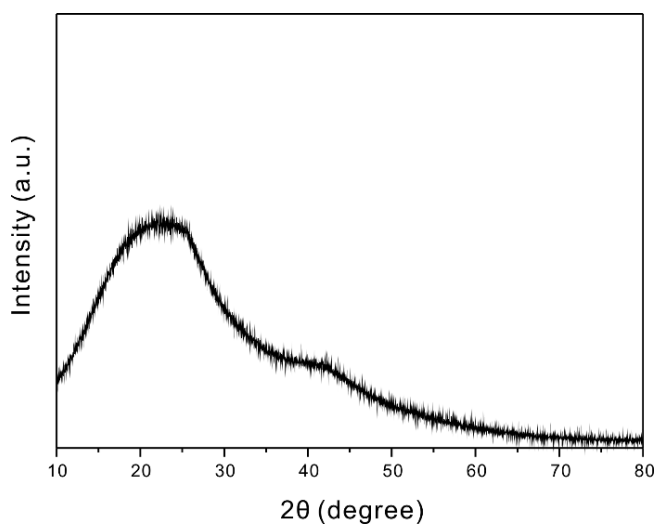

Figure 2-4 XRD pattern of as-prepared CQDs.

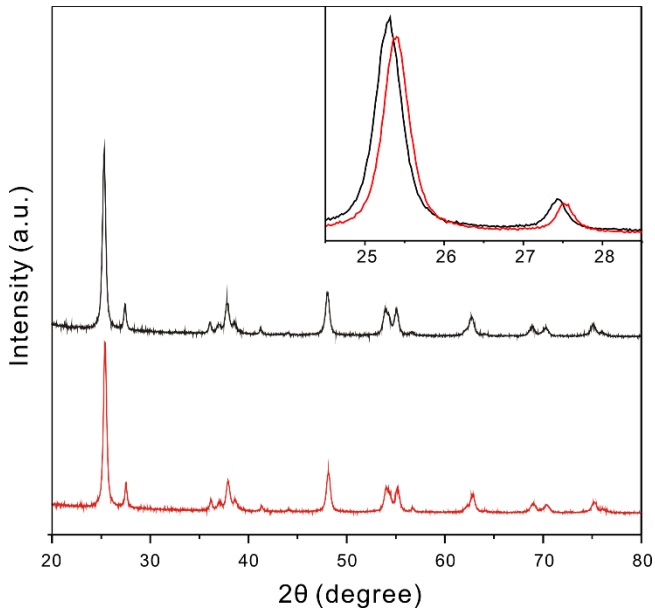

Figure 2-5 XRD patterns of pure TiO_2 nanoparticles (black) and 3% C/TiO_2 nanocomposites (red).

Figure 2-5 shows that pure TiO_2 nanoparticles have an XRD pattern arising from mixed phases of anatase and rutile.[10] For 3% C/TiO_2 nanocomposites, the characteristic peaks of carbon are too weak to be observed, because the dosage and crystallinity of CQDs are low and the diffraction intensity of carbon is weak in a heterostructure.[10,13,16,27] The inset of Figure 2-5 shows that the XRD peaks of 3% C/TiO_2 nanocomposites slightly shift to higher angles compared with the respective ones of pure TiO_2 nanoparticles. This suggests that during the hydrothermal reaction, relatively small carbon atoms incorporate into the pure TiO_2 lattice, resulting in contraction of adjacent atom distances. In addition, these carbon atoms

hinder X-ray diffraction via lowering the crystallinity of TiO_2 nanoparticles. Thus, the XRD peak intensity of 3% C/TiO_2 nanocomposites is slightly reduced compared with that of pure TiO_2 nanoparticles.[27] From these XRD patterns, we can conclude that carbon atoms having a relatively small atomic size have been successfully incorporated into TiO_2 nanoparticles via forming Ti-O-C bonds.

2.4.3. Surface properties

To understand the specific bonding states of the compositional elements of 3% C/TiO_2 nanocomposites, we have measured the XPS spectra of CQDs, pure TiO_2 nanoparticles, and 3% C/TiO_2 nanocomposites. Figure 2-6a displays that the XPS spectrum of C 1s of CQDs has been fitted into three Gaussian curves located at 284.5, 286.4, and 288.6 eV, which can be ascribed to C–C/C=C, C–O, and C=O, respectively.[10,17] Meanwhile, the C 1s XPS spectrum of 3% C/TiO_2 nanocomposites (Figure 2-6b) has been fitted into four Gaussian bands centered at 284.5, 286.7, 288.9, and 290.9 eV, which can be attributed to C–C/C=C, C–O, C=O, and O–C=O, respectively.[13,15] Compared with the C 1s XPS spectrum of CQDs, that of 3% C/TiO_2 nanocomposites shows more peaks of carbon bound to oxygen, indicating that Ti-O-C bonds have been formed in the nanocomposites. The Ti 2p XPS spectrum of Figure 4c has been fitted into two Gaussian bands located at 466.68

and 460.88 eV, which can be ascribed to the binding energies of $2p_{2/1}$ and $2p_{3/2}$, respectively. Compared with the binding energies of pure TiO_2 nanoparticles, 465.84 eV and 460.24 eV, the respective ones of the nanocomposites are slightly shifted to higher binding energies due to changes in the chemical environment of Ti in the 3% C/TiO_2 nanocomposites; when carbon couples with TiO_2 nanoparticles, Ti-O-C bonds are formed, indicating that CQDs are chemically bound to TiO_2 nanoparticles.[13] Figure 4d shows that three O 1s XPS peaks at 531.5, 532.1, and 533.8 eV can be attributed Ti–O–C, C–OH, and C–O–C, respectively, further revealing the chemical bonding of CQDs on TiO_2.[12] In summary, our XPS data support that CQDs have been incorporated successfully with TiO_2 nanoparticle to form C/TiO_2 nanocomposites via forming Ti-O-C bonds.

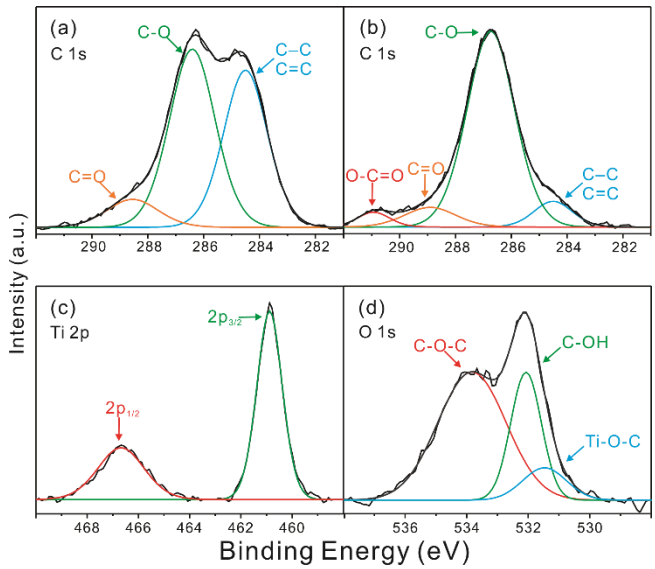

Figure 2-6 C 1s XPS spectrum of as-prepared CQDs (a), and C 1s (b), Ti 2p (c), and O 1s (d) XPS spectra of 3% C/TiO_2 nanocomposites. Each spectrum has been deconvoluted from Gaussian fitting.

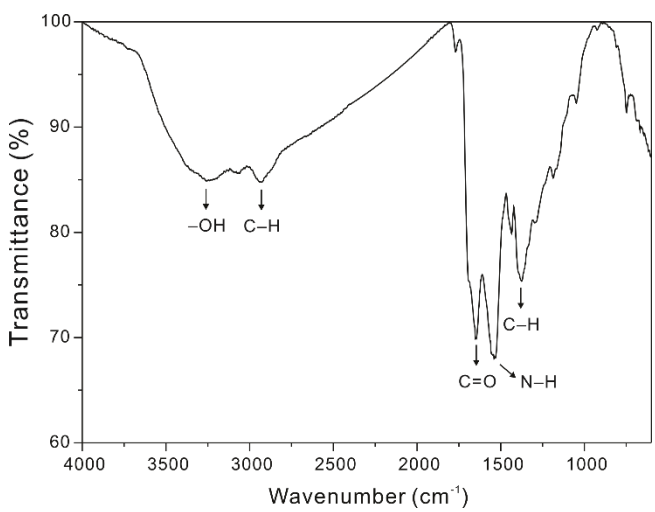

Figure 2-7 FTIR spectrum of as-prepared CQDs.

The FTIR spectrum of Figure 2-7 shows that various carbon functional groups exist on the surfaces of CQDs. The broad absorption band around 3250 cm^{-1} can be attributed to the stretching vibrational mode of O–H, while the characteristic shoulder at 2900 cm^{-1} can be assigned to the C–H stretching mode.[12] The characteristic absorption peaks of CQDs at 1650, 1530, and 1370 cm^{-1} correspond to the stretching vibration of C=O, the bending vibration of N–H, and the bending vibration of C–H, respectively.[13] Thus, Figure 2-7 suggests that our as-prepared CQDs contain diverse functional groups such as –OH, C–H, C=O, and N–H.

Figure 2-8 shows that pure TiO_2 nanoparticles have characteristic IR peaks at 3370 and 1630 cm^{-1} corresponding to the stretching and the bending vibrations of O–H groups, respectively. The intense and broad band below 1000 cm^{-1} is associated with the stretching mode of Ti–O–Ti.[13,16] With increase of the CQD dosage, the absorption peaks attributable to the CQDs of C/TiO_2 nanocomposites become gradually intensive; 2900, 1650, 1530, and 1370 cm^{-1} have been assigned to the stretching mode of C–H, the stretching vibration of C=O, the bending mode of N–H, and the bending vibration of C-H, respectively, as mentioned above with Figure 2-7.[12,13] A close examination of the FTIR spectra of C/TiO_2 nanocomposites in Figure 2-8 reveals that the broad and intense absorption band below 1000 cm^{-1} becomes even broader and more intense with the dosage increase of CQDs due to the increased effect of the Ti–O–C vibration. [10,12,15] Thus, together with XRD and

XPS results, FTIR data also suggest that C/TiO_2 nanocomposites with Ti–O–C bonds have been facilely synthesized by a simple hydrothermal process.

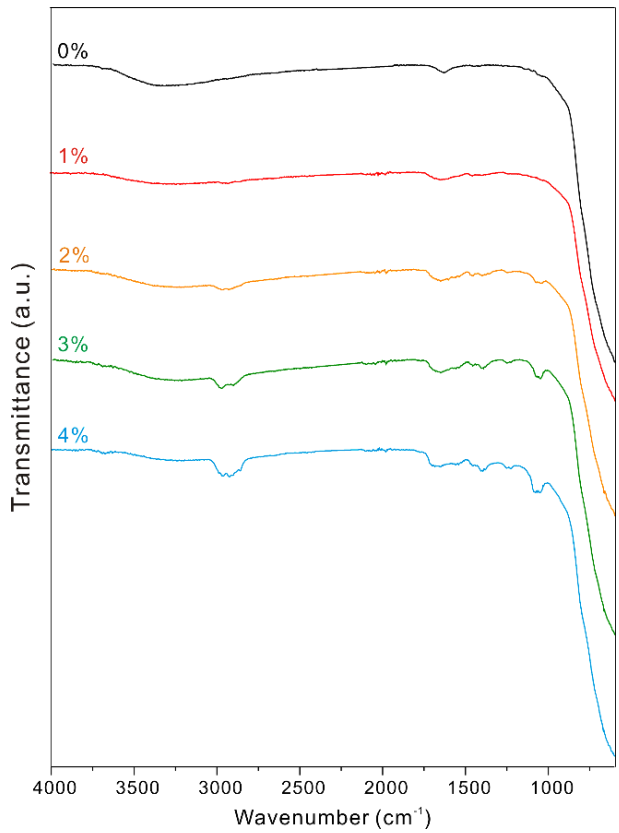

Figure 2-8 FTIR spectra of C/TiO_2 nanocomposites decorated with respectively indicated weight percentages of CQDs.

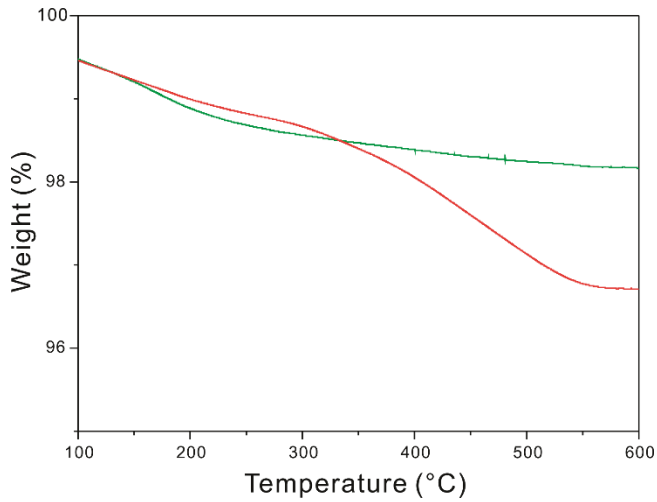

Figure 2-9 TGA curves of pure TiO_2 nanoparticles (green) and 3% C/TiO_2 nanocomposites (red).

TGA curves of pure TiO_2 nanoparticles and 3% C/TiO_2 nanocomposites have also been recorded in a nitrogen atmosphere at a heating rate of 10 °C min^{-1} (Figure 2-9). Both pure TiO_2 nanoparticles and 3% C/TiO_2 nanocomposites have shown mass losses at ~150 °C due to the elimination of adsorbed water and at ~200 °C due to the desorption of hydroxyl groups attached to the surfaces.[12,15] Meanwhile, 3% C/TiO_2 nanocomposites have large weight degradation between 350-500 °C corresponding to the slow combustion of CQDs.[15] From the difference of weight losses between pure TiO_2 nanoparticles and 3% C/TiO_2 nanocomposites, we have estimated that the actual content of the CQDs on 3% C/TiO_2 nanocomposites is about 1.5 wt%.

2.4.4. Optical properties

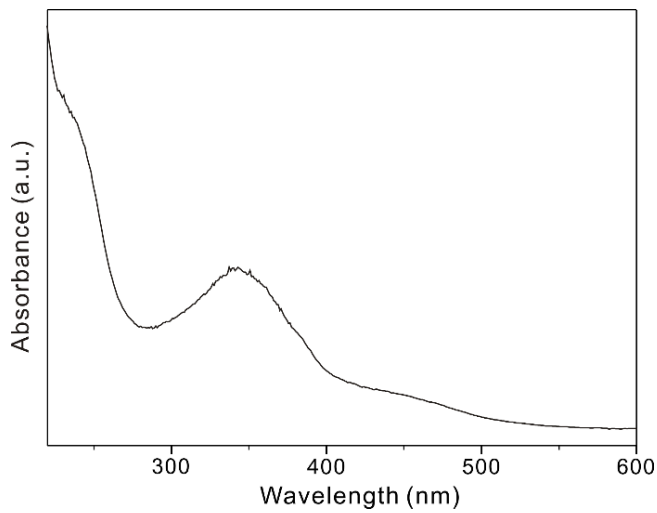

Figure 2-10 Absorption spectrum of as prepared CQDs dispersed in water.

The absorption spectrum of CQDs shows two peaks around 240 and 350 nm and a broad band ranging from 400 to 600 nm (Figure 2-10). Unlike conventional metal-based QDs having band-gap absorptions that are caused by the quantum confinement effect, CQDs have absorptions due to the conjugated π-domains of core carbon atoms.[19] Thus, the photoexcitation of CQDs covers a broad UV-IR spectral range. In the meantime, the peak at 240 nm is attributable to the π-π* transition of sp^2 carbon, while the peak at 350 nm arises from the n-π* transition of C=O bonds from the surfaces of CQDs.[19,20]

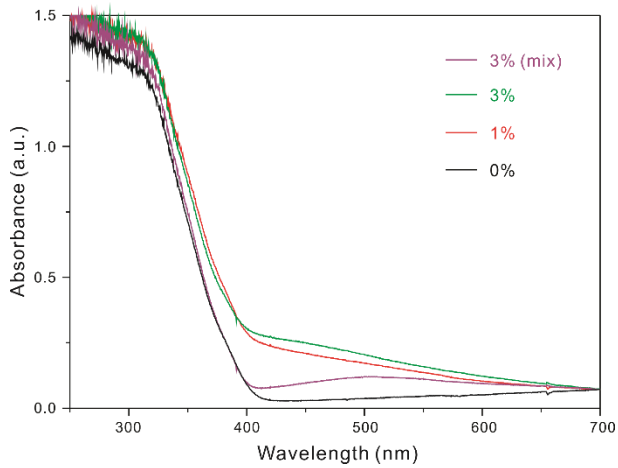

Figure 2-11 Diffuse-reflectance spectra of C/TiO_2 nanocomposites decorated with respectively indicated weight percentages of CQDs. The 3% (mix) and 3% indicate physically mixed and hydrothermally treated 3% C/TiO_2 nanocomposites, respectively.

In case of 0% C/TiO_2 nanocomposites (pure TiO_2 nanoparticles), there is almost no visible response. However, the absorption of C/TiO_2 nanocomposites with a small amount of CQDs extends to the entire visible region obviously, and the visible absorption of the nanocomposites increases with the dosage of CQDs (Figure 2-11). In order to understand the origin of the visible absorption of C/TiO_2 nanocomposites, we have also compared the absorption spectrum of 3% (mix) C/TiO_2 nanocomposites, where CQDs were physically mixed with pure TiO_2 nanoparticles, with the absorption spectrum of 3% C/TiO_2 nanocomposites, where CQDs were hydrothermally treated with pure TiO_2 nanoparticles. The absorption of 3% (mix) nanocomposites is merely the spectral summation of pure TiO_2

nanoparticles and CQDs, thus exhibiting the original absorption peaks of the individual components. Meanwhile, the enhanced spectra of hydrothermally treated C/TiO_2 nanocomposites show an enhanced additional absorption band ranging from 400 to 600 nm, due to the interband transition from the HOMO level of CQDs into the conduction band of TiO_2 nanoparticles.[17,23] This also suggests that our as-prepared nanocomposites have dyade structures with the formation of Ti–O–C bonds between TiO_2 nanoparticles and CQDs. Overall, CQDs in the dyade structures of C/TiO_2 nanocomposites have enhanced visible-light response extensively, being expected to improve the photocatalytic activity of the nanocomposites under visible-light irradiation (see below).[13,27]

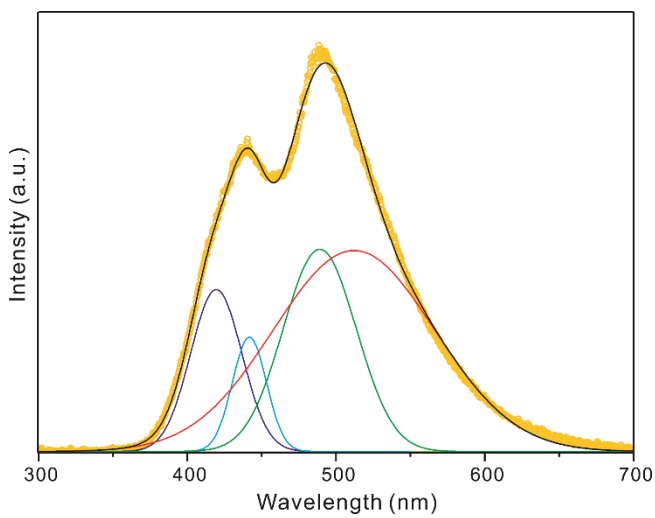

Figure 2-12 Emission spectrum of as-prepared CQDs (yellow circles) dispersed in ethanol with excitation at 266 nm. The solid lines correspond to the deconvoluted Gaussian curves (violet, blue, green, and red) and the integral of the fitted curves (black).

As shown in Figure 2-12, the PL spectrum of CQDs exhibits asymmetric peaks, suggesting multi-fluorophores or luminescent centers.[28] Thus, we have tried to fit the spectrum using four Gaussian functions, which are respectively centered at 420 ± 23 (14.0%), 440 ± 11 (6.5%), 490 ± 25 (25.0%), and 510 ± 54 (54.5%) nm. Even though the exact origins of the fluorescence emission of CQDs have not been entirely understood yet, two emission mechanisms have been proposed; the first one is attributed to band-gap transitions caused by conjugated π-domains, while the second one involves with the radiative recombination of excitons located at the surface defects of CQDs.[18,19,21,28] Therefore, together with HRTEM and XRD data, we can conclude that our as-prepared CQDs have low crystallinity due to many surface defects. Moreover, the PL centers of CQDs can be controlled simultaneously by chemical groups, surface passivation, and sizes. In our case, we suggest that the PL centers have been affected substantially by surface functional groups such as amine, although we still suffer from a dearth of reliable evidences.[22]

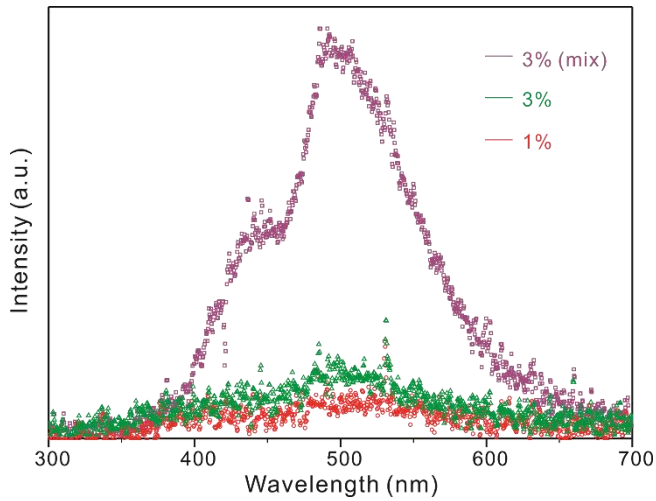

Figure 2-13 Emission spectra of C/TiO_2 nanocomposites decorated with respectively indicated weight percentages of CQDs. 0.50 mg of each sample was dispersed in 1.0 mL of ethanol and excited at 266.

The transfer properties of photo-generated electrons from CQDs to TiO_2 nanoparticles are very important for the overall photocatalytic reduction efficiency of C/TiO_2 nanocomposites. Thus, it is important to examine the PL intensities and spectra of C/TiO_2 nanocomposites closely. Figure 2-13 displays that compared with the PL spectrum of physically mixed 3% C/TiO_2 nanocomposites, the PL spectrum of hydrothermally treated 3% C/TiO_2 nanocomposites is drastically quenched, suggesting that the photo-generated electrons of CQDs can be transferred easily to the conduction band of TiO_2 nanoparticles in C/TiO_2 nanocomposites.[16] Moreover, the PL intensity of 1% C/TiO_2 nanocomposites is even lower than that of 3% C/TiO_2 nanocomposites because of the relatively smaller dosage of CQDs.

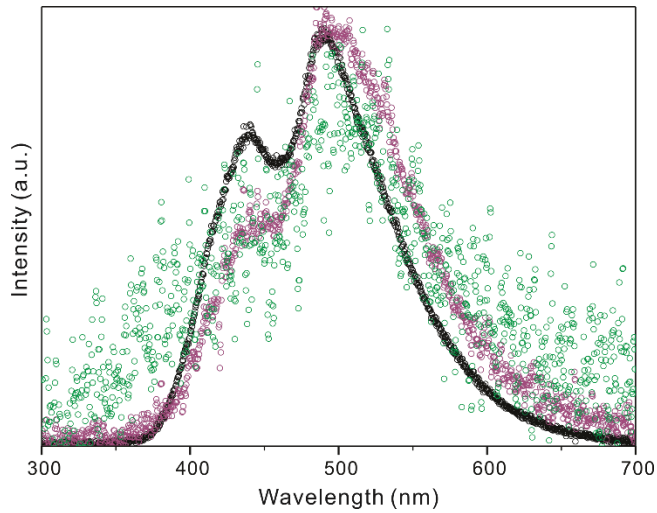

Figure 2-14 Maximum-normalized emission spectra of as-prepared CQDs (black), 3% (mix) C/TiO_2 nanocomposites (purple), and 3% C/TiO_2 nanocomposites (green) dispersed in ethanol with excitation at 266 nm.

Figure 2-14 displays that although the PL spectrum of 3% C/TiO_2 nanocomposites has low signal-to-noise ratios, it is spectrally similar to the PL spectrum of 3% (mix) C/TiO_2 nanocomposites. This suggests that the PL spectral nature of CQDs in C/TiO_2 nanocomposites has hardly been affected by hydrothermal treatment. However, compared to the PL spectrum of as-prepared CQDs, the spectrum of 3% (mix) C/TiO_2 nanocomposites is shifted to the red by 18 nm and its left shoulder peak is reduced by 30%. This designates that the high-energy PL part of CQDs is quenched preferentially in C/TiO_2 nanocomposites. In addition, the PL spectrum of 3% (mix) C/TiO_2 nanocomposites has been fitted four

Gaussian functions centered at 410 ± 9 (3.0%), 440 ± 13 (10.6%), 490 ± 24 (26.7%), and 525 ± 45 (59.7%) nm. This also supports that the blue PL region of multi-fluorophores in CQDs is more selectively quenched by TiO_2 in C/TiO_2 nanocomposites. Although the exact origins of the fluorescence emission of CQDs have not been entirely understood yet, Figure 2-12, as well as Figure 2-13 and Figure 2-14, has suggested that CQDs in C/TiO_2 nanocomposites have been chemically incorporated with TiO_2 nanoparticles via forming Ti–O–C bonds.

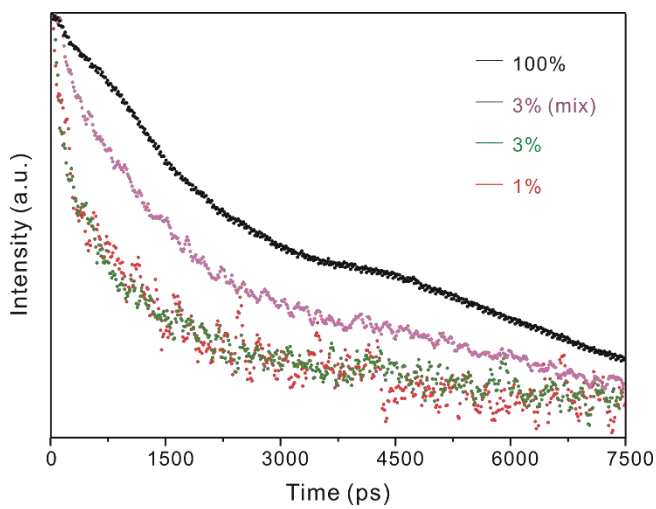

Figure 2-15 PL decay profiles of C/TiO_2 nanocomposites decorated with respectively indicated weight percentages of CQDs. The samples were dispersed in ethanol, excited at 266 nm, and monitored at 450 nm.

The PL decay curves of C/TiO_2 nanocomposites have also been monitored to further examine the charge transfer dynamics across the interface of C/TiO_2

nanocomposites (Figure 2-15). The heterogeneity and surface defects of samples could introduce multi-exponential decay behaviors; all the emission kinetic profiles of C/TiO_2 nanocomposites have been fitted with multi-exponential decay functions, whose time constants are listed in Table 2-1. Compared with the PL lifetime (4300 ps) of as-prepared CQDs, the mean PL lifetimes of C/TiO_2 nanocomposites have been found to be much shorter because of efficient charge separation across the interface between CQDs and TiO_2 nanoparticles. For 3% (mix) C/TiO_2 nanocomposites, while 55% of the PL decays on the time scale of 4300 ps, 45% of the PL decays within 790 ps. This suggests that 45% of excited CQDs in physically adsorbed C/TiO_2 nanocomposites are quenched via charge transfer to the conduction band of adjacent TiO_2 nanoparticles.[6,25] Meanwhile, regardless of the dosages of CQDs, the decay profiles of hydrothermally treated C/TiO_2 nanocomposites have been fitted with lifetimes of 200 (55%) and 2300 ps (45%) to give a mean lifetime of 1100 ps. This suggests that the incorporation of CQDs and TiO_2 nanoparticles with chemical bonds has been obtained by hydrothermal treatment and that the nature of the hybrid structures in C/TiO_2 nanocomposites is the same regardless of the dosages of CQDs. Considering the mean PL lifetime of 1100 ps for C/TiO_2 nanocomposites and the lifetime of 4300 ps for CQDs, we can calculate that the overall transfer time of photo-generated electrons in CQDs into the conduction band of TiO_2 nanoparticles is 1500 ps in C/TiO_2

nanocomposites.[11,25,29] In other words, photo-generated charge carriers can be effectively separated on the time scale of 1500 ps at the interfaces of hydrothermally treated C/TiO_2 nanocomposites owing to the dyade structure; the two components of CQDs and TiO_2 nanoparticles form a joint electronic system.[16,17] We consider that the effective charge transfer nature of C/TiO_2 nanocomposites would enhance the photocatalytic activity of the nanocomposites (see below).[25,27]

Table 2-1

PL decay kinetic constants at 450 nm of various catalysts dispersed in ethanol.

Catalyst	Decay time (ps)	Mean lifetime (ps)
CQDs	4300(100%)	4300
3% (mix) C/TiO_2	790(45%) + 4300(55%)[a]	2700
3% C/TiO_2	200(55%) + 2300(45%)	1100
1% C/TiO_2	200(55%) + 2300(45%)	1100

[a] Initial amplitude percentage of each component.

2.4.5. Photocatalytic activities

The relative fractional abundances of hexavalent chromium species such as H_2CrO_4, $HCrO_4^-$, CrO_4^{2-}, $Cr_2O_7^{2-}$, and $HCr_2O_7^-$ in an aqueous solution are varied with the pH of the solution.[4] For example, at a Cr(VI) concentration of 50 mg L^{-1}, $HCrO_4^-$ and $Cr_2O_7^{2-}$ are abundant species at pH lower than 6.8, whereas at pH above 6.8 CrO_4^{2-} is the dominant component. Of course the absorption wavelength and the numbers of protons and electrons required to completely reduce Cr(VI) to Cr(III) depend on chromium species. Therefore, the initial pH of the solution is important for monitoring the concentration of Cr(VI). The Cr(VI) precursor used in this work is sodium dichromate, so $Cr_2O_7^{2-}$ is the dominant species at first. During the photocatalytic reduction, because holes are not used to reduce Cr(VI), holes can oxidize Cr(III) to Cr(VI). Moreover, the electron-hole recombination can also suppress the photocatalytic reduction of Cr(VI). To exclude these side effects, excess sodium sulfite was added as a sacrificial agent, reacting with the holes or hydroxyl radicals and hindering the electron-hole recombination. Here, excess sodium sulfite used as a sacrificial reagent made the solution basic. Thus, we have monitored the concentration of Cr(VI) by measuring the absorbance of CrO_4^{2-} at 372 nm. One mole of CrO_4^{2-} requires eight moles of protons and three moles of electrons to produce Cr(III) completely: $CrO_4^{2-} + 8H^+ + 3e^- \rightarrow Cr^{3+} + 4H_2O$.

The photocatalytic reduction of Cr(VI) under visible-light has been monitored at ambient conditions to evaluate the photocatalytic activities of C/TiO_2 nanocomposites (Figure 2-16). Whereas the concentration of Cr(VI) was hardly decreased without catalysts or in the dark, it was decreased rapidly with C/TiO_2 nanocomposites under light irradiation. This suggests that C/TiO_2 nanocomposites are photocatalytically effective in reducing Cr(VI) into Cr(III). Figure 2-16 hints that the photocatalytic activity is most efficient when the dosage of CQDs in C/TiO_2 nanocomposites is 3%.

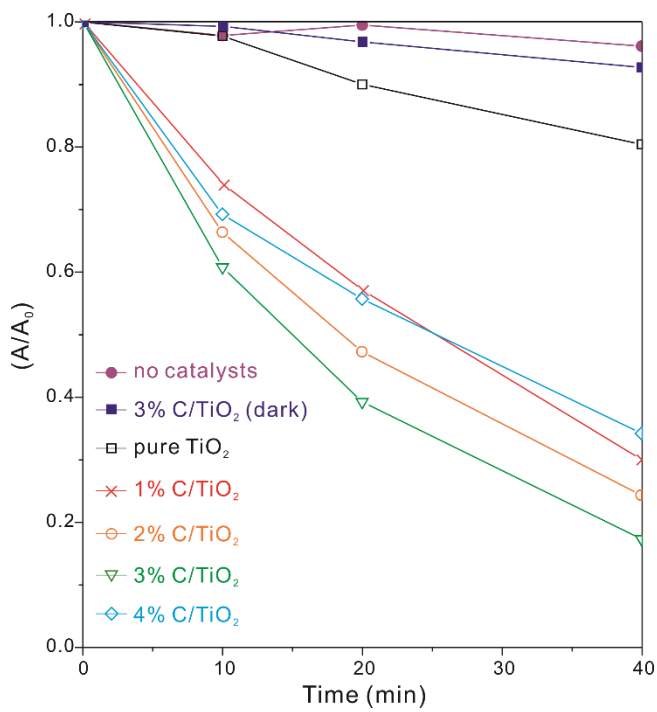

Figure 2-16 Time-dependent concentration changes of aqueous Cr(VI) via indicated photocatalysts.

The first-order kinetic plots of Cr(VI) reduction via photocatalysts under visible-light irradiation have been given in Figure 2-17a and their slopes have yielded the rate constants of the photocatalytic reaction in Table 2-2. With pure TiO_2 nanoparticles, 19% Cr(VI) was reduced after 40 min of irradiation although TiO_2 nanoparticles do not show any absorption in the visible-light region. The photoexcitation of Cr(VI) has contributed to the photocatalytic reduction; CrO_4^{2-} has an absorption band centered at 372 nm so it can response to visible light. Therefore, the photoexcited electrons of CrO_4^{2-} can be transferred to the conduction band of TiO_2. Then, they can be subsequently captured by other Cr(VI) ions, resulting in the reduction of Cr(VI) into Cr(III); when we used 455+ nm cutoff filter instead of a 420+ nm filter, we could not observe any evident decay of the Cr(VI) concentration in the period of 80 min. Figure 2-17b shows that the photocatalytic activity of C/TiO_2 nanocomposites in the reduction of Cr(VI) increases gradually with the content of CQDs, reaches to the maximum value when the dosage of CQDs becomes 3%, and then decreases with a further dosage increase of CQDs. Because excessive CQDs can aggregate without forming chemical bonds with TiO_2 nanoparticles, they can act as charge-recombination centers instead of electron donors.[27] Table 2-2 reveals that the observed photocatalytic reduction rate constant of 3% C/TiO_2 nanocomposites (0.0449 min^{-1}) is 8.6 times higher than that of pure TiO_2 nanoparticles. This indicates that the hybrid structure of CQDs and TiO_2

nanoparticles extensively improves the photocatalytic activity of TiO_2 nanoparticles under visible light.

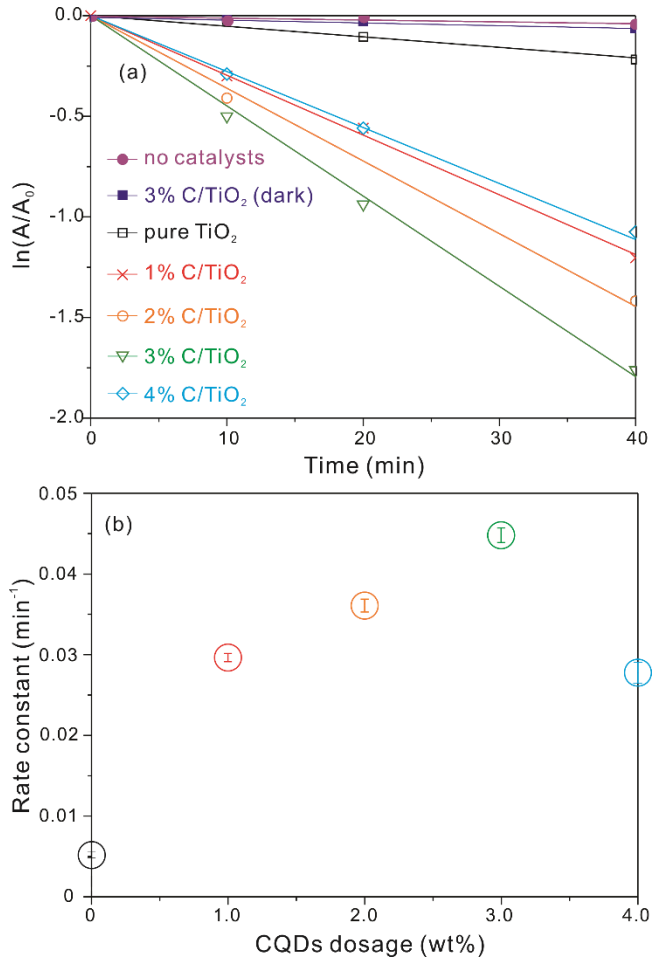

Figure 2-17 First-order kinetic profiles (a) and reduction rate constants (b) of Cr(VI) via indicated catalysts under visible light.

Table 2-2

Catalytic reduction rate constants of Cr(VI) via photocatalysts under visible light.

Catalyst	CQDs dose (wt%)	k (10^{-3} min^{-1})
No catalysts	-	0.917
3% C/TiO_2 (dark)	3.0	1.70
Pure TiO_2	0.0	5.25
1% C/TiO_2	1.0	29.7
2% C/TiO_2	2.0	36.1
3% C/TiO_2	3.0	44.9
4% C/TiO_2	4.0	27.8

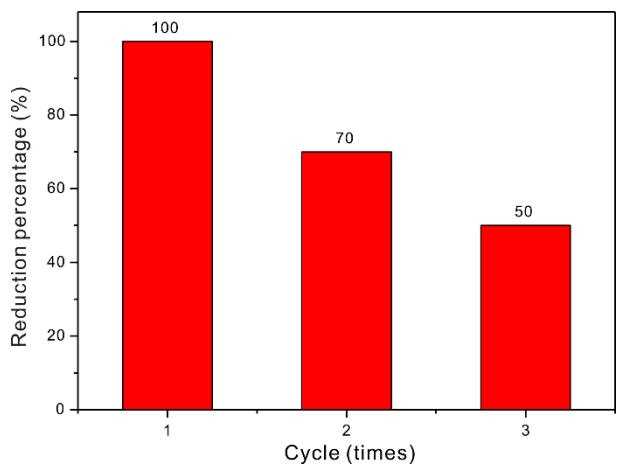

Figure 2-18 Cr(VI) reduction performances of 3% C/TiO_2 nanocomposites for three cycles.

The durability and stability of 3% C/TiO_2 nanocomposites have been monitored via the recycling tests of photocatalysts (Figure 2-18). After three cycles, 50% of the photocatalytic reduction efficiency has decreased due to Cr(VI) ions and

oxide/hydroxide forms of Cr(III) such as $Cr(III)_xO_y$ and $Cr(OH)_3$ adsorbed on the surfaces of C/TiO_2 nanocomposites.[1,7,9] By measuring ICP-MS data, we have confirmed that the amount of residually adsorbed Cr species after the first cycle is 8.2 mg g^{-1}.

Considering all our photocatalytic data, we can propose the photocatalytic reduction mechanism of Cr(VI) over C/TiO_2 nanocomposites as follows (Figure 2-1): when C/TiO_2 nanocomposites are excited by visible light, photo-generated electrons transfer from CQDs into the conduction band of TiO_2 on the time scale of 1500 ps, and then they are captured by Cr(VI) ions, reducing Cr(VI) into Cr(III). During the photocatalytic process under visible light, π-conjugated CQDs act as sensitizers like organic dyes to provide visible-light response to the TiO_2 nanoparticles of C/TiO_2 dyade structures, leading to the enhanced photocatalytic reduction of Cr(VI).[13]

2.5. Conclusions

Carbon quantum dots (CQDs) having sizes of 5-10 nm were prepared facilely by a hydrothermal method, then incorporated with TiO_2 nanoparticles with various dosages of CQDs to produce CQDs-decorated TiO_2 (C/TiO_2) nanocomposites. The incorporation of CQDs with TiO_2 has been achieved via hydrothermal treatment. Two components of CQDs and TiO_2 nanoparticles in C/TiO_2 nanocomposites have been directly combined without using any other chemical linker materials. Direct contact at interfaces without having insulating layers is beneficial to charge transfer in dyade structures. Under visible-light irradiation, the photocatalytic activities of Cr(VI) reduction via C/TiO_2 nanocomposites have been monitored and found to depend highly on the dose of CQDs. The photocatalytic rate constant of 3% C/TiO_2 nanocomposites (0.0449 min^{-1}) has been found to be 8.6 times higher than that of pure TiO_2 nanoparticles. When CQDs are excited by visible light, photo-generated electrons transfer from CQDs into the conduction band of TiO_2 on the time scale of 1500 ps. Transferred electrons are subsequently captured by Cr(VI) ions, reducing Cr(VI) into Cr(III). CQDs in C/TiO_2 nanocomposites play an important role for the photocatalytic reduction of Cr(VI). Under visible-light irradiation, π-conjugated CQDs act as sensitizers like organic dyes to provide visible-light response to the TiO_2 nanoparticles of C/TiO_2 dyade structures, leading to the highly efficient

photocatalytic reduction of Cr(VI). Overall, we can suggest that our as-prepared C/TiO_2 nanocomposites may be applied to treat wastewater by utilizing solar energy in an inexpensive way without employing electron donors.

2.6. Acknowledgements

This work was financially supported by the National Research Foundation of Korea (research grants: 2015-051798 and 2017-006153).

2.7. References

[1] W. Ji, J. Qu, C.-A. Li, J.-W. Wu, S. Jing, F. Gao, Y.-N. Lv, C. Liu, D.-R. Zhu, X.-M. Ren, *Appl. Catal. B: Environ.*, **2017**, 205, 368.

[2] M. Zheng, Z. Xie, D. Qu, D. Li, P. Du, X. Jing, Z. Sun, *ACS Appl. Mater. Interfaces*, **2013**, 5 13242.

[3] J. Wu, J. Wang, Y. Du, H. Li, Y. Yang, X. Jia, *Appl. Catal. B: Environ*., **2015**, 174, 435.

[4] B.A. Marinho, R.O. Cristóvão, R. Djellabi, J.M. Loureiro, R.A.R. Boaventura, V.J.P. Vilar, *Appl. Catal. B: Environ*., **2017**, 203, 18.

[5] Y. Li, Y. Bian, H. Qin, Y. Zhang, Z. Bian, *Appl. Catal. B: Environ.*, **2017**, 206, 293.

[6] F. Liu, J. Yu, G. Tu, L. Qu, J. Xiao, Y. Liu, L. Wang, J. Lei, J. Zhang, *Appl. Catal.*

B: Environ., **2017**, 201, 1.

[7] Y. Yang, G. Wang, Q. Deng, D.H. Ng, H. Zhao, *ACS Appl. Mater. Interfaces*, **2014**, 6, 3008.

[8] M. Qamar, M. Gondal, Z. Yamani, *J. Mol. Catal. A*, **2011**, 341, 83.

[9] J. Qu, D. Chen, N. Li, Q. Xu, H. Li, J. He, J. Lu, *Appl. Catal. B: Environ.*, **2017**, 207, 404.

[10] S. Wang, L. Yi, J.E. Halpert, X. Lai, Y. Liu, H. Cao, R. Yu, D. Wang, Y. Li, *Small*, **2012**, 8, 265.

[11] J. Sun, H. Zhang, L.-H. Guo, L. Zhao, *ACS Appl. Mater. Interfaces*, **2013**, 5, 13035.

[12] H.-B. Kim, D.-J. Jang, *CrystEngComm*, **2015**, 17, 3325.

[13] H. Yu, Y. Zhao, C. Zhou, L. Shang, Y. Peng, Y. Cao, L.-Z. Wu, C.-H. Tung, T. Zhang, *J. Mater. Chem. A*, **2014**, 2, 3344.

[14] J. Tian, Y. Leng, Z. Zhao, Y. Xia, Y. Sang, P. Hao, J. Zhan, M. Li, H. Liu, *Nano Energy*, **2015**, 11, 419.

[15] N.C.T. Martins, J. Ângelo, A.V. Girão, T. Trindade, L. Andrade, A. Mendes, *Appl. Catal. B: Environ*. 2016, 193, 67.

[16] D. Lu, P. Fang, W. Wu, J. Ding, L. Jiang, X. Zhao, C. Li, M. Yang, Y. Li, D. Wang, *Nanoscale*, **2017**, 9, 3231.

[17] L. Zhao, X. Chen, X. Wang, Y. Zhang, W. Wei, Y. Sun, M. Antonietti, M.M. Titirici, *Adv. Mater*., **2010**, 22, 3317.

[18] Y. Wang, A. Hu, *J. Mater. Chem. C*, **2014**, 2, 6921.

[19] S.Y. Lim, W. Shen, Z. Gao, *Chem. Soc. Rev*., **2015**, 44, 362.

[20] H. Li, X. He, Z. Kang, H. Huang, Y. Liu, J. Liu, S. Lian, C.H.A. Tsang, X. Yang, S.T. Lee, *Angew. Chem. Int. Ed*., **2010**, 49, 4430.

[21] S.N. Baker, G.A. Baker, *Angew. Chem. Int. Ed*., **2010**, 49, 6726.

[22] K. Jiang, S. Sun, L. Zhang, Y. Lu, A. Wu, C. Cai, H. Lin, *Angew. Chem. Int. Ed*., **2015**, 54, 5360.

[23] S. Zhu, Q. Meng, L. Wang, J. Zhang, Y. Song, H. Jin, K. Zhang, H. Sun, H. Wang, B. Yang, *Angew. Chem. Int. Ed*., **2013**, 52, 3953.

[24] K.S. Fernando, S. Sahu, Y. Liu, W.K. Lewis, E.A. Guliants, A. Jafariyan, P. Wang, C.E. Bunker, Y.-P. Sun, *ACS Appl. Mater. Interfaces*, **2015**, 7, 8363.

[25] J. Lee, Y. Kim, J.K. Kim, S. Kim, D.-H. Min, D.-J. Jang, *Appl. Catal. B: Environ*., **2017**, 205, 433.

[26] D. Choi, J.-Y. Pyo, Y. Kim, D.-J. Jang, *J. Mater. Chem. C*, **2015**, 3, 3286.

[27] S. Ham, Y. Kim, M.J. Park, B.H. Hong, D.-J. Jang, *RSC Adv*., **2016**, 6, 24115.

[28] P. Yu, X. Wen, Y.-R. Toh, J. Tang, *J. Phys. Chem. C*, 2012, 116, 25552.

[29] J.K. Kim, D.-J. Jang, J, *Mater. Chem. C*, **2017**, 5, 6037.

Chapter 3. Photodeposition of Gold Nanoparticles on Silica Nanospheres using Carbon Dots as Excellent Electron Donors †

† This is reproduced from Dayeon Choi and Du-Jeon Jang, *New J. Chem.*, **2018,** *42(18)*, 14717-14720.

3.1. Abstract

Gold nanoparticles have been photodeposited on the surfaces of SiO2 nanospheres directly by adopting carbon dots as photoexcited-electron donors at room temperature. The sizes of gold nanoparticles have been facilely and eco-friendly controlled by adjusting the irradiation time.

3.2. Introduction

Nanoparticles of noble metals such as gold, silver, and platinum attract great attention owing to their unique properties and diverse applications.[1-4] Their properites can be tunned by controlling sizes, shapes, and compositions. For various applications, noble-metallic nanoparticles need to be stable against the surrounding environment. However, they are unstable in aqueous solutions, so they tend to be aggrerated each other. Therefore, they need to be stabilized with surfactants or to be spatially separated.

Silica (SiO_2) is a well-known support material for nanoparticles of metals and metal oxides. Also, compared with other semiconductors such as TiO_2, silica is considered to be relatively inert. Therefore, silica has been often used as hard templates to make hollow structures, as shell materials to protect core materials,

and as spacers to make a distance between two materials.[5-7]

There are several methods to deposit metal nanoparticles onto semiconductors, such as impregnation, electrodeposition, sputtering, and atomic-layer deposition (ALD). However, these techniques demand elevated temperatures or applied voltages. Especially, metal nanoparticles can be grown onto SiO_2 nanospheres via the chemical reduction of 'seed-mediated growth'.[6] However, this synthesis in a solution requires a quite time-consuming process; (a) surface modification of silica with chemicals such as amine or thiol groups, (b) synthesis of uniform seeds, (c) attachment of the seeds onto silica, and (e) growth of the seeds to form nanoparticles. Moreover, seed-mediated growth is struggling with size control. The sizes of metal nanoparticles are very important to determine their properties so that proper capping agents are used to overcome drawbacks.[7] These chemicals have caused additional environmental problems so it is necessary to study facile and eco-friendly synthetic strategies for growing metal nanoparticles onto silica with controlled sizes. Nevertheless, a few studies regarding the direct growth of metal nanoparticles onto non-functionalized silica with reducing agents have been reported.[6] However, there is no report regarding the direct photodeposition of metal nanoparticles onto silica so far because the band-gap energy (~9.0 eV) of SiO_2 is too high for photodeposition.

Carbon dots (Cdots) as appealing zero-dimensional nanostructures possess

chemical stability and show electron-transfer and electron-reservoir properties.[8-14] Such unique photo-induced electron-transfer properties make Cdots photoactive nanomaterials. In addition, Cdots contain hydrophilic carboxyl and hydroxyl groups so that they have excellent water solubility. Such fascinating properties offer Cdots opportunities to be used as photoactive nanocatalysts.[11] Typically, Cdots have been applied in the photodegradation of organic contaminants by constructing complex photocatalysts such as Cdots/TiO_2, Cdots/SiO_2, Cdots/Fe_2O_3, Cdots/ZnO, and Cdots/Cu_2O.[15-17] In our previous work, Cdots/TiO_2 nanocomposites have been successfully prepared and applied to reduce Cr(VI); Cdots have acted as sensitizers to provide visible-light response to TiO_2 nanoparticles.[15] .

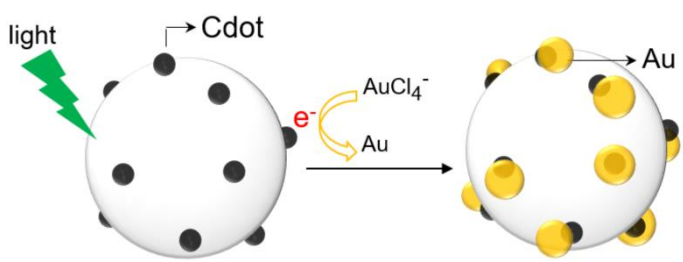

Figure 3-1 Schematic for the fabrication of a Au/Cdots-SiO_2 nanocomposite via photodeposition with the assistance of Cdots as electron donors.

In this communication, for the first time we report the photodeposition of gold nanoparticles on SiO_2 nanospheres directly by adopting Cdots as electron donors at room temperature (Figure 1). The photodeposition method offers several

advantages.[18-20] First, the percentage yield of the photodeposition method is higher than that of any chemical methods. And, metallic nanoparticles having uniform sizes can be easily produced; their sizes can be controlled by adjusting the irradiation time. Moreover, this eco-friendly method needs neither any additional reducing agents, capping agents, nor ligands; simply light does everything.[21,22] As a result, metallic nanoparticles can be tightly anchored to silica. So, the adoption of Cdots as electron donors has been proved to be an efficient way to prepare metal-semiconductor hybrids, where the semiconductor may be photoactive or not.

3.3 Experimental

3.3.1. Materials

All chemicals were used as received: $HAuCl_4 \cdot 3H_2O$ (s, 99.9%), tetraethyl orthosilicate (TEOS, l, ≥99%), 28-30% NH_4OH(aq), 3-aminopropyl triethoxysilane (APTES, l, >98%), citric acid (s, 99.5%) from Sigma-Aldrich. Isopropyl alcohols (IPA, l) and ethanol(l) were from Dajeong Chemicals, and purified water (>15 MΩcm) from an ELGA PURELAB Option-S system was used throughout the experiments.

3.3.2. Preparation

Preparation of SiO_2 nanospheres. Hard supporters of silica nanospheres were prepared via the sol-gel reaction of TEOS under base catalysis following the Stöber method.[5] 50 mL of ethanol, 3.55 mL of water, 3.1 mL of TEOS, and 3.25 mL of 28-30% NH_4OH(aq) were mixed and stirred vigorously overnight. The product was centrifuged at 9,000 rpm for 10 min, rinsed three times with water and ethanol, and then dried at 60 °C for 5 h.

Synthesis of Cdots-decorated SiO_2 (Cdots-SiO_2) nanocomposites. Firstly, the surface modification of SiO_2 nanospheres with APTES was performed to synthesize Cdots directly on surfaces of SiO_2 nanospheres. 100 mg of as-prepared SiO_2 nanospheres was dispersed in 19.5 mL of IPA with sonication. Then, the mixture was added with 0.50 mL of APTES and stirred at 60 °C for 2 h. Then, produced APTES-modified SiO_2 nanospheres were centrifuged at 9,000 rpm for 10 min, washed with IPA several times to remove remaining APTES, and re-dispersed in 20 mL of IPA. Then, 0.10 mmol of citric acid was dissolved in 10 mL of water and added to the above colloidal solution of APTES-modified SiO_2 nanospheres. The resultant mixture was stirred for 10 min, transferred into a Teflon-lined stainless-steel autoclave of 50 ml, and maintained at 180 °C for 3 h. After the

reaction, the autoclave was cooled down to room temperature, and the product was centrifuged, rinsed three times with ethanol, and re-dispersed in 5.0 mL of ethanol to produce a 20 g L^{-1} Cdots-SiO_2 colloidal solution.

Photodeposition of gold nanoparticles on Cdots-SiO_2 nanocomposites. Au/Cdots-decorated SiO_2 nanocomposites were synthesized by phtodepositing gold on surfaces of Cdots-SiO_2 nanocomposites under light irradiation. 15 mL of water and 5.0 mL of ethanol, and 10 μL of the as-prepared Cdots-SiO_2 colloidal solution were mixed. The mixture was transferred into a quartz reactor, stirred for 10 min, placed 30 cm away from a 300 W Schoeffel LPS 255 HR xenon arc lamp with a focusing lens, and irradiated for a few seconds with stirring. The reaction was started by the addition of a specific amount of a $HAuCl_4$ stock solution (12.7 mM in ethanol) and stopped by turning off the Xe lamp; the concentration of the gold precursor in 20 mL of the final photodeposition reaction mixture was 6.35 μM and the light intensity at 250 nm was 327 mW. Then, the product was separated by centrifugation at 12,000 rpm for 10 min, washed with ethanol, and re-dispersed in ethanol. Hereafter, the product of Au/Cdots-decorated SiO_2 nanocomposites will be designated as Au/Cdots-SiO_2 nanocomposites.

3.3.3. Characterization

While transmission electron microscopy (TEM) images were measured using a Hitachi H-7600 microscope operating at 100 kV, high-resolution TEM (HRTEM) images and energy-dispersive X-ray (EDX) elemental mappings were measured utilizing a JEOL JEM-2100F microscope. Absorption spectra were measured using a Scinco S3100 UV-vis spectrophotometer, and field-emission scanning electron microscopy (FE-SEM) images were obtained with a ZEISS MERLIN Compact microscope. Light intensities were detected using a Gentec-EO Integra photodetector.

3.4. Results and discussion

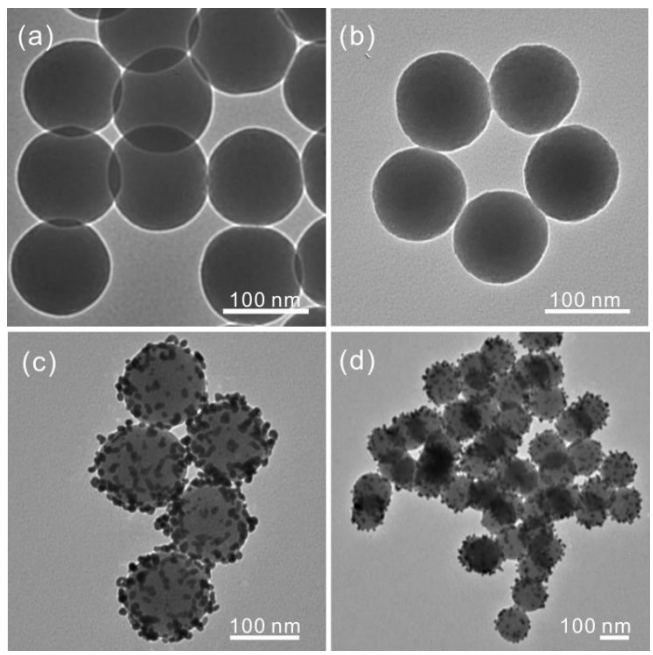

Figure 3-2 TEM images of SiO_2 nanospheres (a), Cdots-SiO_2 nanocomposites (b), and Au/Cdots-SiO_2 nanocomposites (c,d).

Figure 3-2a shows a normal TEM image of SiO_2 nanospheres, which have a good monodispersity with an average diameter of about 100 nm. Monodispersive supporters of SiO_2 nanospheres were prepared following the Stöber method.[5] To prepare Cdots onto SiO_2 nanospheres, a hydrothermal reaction was conducted with citric acid and APTES as precursors. During the hydrothermal reaction, the precursors were condensed via forming amide bonds, producing polymer-like

Cdots, which were then carbonized at high temperature (Figure 3-3).[15] The overall sizes of as-prepared Cdots-SiO_2 nanocomposites, depicted in Figure 3-1b, were the same as the diameters of SiO_2 nanospheres. A close examination indicates that the surfaces of Cdots-SiO_2 nanocomposites are rougher than those of SiO_2 nanospheres. This suggests that Cdots have been formed on SiO_2 nanospheres. However, due to the relatively small sizes of Cdots over supporter SiO_2 nanospehres, Cdots could be hardly discriminated from SiO_2 nanospheres in normal TEM images.[25] Alternatively, the absorption spectra of Figure 3-4 are helpful to identify the existence of Cdots on SiO_2 nanospheres. Compared with the absorption spectrum of SiO_2 nanospheres, that of Cdots-SiO_2 nanocomposites shows enhanced absorbance in the UV-visible region, indicating that Cdots have been produced on SiO_2 nanospheres.[15] Then, we have decorated Cdots-SiO_2 nanocomposites with gold nanoparticles by photodeposition. As shown in Figure 3-2c, gold nanoparticles having uniform sizes of ~10 nm have been deposited successfully onto Cdots-SiO_2 nanocomposites, forming Au/Cdots-SiO_2 nanocomposites. The low-magnified TEM image of Figure 3-2d also indicates that gold nanoparticles have been deposited evenly onto Cdots-SiO_2 nanocomposites by the photodeposition method.

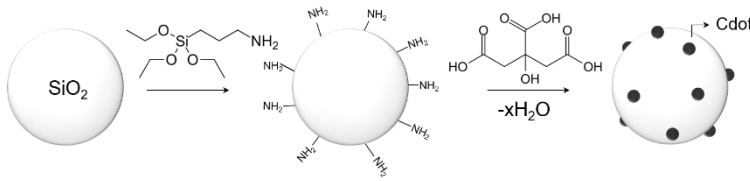

Figure 3-3 Synthetic route of a Cdots-SiO_2 nanocomposite using citric acid and APTES.

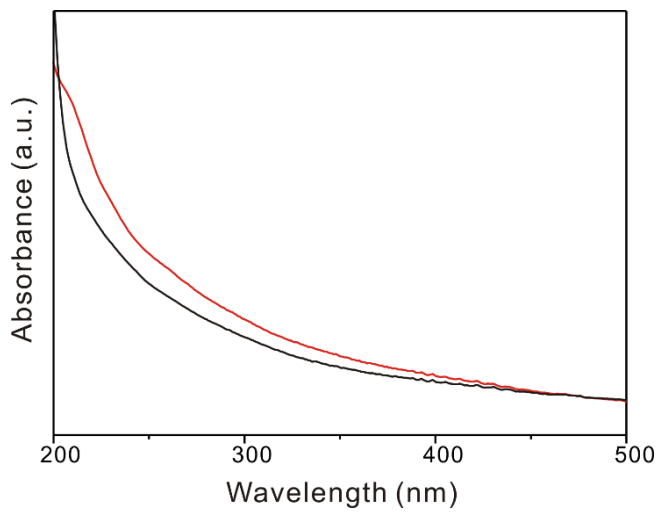

Figure 3-4 Absorption spectra of SiO_2 nanospheres (black) and Cdot-SiO_2 nanocomposites (red).

The FE-SEM images of Figure 3-5 display the surfaces of nanostructures very clearly. The surfaces of Cdots-SiO_2 nanocomposites in Figure 3-5b is rougher than the surfaces of SiO_2 nanospheres in Fig 3-5a, supporting that Cdots have been deposited on SiO_2 nanospheres by the hydrothermal treatment. Also, Fig 3-5c

indicates that gold nanoparticles have been adequately deposited on the Cdots-SiO_2 nanocomposites without being aggregated, demonstrating that Cdots can be used as excellent electron donors for the photodeposition of gold.

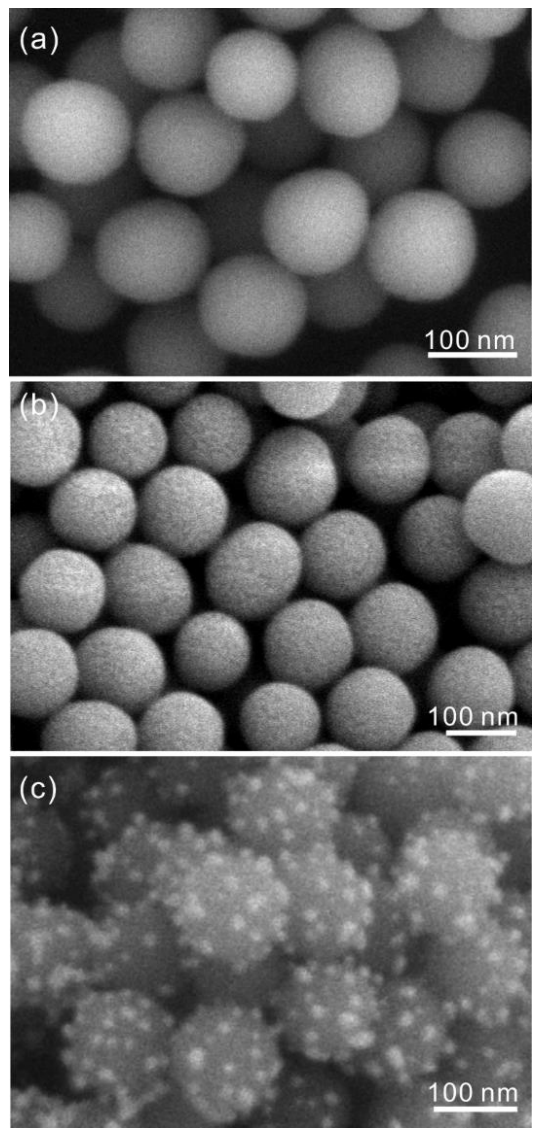

Figure 3-5 FE-SEM images of SiO_2 nanospheres (a), Cdots-SiO_2 nanocomposites (b), and Au/Cdots-SiO_2 nanocomposites (c).

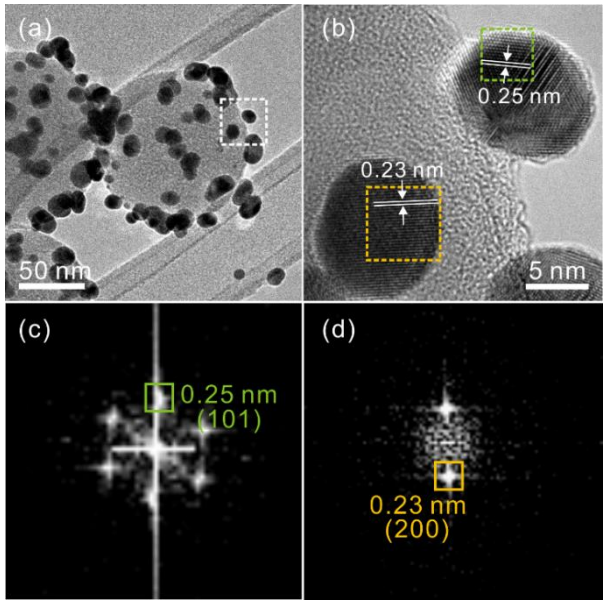

Figure 3-6 HRTEM image (a), enlarged HRTEM image (b), and FFT patterns (c,d) of Au/Cdots-SiO_2 nanocomposites; the FFT patterns of (c) and (d) were obtained from the green and the yellow regions, respectively, of (b).

The HRTEM images of Figure 3-6 provide the detailed information of gold nanoparticles decorated on SiO_2 nanospheres. Gold nanoparticles on Cdots-SiO_2 nanocomposites have spherical shapes with an average diameter of ~10 nm. The selected area of Au/Cdots-SiO_2 nanocomposites in the white box of Figure 3-6a has been enlarged; unfortunately, it is not possible for us to identify the intrinsic lattices of Cdots even with highly magnified HRTEM images. Figure 3b displays that the averaged d-spacing values of 0.25 and 0.23 nm, which match well with the standard spacings of 0.249 and 0.230 nm between the (101) and (200) planes of

gold, respectively.[27] The green and yellow regions in Fig 3-6b yield the FFT patterns of Figure 3c and Figure 3-6d, respectively, which can be indexed to the (101) and (200) planes of gold, respectively. In addition, the FFT patterns of Figure 3-6d show discrete spots, suggesting that photodeposited gold nanoparticles have relatively good crystallinity. Based on the structural analysis of Figure 3-6, we can conclude that gold nanoparticles with good crystallinity have been successfully photodeposited on the surfaces of silica nanospheres using Cdots as electron donors.

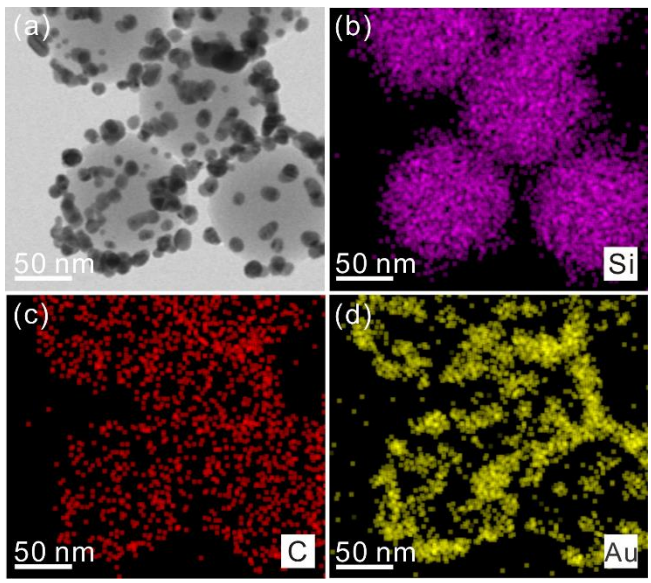

Figure 3-7 HRTEM image (a), and EDX elemental maps (b-d) of Au/Cdots-SiO_2 nanocomposites.

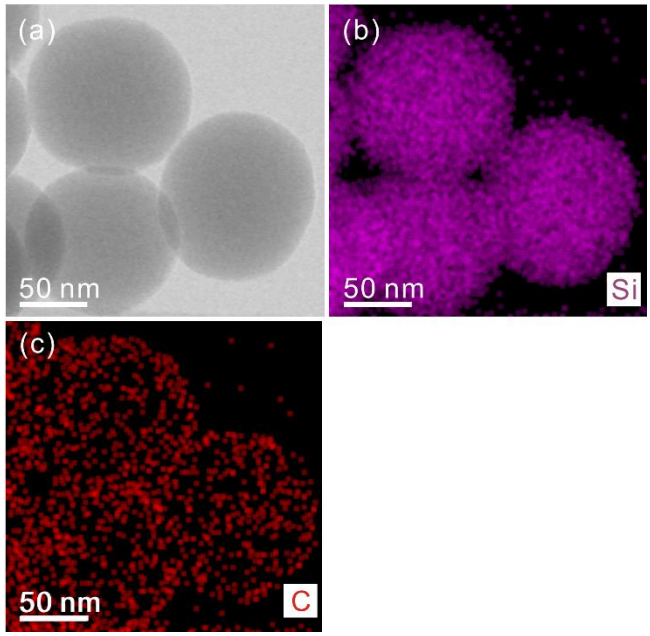

Figure 3-8 HRTEM image (a) and EDX elemental maps (b,c) of Cdots-SiO_2 nanocomposites.

The HRTEM images and EDX elemental maps of Figs. 3-7 and 3-8 reveal that Cdots have been evenly prepared on the surfaces of SiO_2 nanospheres by hydrothermal treatment and that gold nanoparticles, which have an average diameter of ~10 nm, have been photodeposited well on Cdots-SiO_2 nanocomposites, suggesting once more that Cdots can be used as excellent nucleation sites and electron donors for the photodeposition of gold nanoparticles.

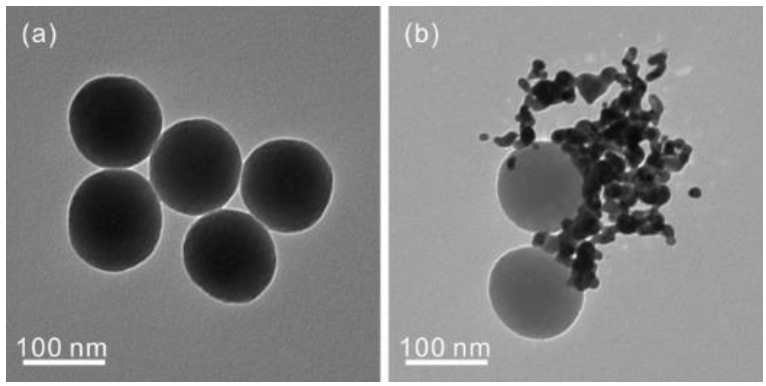

Figure 3-9 TEM images of Au/Cdots-SiO_2 nanocomposites prepared with Cdots-SiO_2 nanospheres under the dark (a) and with Cdots-free SiO_2 nanospheres under light irradiation (b).

Control experiments have been performed to understand the roles of Cdots (Figure 3-9). We tried to deposit gold nanoparticles onto Cdots-SiO_2 nanocomposites under the dark or with Cdots-free SiO_2 nanospheres while the other experimental conditions were retained throughout the experiments. In both cases, gold nanoparticles could not been deposited onto the SiO_2 nanospheres satisfactorily. As displayed in Figure 3-9a, the gold precursor of $AuCl_4^-$ in the absence of light was not reduced to form gold nanoparticles at all, suggesting that Cdots can act as electron donors only with light for the reduction of the gold precursor. Similarly, Figure 3-9b indicates that gold nanoparticles could not be deposited onto Cdots-free SiO_2 nanospheres even if light was irradiated; gold nanoparticles were produced but aggregated in the solvent due to the direct

photoexcitation of dissolved $AuCl_4^-$ species. Based on these control experiments, we can suggest that under irradiation, Cdots can act as electron donors and nucleation sites simultaneously, producing Au/Cots-SiO_2 nanocomposites.

Typically, the growth of nanoparticles has taken place in two steps: seed nucleation and growth. And, there are several conditions for efficient photodeposition. 1) Proper energy levels of the semiconductor; the reduction potential of the metal to be reduced and the oxidation potential of the sacrificial agent to be oxidized must be in favorable positions. 2) The incident light needs to have a sufficient energy to exceed the band gap energy of the semiconductor. 3) Charge carriers need to be separated to migrate effectively. 4) Sufficient nucleation sites are required for photodeposition. Thus, we have conducted the following additional control experiments with variation of incident light intensities, solvents, and irradiation intervals.

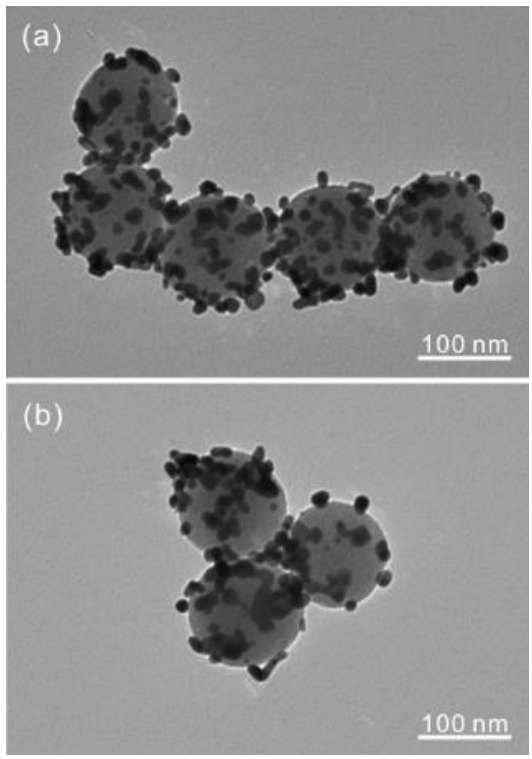

Figure 3-10 TEM images of as-prepared Au/Cdots-SiO_2 nanocomposites prepared via photodeposition at light intensities of 111 mW (a) and 57 mW (b).

Compared with Au/Cdots-SiO_2 nanocomposites prepared at 327 mW (Figure 3-2c), those prepared at 111 mW (Figure 3-10a) and at 57 mW (Figure 3-10b) are decorated with relatively larger gold nanoparticles having irregular shapes. Moreover, distances among gold nanoparticles of Au/Cdots-SiO_2 nanocomposites increase gradually as the light intensity decreases. This suggests that the gold precursor prefers to be reduced at existing gold seeds rather than at new nucleation sites because it is hard to make new gold seeds at weak light intensities. From these

experiments, we can conclude that the light intensity is an important factor for the photodeposition of gold nanoparticles having uniform sizes and shapes; the more intense light is, the denser and more uniform gold nanoparticles are produced.

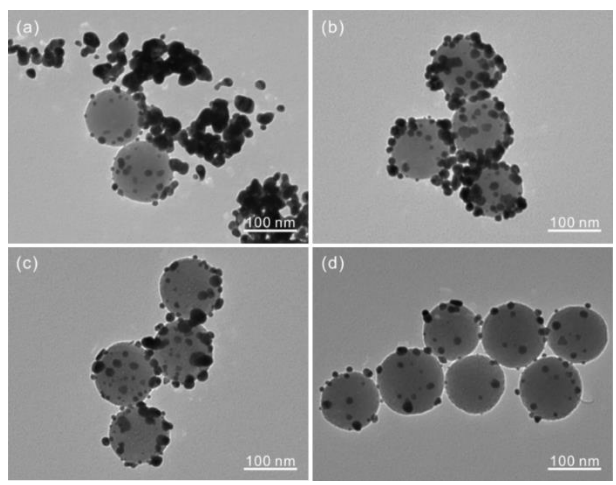

Figure 3-11 TEM images of as-prepared Au/Cdots-SiO_2 nanocomposites prepared via photodeposition in 20 mL of various ethanol-water solutions: $V_{ethanol}$ / V_{water} values are 0/20 (a), 10/10 (b), 15/5 (c), and 20/0 (d).

The effects of solvents were also investigated by varying the volume percentage of ethanol in an ethanol-water solution, where ethanol was used as hole scavengers. When $V_{ethanol}$ / V_{water} was 0/20, large gold nanoparticles were produced but aggregated in the solvent (Figure 3-11a). In this case, because ethanol acting as hole scavengers was absent, the photoexcited electrons of Cdots returned rapidly to ground states without reducing $AuCl_4^-$ to form Au/Cdots-SiO_2 nanocomposites.

As photoexcited gold precursor ions of $AuCl_4^-$ are unstable in water, they tend to be reduced and aggregated. However, the addition of ethanol led to a completely different result. A small amount of ethanol can scavenge holes effectively, so photoexcited electrons can be accumulated on the surfaces of Cdots-SiO_2 nanocomposites, resulting in the reduction of gold precursor species onto the surfaces of SiO_2 nanospheres. Nevertheless, too much accumulation of electrons at $V_{ethanol}$ / V_{water} values of 10/10 (Figure 3-11b) and 15/5 (Figure 3-11c) can cause to enlarge gold nanoparticles too much. Besides, dissolved oxygen molecules can also affect the overall photodeposition process as they can act as scavengers of photoexcited electrons produced at the surfaces of Cdots-SiO_2 nanocomposites; at standard temperature and pressure, the concentrations of dissolved oxygen in ethanol and water are 2.10 and 0.26 mM, respectively.[19] At a high concentration of dissolved oxygen, photoinduced electrons can be scavenged by dissolved oxygen, decreasing electrons accumulated in the surface of Cdots-SiO_2 nanocomposites. Therefore, the amount of electrons on Cdots-SiO_2 nanocomposites is small at $V_{ethanol}$ / V_{water} of 20/0, so a small amount of gold nanoparticles having tiny sizes has been produced on the surfaces of SiO_2 nanospheres (Figure 3-11d). The TEM images of Figure 3-11 reveal the significance of ethanol acing as a sacrificial agent in the photodeposition. The sacrificial agent helps charge carriers to be separated effectively, leading to the formation of gold nanoparticles onto Cdots-SiO_2

nanocomposites. So, we can conclude that by adjusting the amount of the sacrificial agent, we can change the sizes and shapes of gold nanoparticles approximately.

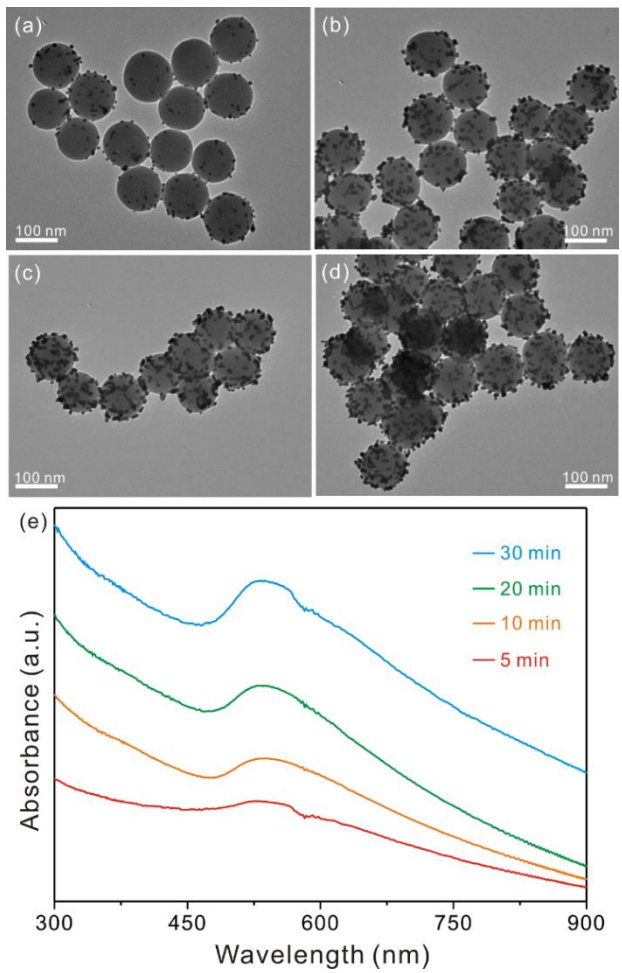

Figure 3-12 TEM images of as-prepared Au/Cdots-SiO_2 nanocomposites via photodeposition for 5 min (a), 10 min (b), 20 min (c), and 30 min (d), and absorption spectra of as-prepared Au/Cdots-SiO_2 nanocomposites prepared via photodeposition for respectively indicated times (e).

We have also investigated the time dependence of the gold deposition (Figure 3-12). The TEM image of Figure 3-12a shows that tiny gold nanoparticles were photodeposited onto SiO_2 nanospheres at an early stage of 5 min, forming nucleation seeds. Until 10 min (Figure 3-12b), the surfaces of SiO_2 nanospheres were decorated densely with gold nanoparticles because additional $AuCl_4^-$ ions were reduced on the surface of Cdots-SiO_2 nanocomposites to form Au/Cdots-SiO_2 nanocomposites. After 10 min (Figure 3-12c,d), the gold precursor preferred to be reduced at existing gold seeds rather than at new nucleation sites. Thus, existing gold seeds grew to cover the surfaces of Cdots-SiO_2 nanocomposites uniformly. By monitoring the surface plasmon absorption band of gold centered at ~530 nm, we can also verify the existence of gold nanoparticles (Figure 3-12e). The absorption spectrum at 5 min displays the surface plasmon band of gold nanoparticles, indicating the nucleation of gold seeds onto Cdots-SiO_2 nanocomposites already at an early stage. The absorbance increased gradually with the time, indicating the size increase of gold seeds. The gold precursor of $AuCl_4^-$ needs three electrons to be reduced into a gold atom. Thus, researchers usually have used two kinds of reducing agents for efficient redcution.[23] Compared with the typical methods, our method employs only Cdots and light irradiation to reduce the gold precursor facilely, indicating Cdots can be used as excellent photoinduced-electron donors.

3.5. Conclusion

Cdots were prepared on SiO_2 nanospheres having diameters of ~100 nm by a hydrothermal method to produce Cdots-SiO_2 nanocomposites, then gold nanoparticles having sizes of ~10 nm were deposited on Cdots-SiO_2 nanocomposites facilely via a photodeposition method to produce Au/Cdots-SiO_2 nanocomposites; two components of gold nanoparticles and SiO_2 nanospheres were directly combined without using any chemicals. Under light irradiation, the photoinduced electrons of Cdots could reduce the gold precursor of $AuCl_4^-$ on the surfaces of SiO_2 nanospheres; Cdots could act as electron donors and reaction sites simultaneously. And, the average size of gold nanoparticles could be controlled easily by adjusting the irradiation period. Overall, the adoption of Cdots as electron donors and nucleation sites has been proved to be an efficient and eco-friendly way to prepare metal-semiconductor hybrids, where the semiconductor may be photoactive or not.

2.6. Acknowledgements

This work was financially supported by the National Research Foundation of Korea (research grant: 2017-006153).

3.7. References

[1] M. Son, S. Jeong, D.-J. Jang, *J. Phys. Chem. C*, **2014**, 118, 5961.

[2] A.M. Brito-Silva, R.G. Sobral-Filho, R. Barbosa-Silva, C.B. de Araújo, A. Galembeck, A.G. Brolo, *Langmuir*, **2013**, 29, 4366.

[3] T.-H. Park, H. Lee, J. Lee, D.-J. Jang, *RSC Adv*., **2017**, 7, 7718.

[4] F. Akbarian, B.S. Dunn, J.I. Zink, *J. Phys. Chem.*, **1995**, 99, 3892.

[5] Y. Kim, H.-B. Kim, D.-J. Jang, *J. Mater. Chem. A*, **2014**, 2, 5791.

[6] J. Lee, D.-J. Jang, *RSC Adv*., **2015**, 5, 64268.

[7] J.K. Kim, D.-J. Jang, *J. Mater. Chem. C*, **2017**, 5, 6037.

[8] Y. Wang, A. Hu, *J. Mater. Chem. C*, **2014**, 2, 6921.

[9] G.A. Hutton, B.C. Martindale, E. Reisner, *Chem. Soc. Rev.*, **2017**, 46, 6111.

[10] S.Y. Lim, W. Shen, Z. Gao, *Chem. Soc. Rev.*, **2015**, 44, 362.

[11] X. Wu, J. Zhao, L. Wang, M. Han, M. Zhang, H. Wang, H. Huang, Y. Liu, Z. Kang, *Appl. Catal. B Environ.*, **2017**, 206, 501.

[12] V. Strauss, J.T. Margraf, K. Dirian, Z. Syrgiannis, M. Prato, C. Wessendorf, A. Hirsch, T. Clark, D.M. Guldi, *Angew. Chem*., **2015**, 54, 8292.

[13] R. Long, D. Casanova, W.-H. Fang, O.V. Prezhdo, *J. Am. Chem. Soc.*, **2017**, 137, 2619.

[14] B. Martindale, G.A. Hutton, C.A. Caputo, S. Prantl, R. Godin, J.R. Durrant, E. Reisner, *Angew. Chem.*, **2017**, 56, 6459.

[15] D. Choi, S. Ham, D.-J. Jang, *J. Environ. Chem. Eng.*, **2018**, 6, 1.

[16] H. Li, X. Zhang, D.R. MacFarlane, *Adv. Energy Mater.*, **2015**, 5, 1401077.

[17] Z. Wei, L. Rosa, K. Wang, M. Endo, S. Juodkazis, B. Ohtani, E. Kowalska, *Appl. Catal. B Environ.*, **2017**, 206, 393.

[18] K. Wenderich, G. Mul, Methods, *Chem. Rev*., **2016**, 116, 14587.

[19] J.F. Fernando, M.P. Shortell, C.J. Noble, J.R. Harmer, E.A. Jaatinen, E.R. Waclawik, *ACS Appl. Mater. Interfaces*, **2016**, 8, 14271.

[20] H. Tada, R. Negishi, S.-i. Naya, H. Kobayashi, *Angew. Chem*., **2017**, 56, 10347.

[21] J. Taing, M.H. Cheng, J.C. Hemminger, *ACS Nano*, **2011**, 5, 6325.

[22] K. Uma, N. Arjun, G.-T. Pan, T.C.-K. Yang, *Appl. Surf. Sci*., **2017**, 425, 377.

[23] G. González-Rubio, P. Díaz-Núñez, A. Rivera, A. Prada, G. Tardajos, J. González-Izquierdo, L. Bañares, P. Llombart, L.G. Macdowell, M.A. Palafox, *Science*, **2017**, 358, 640.

Chapter 4. Au-C/SiO_2 Nanocomposites with Enhanced Peroxidase-like Activity for Colorimetric and Fluorometric Detection of Hydrogen Peroxide †

† This is reproduced from Dayeon Choi, Sooho Ham, and Du-Jeon Jang, *Mater. Res. Bull.*, **2019,** ⓒ 2019 Elsevier Inc.

4.1 Abstract

Gold nanoparticles with an average diameter of 10 nm have been facilely prepared on Cdots/SiO_2 nanocomposites by a photodeposition method to fabricate Au-C/SiO_2 nanocomposites. Photodeposited gold nanoparticles have shown commendable peroxidase-like activity, so they can oxidize 3,3',5,5'-tetramethylbenzidine effectually in the presence of H_2O_2. The catalytic reaction followed the Michaelis-Menton kinetics; the obtained K_m value of Au-C/SiO_2 nanocomposites with H_2O_2 is 60 times smaller than that of HRP, indicating the strong affinity of Au-C/SiO_2 nanocomposites to H_2O_2. In addition, Au-C/SiO_2 nanocomposites can be used for the fluorometric detection of H_2O_2 because photodeposited gold nanoparticles act as light absorbers of Cdots. The fluorescence of Au-C/SiO_2 nanocomposites was highly enhanced as much as 18 times at 7.5 mM of H_2O_2. Taken together, H_2O_2 can be detected quantitatively via dual-signal modes, colorimetric and fluorometric methods, with Au-C/SiO_2 nanocomposites. Thus, it is suggested that our Au-C/SiO_2 nanocomposites have a wide range of applications in bio-detection, catalysis, and clinical diagnostics.

4.2 Introduction

Enzyme-based biosensing has attracted considerable attention due to its low cost, simplicity, and practicality. Horseradish peroxidase (HRP), a natural enzyme, has high catalytic efficiency and good substrate specificity. Nevertheless, the natural enzyme has some disadvantages. For example, the catalytic activity of natural enzymes is restricted to environmental changes, such as temperature, acidity, and inhibitors, which often lead to their denaturation and digestion.[1,2] Furthermore, preparation, purification, and storage are usually expensive and time-consuming. So, artificial enzymes as alternatives for natural enzymes receive much interest to overcome these drawbacks. Recently, artificial enzyme mimics, such as porphyrins, polymers, biomolecules, metal nanoparticles, metal oxides, and carbon-based materials, have been found to have peroxidase-like activity.[2-9] Because of high resistance to harsh reaction conditions, the artificial enzymes receive much interest. The concept of "nanozyme" was first proposed by Manea et al. to represent their thiol-coated gold clusters with ribonuclease-like activity.[7]

Gold nanoparticles have attracted great attention in diverse fields because of excellent biocompatibility and unique optoelectronic properties.[3-7,10] Also, they have been frequently used as light absorbers due to their high extinction coefficients.[11] Besides, their surface plasmon absorption can be facilely tuned to

overlap with the emission spectra of various common fluorophores by controlling their sizes, shapes, and compositions.

Carbon dots (Cdots) as interesting luminescence materials have been used for a variety of imaging, visualization and analysis.[12-15] Compared with other inorganic luminescence materials, Cdots have good chemical stability, solubility, and photostability, so they have wide potential for various applications. Above all, Cdots show outstanding electronic properties; Cdots act as electron donors and acceptors simultaneously.[16,17] Thus, we can use them as fluorophores for fluorescence-based detection systems.

Hydrogen peroxide (H_2O_2), as an important intermediate in environmental and biological processes or a messenger in cellular-signal transduction, plays as a significant role in living organisms.[18-20] Various methods have been utilized to determine the concentration of H_2O_2 efficiently. Among them, colorimetric detection is superior to other assays due to its convenience. Practically, the color change of substrates could be observed easily by the naked eye.[21-23] In addition, fluorescence-based sensing systems are also interesting owing to the benefits of excellent sensitivity, selectivity, simplicity, and rapid detection.[24] Nevertheless, detection signals can be interfered with various factors. Therefore, it is a serious task to find an efficient peroxidase-like system with dual-signal modes to detect H_2O_2 quantitatively.[25]

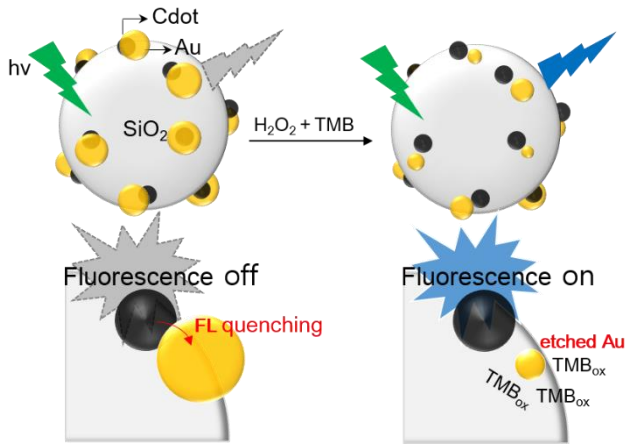

Figure 4-1 Schematic for the fluorosence-based detection of H_2O_2 by the TMB_{ox}-induced etching of gold nanoparticles

In this work, Au-C/SiO_2 nanocomposites have been prepared via a photodeposition method and employed to detect H_2O_2 via dual optical modes of absorption and emission. Gold nanoparticles deposited on C/SiO_2 nanocomposites can catalyze the oxidation reaction of a peroxidase substrate, 3,3',5,5'-tetramethylbenzidine (TMB), in the presence of H_2O_2 to develop a blue color product, which allows us to detect H_2O_2 colorimetrically.[26] Afterward, oxidized TMB (TMB_{ox}) can etch gold nanoparticles, changing the fluorescence intensity of Au-C/SiO_2 nanocomposites enormously. As gold nanoparticles can be used as light absorbers to quench the fluorescence (FL) of C/SiO_2 nanocomposites, TMB_{ox}-assisted gold etching provides the fluorometric detection of H_2O_2 (Figure 4-1). As-prepared Au-C/SiO_2 nanocomposites can be used as peroxidase mimics and light-

absorbers at the same time. Thus, H_2O_2 can be detected colorimetrically as well as fluorometrically with our Au-C/SiO_2 nanocomposites in the presence of TMB.

4.3 Material and methods

4.3.1 Materials

All chemicals were used as purchased: $HAuCl_4 \cdot 3H_2O$ (s, 99.9%), 28-30% NH_4OH(aq), 3-aminopropyl triethoxysilane (APTES, l, >98%), tetraethyl orthosilicate (TEOS, l, ≥99%), and citric acid (s, 99.5%) from Sigma-Aldrich; 3,3',5,5'-tetramethylbenzidine (TMB, s, 98%) from Alfa-Aesar; cetyl trimethyl ammonium bromide (CTAB, s), isopropyl alcohol (IPA, l), ethanol (l), and 30% hydrogen peroxide(aq) from Dajeong Chemicals. Water (>15 MΩ cm) purified using an ELGA PURELAB Option-S system was used throughout the experiments.

4.3.2 Preparation

C/SiO_2 nanocomposites. We have already reported the detailed synthetic methods of C/SiO_2 and Au-C/SiO_2 nanocomposites [16]. Briefly, silica nanospheres were synthesized via the sol-gel reaction of TEOS under base catalysis.

And the surfaces of SiO_2 nanospheres were modificated with APTES. Then, citric acid was added to the colloidal solution of APTES-modified SiO_2 nanospheres. The mixture was stirred for 10 min, transferred into a Teflon-lined stainless-steel autoclave, and maintained at 180 °C for 3 h. After the reaction, the product was centrifuged, rinsed three times with ethanol, and re-dispersed in 5.0 mL of ethanol.

Au-C/SiO_2 nanocomposites. 15 mL of water and 5.0 mL of ethanol, and 10 μL of the as-prepared colloidal solution of C/SiO_2 nanocomposites were mixed. The mixture was transferred into a quartz reactor, stirred for 10 min, placed 30 cm away from a xenon arc lamp with a focusing lens, and irradiated for a few seconds with stirring. The reaction was started by the addition of a specific amount of a $HAuCl_4$ stock solution and stopped by turning off the Xe lamp after 10 min; the concentration of the gold precursor in the final photodeposition reaction mixture was 6.35 μM and the light intensity at 250 nm was 327 mW. Then, the product was separated by centrifugation for 10 min at 12,000 rpm, washed with ethanol, and re-dispersed in 1.0 mL of ethanol.

4.3.3 Characterization

High-resolution TEM (HRTEM) images and energy-dispersive X-ray (EDX)

elemental mappings were obtained using a JEOL JEM-2100F microscope. Absorption spectra were measured using a Scinco S3100 UV-vis spectrophotometer and FL spectra were taken employing an Ocean Optics USB2000+ detector with excitation of 266 nm pulses having a duration time of 6 ns from a Q-switched Quantel Brilliant Nd:YAG laser.

4.3.4 Colorimetric detection of hydrogen peroxide

Peroxidase-like activity test of Au-C/SiO_2 nanocomposites. The peroxidase-like activity of Au-C/SiO_2 nanocomposites was investigated by monitoring the catalytic oxidization of TMB to TMB_{ox} in the presence of H_2O_2. 0.2 mL of 1.0 mM TMB(ethanol) and 0.2 mL of 0.2 mg mL^{-1} Au-C/SiO_2 nanocomposites(ethanol) were dispersed in 1.4 mL of an aqueous sodium acetate buffer (pH 4) solution. The mixture was incubated at 40 °C for 10 min, and then catalytic oxidation was started by adding 0.2 mL of 10 mM H_2O_2(aq). After 10 min, the absorbance of TMB_{ox} was recorded at 652 nm.

Optimization of experimental conditions. The peroxidase-like activity of Au-C/SiO_2 nanocomposites was optimized by varying pH values (3~6), temperatures (30~60 °C), nanocomposite catalyst amounts (0~20 μg), TMB concentrations (0~10 μM), and H_2O_2 concentrations (0~100 μM); only one parameter was varied

at a time while the other parameters were fixed. The color changes of reaction mixtures were observed by recording optical density changes at 652 nm.

4.3.5 Fluorescence-based detection of hydrogen peroxide

For the fluorescence-based detection of hydrogen peroxide, the TMB_{ox}-induced etching of gold nanoparticles has been performed at various concentrations of H_2O_2. On this occasion, CTAB was essential to promote the etching process. Thus, 0.1 mL of 10 mM CTAB(aq) was added to a prepared 2.0 mL TMB_{ox} solution with stirring to start the etching of gold nanoparticles. After 10 min, the product was separated by centrifugation at 9,000 rpm for 10 min, washed with ethanol, and re-dispersed in 1.0 mL of ethanol. Then, the fluorescence of etched Au-C/SiO_2 nanocomposites was recorded.

4.4 Results and discussion

4.4.1 Optical properties of Au-C/SiO_2 nanocomposites

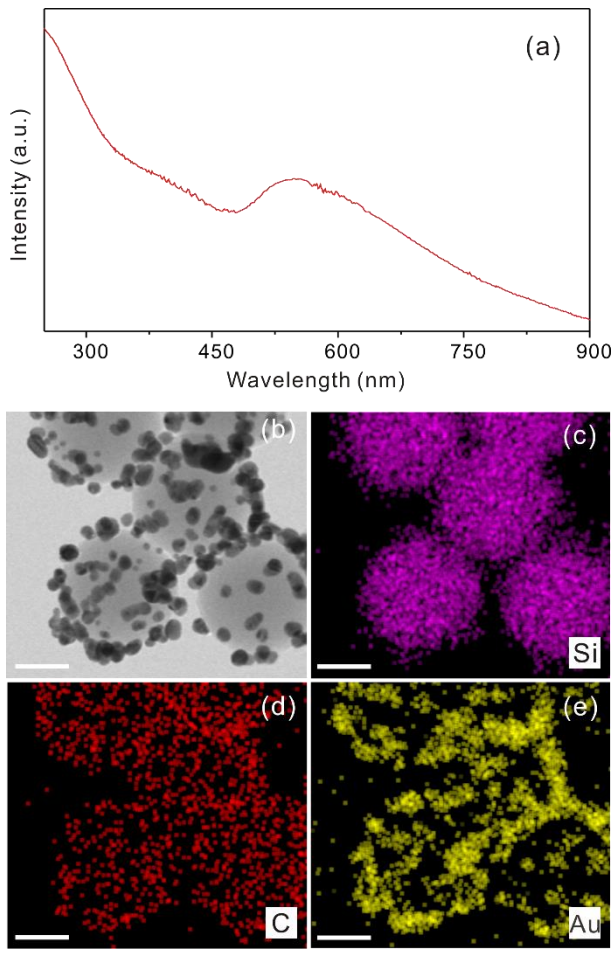

Figure 4-2 (a) An absorption spectrum and (b) an HRTEM image, and (c-e) EDX elemental maps of Au-C/SiO_2 nanocomposites. Each scale bar indicates 50 nm.

As shown in Figure 4-2a, the surface plasmon absorption of gold nanoparticles

centered at 530 nm was observed, indicating the existence of gold nanoparticles in Au-C/SiO_2 nanocomposites. The HRTEM image of Figure 4-2b reveals that gold nanoparticles having an average diameter of ~10 nm have been prepared on the surfaces of C/SiO_2 nanocomposites. The EDX mapping analysis in Figure 4-2c-e shows that Cdots are evenly distributed on SiO_2 nanospheres and that gold nanoparticles are photodeposited on the Cdots of C/SiO_2 nanocomposites, forming Au-C/SiO_2 nanocomposites.[16] By changing gold precursor concentrations, light intensities, and reaction times, we can control the sizes, contents, and coverages of gold nanoparticles adsorbed on C/SiO_2 nanocomposites.[16] Based on these results, we can propose that Cdots can be utilized as electron donors and nucleation sites in the photodeposition of gold nanoparticles.

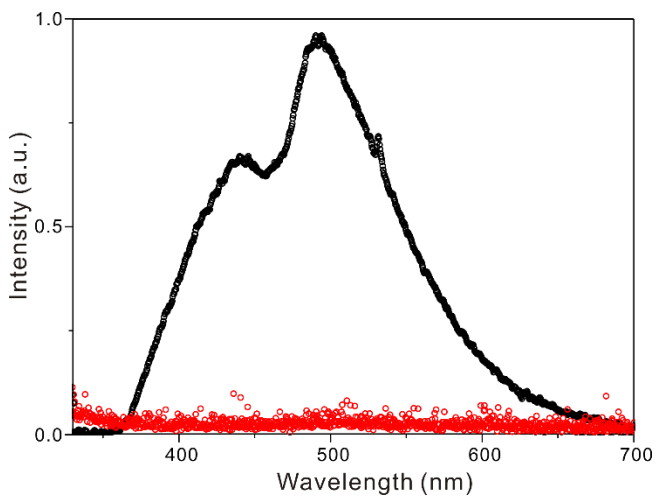

Figure 4-3 Emission spectra of (black) as-prepared C/SiO_2 and (red) Au-C/SiO_2 nanocomposites.

The emission spectra of Figure 4-3 are helpful to verify that gold nanoparticles exist on Cdots of Au-C/SiO_2 nanocomposites. Compared with the FL spectrum of C/SiO_2 nanocomposites, the spectrum of Au-C/SiO_2 nanocomposites is totally quenched. This suggests that photo-generated electrons from Cdots were almost completely transferred to gold nanoparticles. We can also explain this phenomenon by inner filter effect (IFE). IFE was previously considered as an error in fluorescence measurement,[11,24] but now it is recognized as an important non-radiative energy conversion process in spectroscopy techniques.[11,24] IFE results from the absorption of absorbers and the emission of fluorophores in a fluorescence-based detection system. The absorbers are critical in this system because their absorption ability and selectivity significantly affect whole sensing performances. For efficient detection performances with IFE, the spectral overlap between absorption and emission needs to be increased. Additionally, light-absorbers have to possess a high extinction coefficient. In our case, the absorption of gold nanoparticles is centered at ~530 nm (Figure 4-2a), the FL of C/SiO_2 nanocomposites appears around 400~600 nm (Figure 4-3), and the extinction coefficient of gold nanoparticles with an average diameter of ~13 nm is as large as 2.7×10^8 cm^{-1} M^{-1} at 520 nm.[11] Thus, the FL of C/SiO_2 nanocomposites can be drastically quenched by gold nanoparticles due to IFE. Considering the emission spectra of Figure 4-3, we can suggest that gold nanoparticles have been well

photodeposited on C/SiO_2 nanocomposites and that photodeposited gold nanoparticles function well as effective luminescence quenchers.

4.4.2 Peroxidase-like activity of Au-C/SiO_2 nanocomposites

The peroxidase-like activity of Au-C/SiO_2 nanocomposites was investigated by the catalytic oxidation of TMB to form TMB_{ox}. TMB is oxidized during the enzymatic degradation of H_2O_2 by peroxidase, so TMB is widely used as a peroxidase enzyme substrate. One electron detachment of TMB produces a radical cation that subsequently forms a charge transfer complex with a pristine TMB molecule.[26] This charge transfer complex absorbs at 652 nm. Therefore, the oxidized product (TMB_{ox}) has a blue color, which can be observed by the naked eye.

There is an obvious absorption band at 652 nm (Figure 4-4a) since TMB was oxidized to form TMB_{ox} by H_2O_2 in the presence of Au-C/SiO_2 nanocomposites, indicating that as-prepared Au-C/SiO_2 nanocomposites could catalyze the oxidation of TMB in the presence of H_2O_2. If either H_2O_2 (Figure 4-4b) or TMB (Figure 4-4c) was absent, TMB could not be oxidized as TMB_{ox} naturally. Some researchers have reported that Cdots themselves have peroxidase-like activity.[27] However, the comparison of Figure 4-4d with Figure 4-4e indicates that our C/SiO_2

nanocomposites have no catalytic activity at all. Therefore, we can suggest that gold nanoparticles deposited on C/SiO_2 nanocomposites have commendable peroxidase-like catalytic activity and that H_2O_2 can be detected colorimetrically with our Au-C/SiO_2 nanocomposites in the presence of TMB.

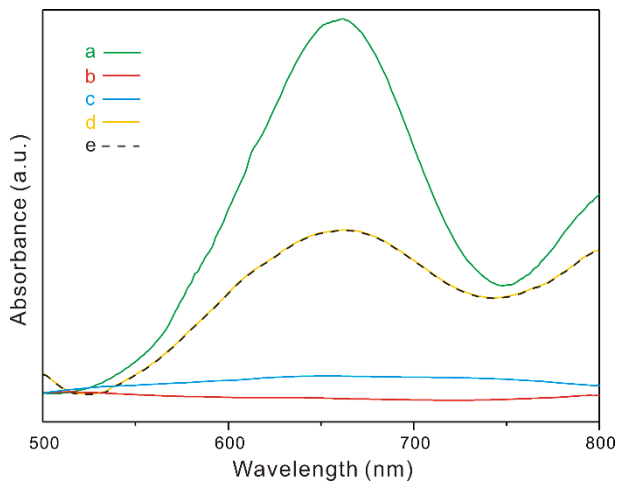

Figure 4-4 Absorption spectra of solutions containing (a) TMB + Au-C/SiO_2 + H_2O_2, (b) TMB + Au-C/SiO_2, (c) Au-C/SiO_2 + H_2O_2, (d) TMB + C/SiO_2 + H_2O_2, and (e) TMB + H_2O_2.

4.4.3 Colorimetric detection of hydrogen peroxide

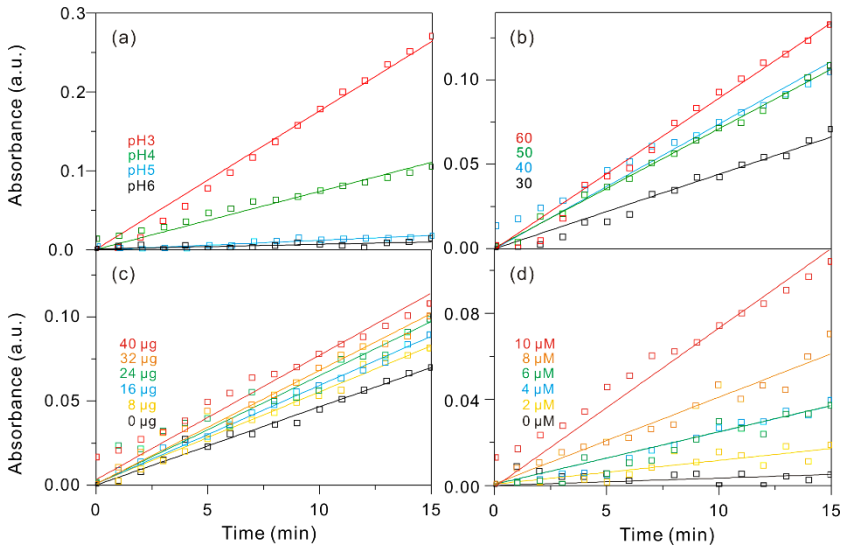

Figure 4-5 First-order kinetics, absorbance vs t, for the catalytic oxidation of TMB varied with (a) pH values, (b) temperatures, (c) catalyst amounts, and (d) TMB concentrations.

Like the catalytic activity of natural enzymes, that of Au-C/SiO_2 nanocomposites depends on various factors. So the activity was optimized by monitoring the absorbance of TMB_{ox} at 652 nm;[5-9] with variation of pH values, temperatures, catalyst amounts, and TMB concentrations, we have recorded the absorbance of TMB_{ox} at 652 nm as a function of time (Figure 4-5) and obtained rate constants for the peroxidase-like activity of Au-C/SiO_2 nanocomposites (Figure 4-6). The catalytic activity of Au-C/SiO_2 nanocomposites decreased with the increase of pH;

compared with the catalytic activity at pH 3, the activity became 1/2 at pH 4, 1/4 at pH 5, and 3% at pH 6. Like most other peroxidase-like enzymes, the optimum catalytic activity of Au-C/SiO_2 nanocomposites was strong in acidic solutions.[7-9] We have selected pH 4 for the normal condition because Au-C/SiO_2 nanocomposites was unstable at pH 3. Like other nanocatalysts, the catalytic activity increased with the increment of reaction temperatures.[9] We have also changed catalyst amounts from 0 μg to 40 μg and TMB concentrations from 0 μM to 10 μM. The catalytic activity has been found to increase with the increase of catalyst amounts and TMB concentrations.

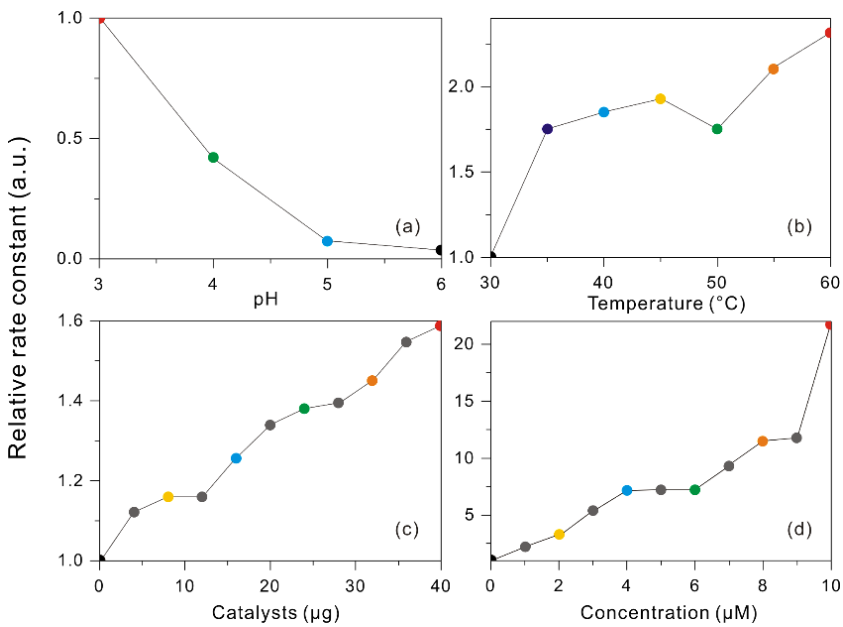

Figure 4-6 Relative rate constants for the peroxidase-like activity of Au-C/SiO_2 nanocomposites, depending on (a) pH values, (b) temperatures, (c) catalysts amounts, and (d) TMB concentrations.

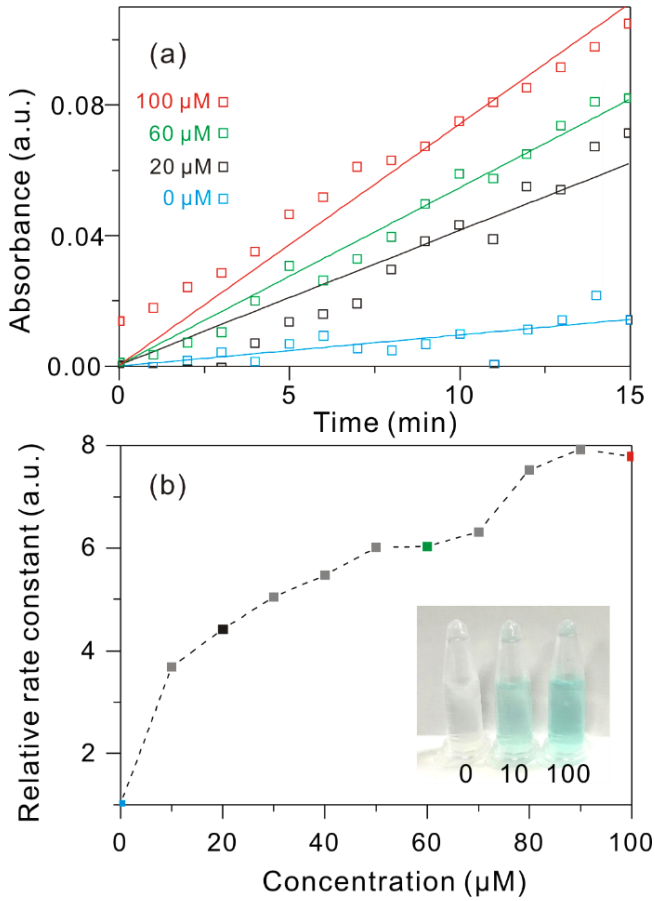

Figure 4-7 (a) First-order kinetics, absorbance vs t, for the catalytic oxidation of TMB under the indicated concentrations of H_2O_2; the rate constant, k, of the reaction has been obtained from the slope of the first-order kinetics. (b) Relative rate constants dependent on H_2O_2 concentrations. The photograph shows the representative colors of TMB_{ox} developed under the indicated concentrations in μM of H_2O_2.

Furthermore, we changed H_2O_2 concentrations from 0 to 100 μM (Figure 4-7). The catalytic activity increased gradually with the increase of H_2O_2 concentrations. In practical colorimetric detection conditions, the color change of TMB solution

should be identifiable by the naked eye. The inset of Figure 4-7 shows the digital images of TMB_{ox} solutions produced at three different concentrations of H_2O_2; note that we can well discern the blue color of a TMB_{ox} solution produced even at a relatively low 10 mM concentration of H_2O_2.

For the kinetic studies of the peroxidase-like activity of Au-C/SiO_2 nanocomposites, the apparent steady-state kinetic parameters (K_m and V_{max}) of the initial reaction following the typical Michaelis-Menton model were determined by changing the concentrations of H_2O_2 and TMB (Figure 4-8);[7-9] K_m is the Michaelis-Menton constant and V_{max} is the maximum reaction velocity. The obtained K_m and V_{max} values of Au-C/SiO_2 nanocomposites with H_2O_2 are 0.07 mM and 2.7 x 10^{-9} M s^{-1}, respectively, while the obtained K_m and V_{max} values of Au-C/SiO_2 nanocomposites with TMB are 7.1 mM and 7.2 x 10^{-7} M s^{-1}, respectively. Note that the K_m and V_{max} values of HRP with H_2O_2 are 3.7 mM and 8.7 x 10^{-8} M s^{-1}, respectively, and that those values of HRP with TMB are 0.4 mM and 1.0 x 10^{-7} M s^{-1}, respectively [8]. The K_m value of Au-C/SiO_2 nanocomposites with H_2O_2 is 60 times smaller than that of HRP, indicating the strong affinity of Au-C/SiO_2 nanocomposites to H_2O_2. Furthermore, this value is also smaller than the respective values of previously reported nanozymes.[7-9] However, the K_m value of Au-C/SiO_2 nanocomposites with TMB is larger than each value of HRP and other nanozymes.[7-9]

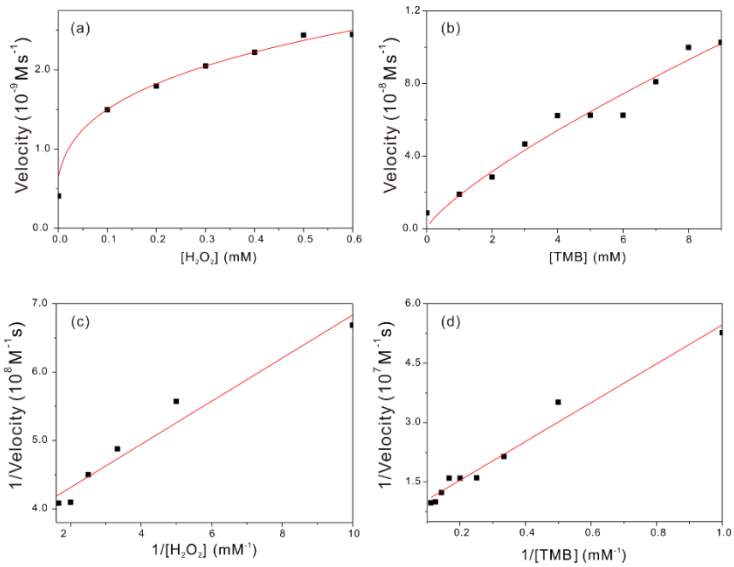

Figure 4-8 Steady-state kinetic analysis utilizing (a,b) the Michaelis-Menton model and (c,d) the Lineweaver-Burk double-reciprocal model for Au-C/SiO_2 nanocomposites with (a,c) H_2O_2 and (b,d) TMB.

4.4.4 Fluorometric detection of hydrogen peroxide

The fluorescence of Au-C/SiO_2 nanocomposites was monitored for the fluorometric detection of H_2O_2 based on the etching of gold nanoparticles deposited on C/SiO_2 nanocomposites (Figure 4-9a). As already mentioned with Figure 4-3, gold nanoparticles effectively quench the FL of C/SiO_2 nanocomposites. On this occasion, if gold nanoparticles are etched by H_2O_2, the FL of Cdots recovers effectually. Therefore, we can detect the concentration changes of hydrogen peroxide quantitatively by monitoring the FL intensity changes of Au-C/SiO_2

nanocomposites throughout the etching process. However, gold nanoparticles cannot be etched easily by H_2O_2 at normal conditions. Therefore, many researches have used TMB_{ox} to etch gold nanoparticles, so we have adopted TMB to etch gold nanoparticles.[21,22] As Au-C/SiO_2 nanocomposites have peroxidase-like activity, we can prepare TMB_{ox} ethanol solutions without using other enzymes such as HRP to etch gold nanoparticles. To start off the reaction, we added 0.1 mL of 10 mM CTAB(aq) because gold nanoparticles could not be etched easily by TMB_{ox}. The standard electrode potential of $AuBr_2^-$/Au (0.93 V vs NHE) is higher than that of TMB^{2+}/TMB (0.741 V vs NHE), blocking the oxidation of gold nanoparticles by TMB_{ox}. By adding CTAB, the reduction potential of $AuBr_2^-$/Au decreased substantially via forming $AuBr_2^-$-$(CTA)^{2+}$/Au (< 0.2 V vs NHE), helping the etching of gold nanoparticles.[21,22] As shown in Figure 4-10, the FL of Au-C/SiO_2 nanocomposites hardly recovered in the absence of CTAB whereas the FL of Au-C/SiO_2 nanocomposites was enhanced enormously in the presence of CTAB. Therefore, we started the reaction by adding CTAB into the reaction mixture.

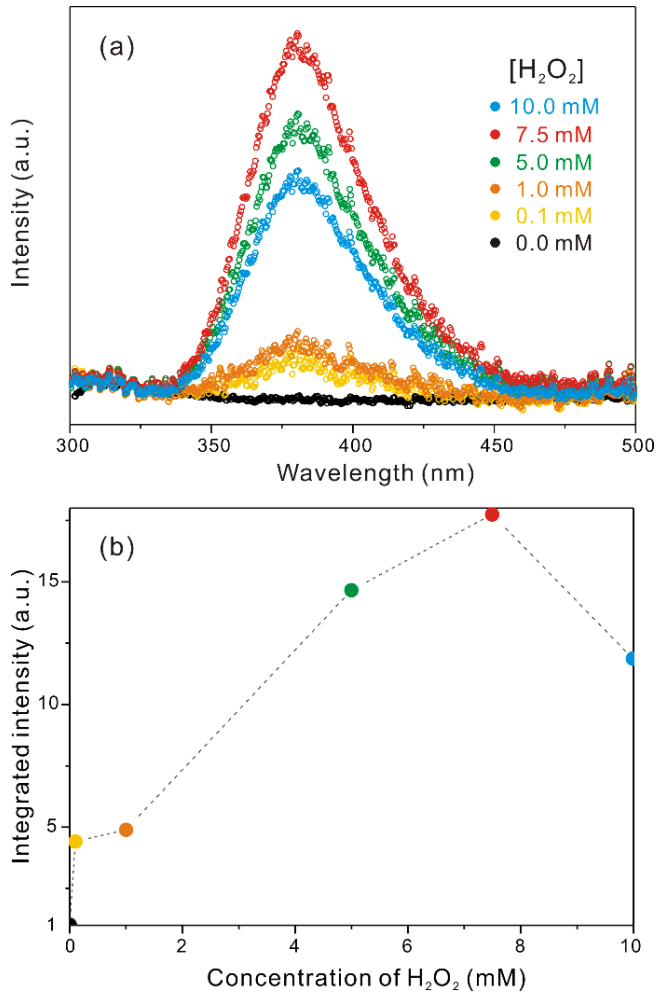

Figure 4-9 Influence of H_2O_2 concentrations on the fluorescence-based detection of H_2O_2 in the presence of TMB and Au-C/SiO_2 nanocomposites.

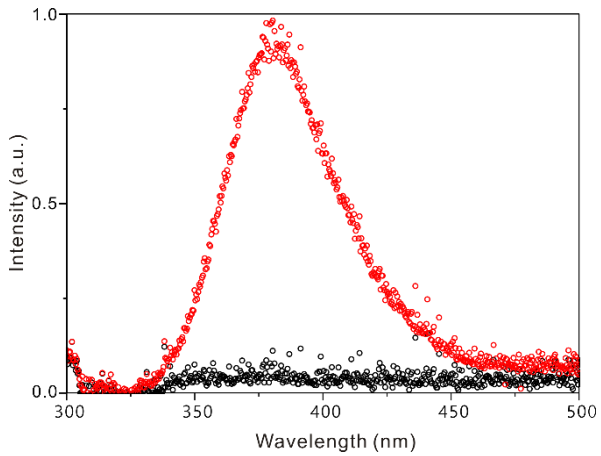

Figure 4-10 Emission spectra of Au-C/SiO_2 nanocomposites etched (red) with and (black) without CTAB.

Compared with the FL intensity of pristine Au-C/SiO_2 nanocomposites, that of Au-C/SiO_2 nanocomposites reacted with 1.0 mM of H_2O_2 increased five times (Figure 4-9b), suggesting that TMB_{ox} in the presence of CTAB can oxidize gold nanoparticles effectively. The FL intensity of Au-C/SiO_2 nanocomposites increased extensively with the concentration increase of H_2O_2 until it reached a maximum (18 times) at 7.5 mM of H_2O_2.

Based on Figs. 4-7 and 4-9, we can conclude that H_2O_2 can be detected effectually via dual-signal modes, colorimetric and fluorometric methods, with our Au-C/SiO_2 nanocomposites. Thus, we can suggest that our Au-C/SiO_2 nanocomposites have a wide range of potential applications in bio-detection, catalysis, and clinical diagnostics.

4.5 Conclusions

Gold nanoparticles having an average diameter of 10 nm have been facilely prepared on Cdots/SiO_2 nanocomposites by a photodeposition method to fabricate Au-C/SiO_2 nanocomposites. Photodeposited gold nanoparticles have shown commendable peroxidase-like activity, so they can oxidize the substrate of TMB effectually in the presence of H_2O_2. We can well discern the blue color of a TMB_{ox} solution produced at a relatively low 10 mM concentration of H_2O_2 by the naked eye. Therefore, Au-C/SiO_2 nanocomposites can be used for the colorimetric detection of H_2O_2. The catalytic reaction was found to follow the Michaelis-Menton kinetics; the obtained K_m value of Au-C/SiO_2 nanocomposites with H_2O_2 is 60 times smaller than that of HRP, indicating the strong affinity of Au-C/SiO_2 nanocomposites to H_2O_2. Note that, this value is also smaller than the respective reported values of nanozymes. In addition, Au-C/SiO_2 nanocomposites can be used for the fluorometric detection of H_2O_2 because photodeposited gold nanoparticles act as light absorbers of Cdots. The FL intensity was found to increase 18 times when the concentration of H_2O_2 was 7.5 mM. Taken together, H_2O_2 can be detected quantitatively via dual-signal modes, colorimetric and fluorometric methods, with Au-C/SiO_2 nanocomposites.

4.6 Acknowledgement

This work has been financially supported by the National Research Foundation of Korea (research grant: 2017-006153).

4.7 References

[1] L. He, Z.W. Jiang, W. Li, C.M. Li, C.Z. Huang, Y.F. Li, *ACS Appl. Mater. Interfaces*, **2018**, 10, 28868.

[2] Y. Jv, B. Li, R. Cao, *Chem. Commun.*, **2010**, 46, 8017.

[3] L. Hu, H. Liao, L. Feng, M. Wang, W. Fu, *Anal. Chem.*, **2018**, 90, 6247.

[4] W. Haider, A. Hayat, Y. Raza, A.A. Chaudhry, J.L. Marty, *RSC Adv.*, **2015**, 5, 24853.

[5] X. Jiang, C. Sun, Y. Guo, G. Nie, L. Xu, *Biosens.Bioelectron.*, **2015**, 64, 165.

[6] J. Shah, R. Purohit, R. Singh, A.S. Karakoti, S. Singh, *J. Colloid Interface Sci.*, **2015**, 456, 100.

[7] Y. Ding, B. Yang, H. Liu, Z. Liu, X. Zhang, X. Zheng, Q. Liu, *Sens. Actuators B Chem.*, **2018**, 259, 775.

[8] Y. Gao, K. Wu, H. Li, W. Chen, M. Fu, K. Yue, X. Zhu, Q. Liu, *Sens. Actuators B Chem.*, **2018**, 273, 1635.

[9] N. Lu, M. Zhang, L. Ding, J. Zheng, C. Zeng, Y. Wen, G. Liu, A. Aldalbahi, J. Shi, S. Song, X. Zuo, L. Wang, *Nanoscale*, **2017**, 9, 4508.

[10] T.-H. Park, D.-J. Jang, *Nanoscale*, **2018**, 10, 20108..

[11] S. Chen, Y.-L. Yu, J.-H. Wang, *Anal. Chim. Acta*, **2018**, 999, 13.

[12] W. Liu, F. Ding, Y. Wang, L. Mao, R. Liang, P. Zou, X. Wang, Q. Zhao, H. Rao, *Sens. Actuators B Chem*., **2018**, 265, 310.

[13] J. Zhu, X. Bai, Y. Zhai, X. Chen, Y. Zhu, G. Pan, H. Zhang, B. Dong, H. Song, *J. Mater. Chem. C*, **2017**, 5, 11416.

[14] I.Y. Goryacheva, A.V. Sapelkin, G.B. Sukhorukov, *Trends Anal. Chem*., **2017**, 90, 27.

[15] C. Yu, X. Li, F. Zeng, F. Zheng, S. Wu, *Chem. Commun*., **2013**, 49, 403.

[16] D. Choi, D.-J. Jang, *New J. Chem*., **2018**, 42, 14717.

[17] D. Choi, S. Ham, D.-J. Jang, *J. Environ. Chem. Eng.*,**2018**, 6, 1.

[18] L. Sun, Y. Ding, Y. Jiang, Q. Liu, *Sens. Actuators B Chem*., **2017**, 239, 848.

[19] P. Wang, K. Wang, Y. Gu, *Sens. Actuators B Chem*., **2016**, 228, 174.

[20] S.K. Maji, S. Sreejith, A.K. Mandal, X. Ma, Y. Zhao, *ACS Appl. Mater. Interfaces*, **2014**, 6, 13648.

[21] Y. Lin, M. Zhao, Y. Guo, X. Ma, F. Luo, L. Guo, B. Qiu, G. Chen, Z. Lin, *Sci. Rep*., **2016**, 6.

[22] L. Guo, S. Xu, X. Ma, B. Qiu, Z. Lin, G. Chen, *Sci. Rep.*, **2016**, 6, 32755.

[23] Y. Jiang, H. Zhao, Y. Lin, N. Zhu, Y. Ma, L. Mao, *Angew. Chem*., **2010**, 122, 4910.

[24] Y. Liu, H. Li, B. Guo, L. Wei, B. Chen, Y. Zhang, *Biosens.Bioelectron*., **2017**, 91, 734.

[25] Q. Zhao, S. Chen, H. Huang, L. Zhang, L. Wang, F. Liu, J. Chen, Y. Zeng, P.K. Chu, *Analyst*, **2014**, 139, 1498.

[26] P.D. Josephy, T. Eling, R.P. Mason, *J. Biol. Chem*., **1982**, 257, 3669.

[27] Y. Song, K. Qu, C. Zhao, J. Ren, X. Qu, *Adv. Mater*., **2010**, 22, 2206.

Chapter 5. Facile Fabrication of CuO/Cu_2O Composites with High Catalytic Performances †

† This is reproduced from Dayeon Choi and Du-Jeon Jang, *New J. Chem.*, **2017,** *41*, 2964-2972.

5.1 Abstract

Diverse morphologies of CuO/Cu_2O composites having good catalytic properties for the reduction of 4-nitrophenol in the presence of $NaBH_4$ have been controlled facilely by adjusting the concentrations of NaOH during the wet etching of Cu_2O cubes. The catalytic activity of CuO/Cu_2O composites is found to depend highly on their morphologies; in particular, CuO/Cu_2O composites prepared at 0.3 M of NaOH(aq) have shown the strongest catalytic performances. Regarding to the highest catalytic activity of the composites with cavities surrounded by CuO flakes, confinement effect is considered to expedite electron transfer from BH_4^- to the dye molecule enormously by reducing the activation energy largely; the energetically favorable formation of the activated complex at the inner walls of a CuO box lowers the energy barrier substantially. In brief, CuO/Cu_2O composites having high catalytic activity have been prepared facilely via a controlled oxidation process of Cu_2O cubes, and they may be applied to treat wastewater in an inexpensive way without employing commonly used noble-metal catalysts.

5.2 Introduction

The industrial society must treat wastewater containing diverse contaminants from toxic organics such as phenol, benzene, other aromatics, and amines to inorganics like sulfite, mercaptans, cyanide, and heavy metals. Therefore, the decomposition of organic contaminants in wastewater is a powerful solution to water pollution treatment. For the purpose of wastewater treatment, nanoscale materials like semiconductors and metals[1-8] have been reported as excellent catalysts due to their enlarged surface area,[9] which obviously correlates with an increase in the number of active sites and exposed surface atoms. Although catalytic performances of noble-metal catalysts have already been reported,[3-7] due to the high cost and limited availability of noble-metal catalysts, there is a strong need to develop suitable catalysts that are economical, easily available, and nontoxic. Moreover, the high surface energy of nanostructures makes them unstable in solutions, resulting in aggregation followed by the loss of catalytic activity. Thus, to overcome these problems, capping agents or polymer surfactants are often used to stabilize catalysts. However, if interaction forces between the stabilizers and nanostructure are too strong, the catalytic activity will be lessen. Therefore, as an alternative method to overcome these drawbacks, numerous researchers have strived for the introduction of solid supports such as polymers,

carbon materials, and semiconductors.[10-13] Among those semiconductor materials, copper oxides are attractive materials for support materials. They can be synthesized with various morphologies easily[14-18] and used for large-scale applications due to non-toxicity, abundance, and cheapness. Thus, copper oxides have often been used as templates for the synthesis of various metal oxides, metal sulfides, and metal particles.[16-18] Recently, it has been reported that oxides of first-row transition metals such as CuO, Co_3O_4, Fe_2O_3, and NiO have catalytic activity as well in the conversion of 4-nitrophenol to 4-aminophenol;[19] so, metal oxides with high reactivity may become promising cost-effective catalysts.[13,19,20]

Nitrogen-containing phenol derivatives generated from the production of toxic substances are some of the most stubborn pollutants in industrialized wastewater.[19-21] The United State Environmental Protection Agency (EPA) has regarded nitrophenols and their derivatives as priority pollutants due to their toxicity and hazard. Among nitrogen-containing phenol derivatives, 4-nitrophenol (4-NP) is a popular one of the frequently occurring by-products that are harmful to the environment. By the way, 4-aminophenol (4-AP) is an important intermediate in the manufacturing of analgesic drugs and can also be used in photographic developers, corrosion inhibitors, anticorrosion lubricant additives, and hair-dyeing agents.[22] Luckily, 4-NP could be a precursor to 4-AP. However, nitro-compounds cannot be easily reduced with electron donors.[19-22] A variety of reducing reagents

such as sodium sulfide (Na_2S), sodium borohydride ($NaBH_4$), hydrazine monohydrate ($N_2H_4 \cdot H_2O$), and hydrogen can reduce nitro-aromatics. Among them, $N_2H_4 \cdot H_2O$ is a low-cost reducing agent but it is toxic and hazardous because it is poisonous to nerve tissues, livers, lungs, and kidneys.[22] Thus, $NaBH_4$ is the most widespread and common reducing agent for the reduction of nitro groups. The catalytic reduction of 4-NP via a metal catalyst in the presence of borohydride (BH_4^-) ions has become a typical reaction. The reduction of 4-NP by BH_4^- in the absence of any catalysts is thermodynamically feasible, but it is not achievable kinetically because of a high kinetic barrier between the repelling negative ions of 4-nitrophenolate and BH_4^-. Therefore, it is necessary to develop catalysts accelerating the reaction. If so, we could handle the environment problem and produce the beneficial product of 4-AP simultaneously.[22]

In this work, we have synthesized CuO/Cu_2O composites with various structures facilely via the wet-etching of pristine Cu_2O cubes at different concentrations of NaOH (Figure 1). Etching at 0.1 and 0.2 M of NaOH(aq) has produced CuO/Cu_2O composites where Cu_2O cubes are surrounded incompletely by CuO flakes. CuO/Cu_2O composites prepared at 0.3 M of NaOH(aq) have a box of CuO flakes, which contains a hollow interior as well as a CuO cube. However, the box-like CuO structures have been collapsed under a harsh alkaline condition of 0.4 M NaOH(aq). Prepared Cu_2O cubes and CuO/Cu_2O composites have been used as catalysts to

reduce 4-NP in the presence of $NaBH_4$. The catalytic activity of CuO/Cu_2O composites is found to depend highly on their morphologies, suggesting that through this relatively simple and easy oxidation process, we can control the morphologies of CuO/Cu_2O composites facilely to have good catalytic activity for 4-NP reduction; wastewater can be treated with inexpensive catalysts of prepared CuO/Cu_2O composites.

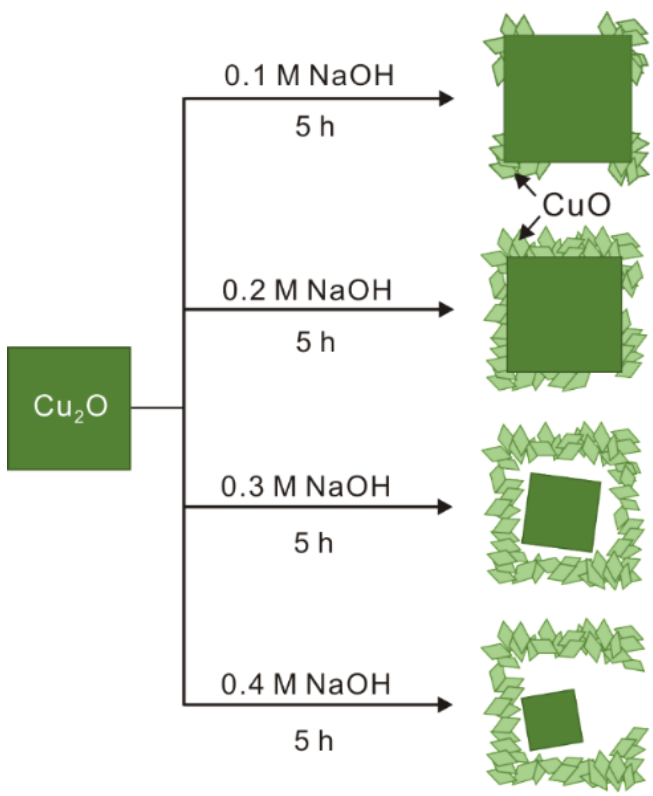

Figure 5-1 Schematic for the synthesis of CuO/Cu_2O composites via the simple top-down wet etching of Cu_2O cubes.

5.3 Experimental method

5.3.1 Materials

Chemicals were used as received: polyvinylpyrrolidone (PVP, s, Mw ~29,000), $CuCl_2 \cdot 2H_2O$ (s, 98%), L-ascorbic acid (s, 99%), $NaBH_4$ (s, 99%), 4-nitrophenol (4-NP, s) from Sigma-Aldrich; NaOH (s, 97%) from Dajeong Chemicals. Ultrapure deionized water (>15 MΩ cm) from an Elga PURELAB Option-S system was used throughout the experiments.

5.3.2 Preparation

Cu_2O cubes. Cu_2O cubes were synthesized by a wet-chemical solution method according to previous works.[23] The entire processes were carried out in a water bath at 55 °C with constant stirring. 110 mg of polyvinylpyrrolidone was added into 100 mL of 0.1 M $CuCl_2$(aq) and stirred for 1 h. Then, 10.0 mL of 2.0 M NaOH(aq) was added to the above mixed solution drop-by-drop by using a pipette. After 30 min, 10.0 mL of 0.6 M L-ascorbic acid(aq) was added slowly in the same manner. The mixed dark brown solution turned gradually into a turbid red solution,

which was then allowed to react for 3 h. The autoclave was naturally cooled down to room temperature and centrifuged at 7,000 rpm for 5 min. The collected products were washed several times with distilled water and ethanol and dried at 60 °C for 5 h.

CuO/Cu_2O composites. An aqueous solution of 40 mL containing 40 mg of prepared Cu_2O cubes and a specific concentration of NaOH was stirred for 30 min at room temperature. Then, the above solution was transferred into a Teflon-lined stainless-steel autoclave of 50 mL capacity and placed in an oven at 150 °C for 5 h. Hereafter, the product prepared at an x M concentration of NaOH will be designated as CuO/Cu_2O(x M) composites.

5.3.3 Characterization

While transmission electron microscopy (TEM) images were measured using a Hitachi H-7600 microscope operating at 100 kV, field-emission scanning electron microscopy (FE-SEM) images were obtained with a ZEISS MERLIN Compact microscope. High-resolution transmission electron microscopy (HRTEM) images, fast Fourier-transform (FFT) patterns, and selected-area diffraction (SAED) patterns were acquired using a FEI Tecnai F20 transmission electron microscope

operating at 200 kV, and X-ray diffraction (XRD) patterns were collected with a Bruker New D8 advanced diffractometer using Cu-K_α radiation. X-ray photoelectron spectroscopy (XPS) spectra were obtained with a KRATOS AXIS-HSI spectrometer using Al-K_α and the measured binding energies were calibrated with the C 1s peak at 284.5 eV of contaminated carbon. Absorption spectra were measured with a Scinco S3100 UV-vis spectrophotometer.

5.4.4 Catalytic experiments

For the evaluation of the catalytic properties of CuO/Cu_2O composites, the reduction reaction of 4-NP in the presence of $NaBH_4$ was investigated. 0.368 mL of an aqueous 0.10 $g\,L^{-1}$ catalyst colloid and 0.160 mL of 1.0 mM 4-NP(aq) were added to 1.452 mL of water contained in a cuvette. Subsequently, 20 µL of freshly prepared 0.2 M $NaBH_4$(aq) was added to the above solution, resulting in color change from light yellow to bright yellow immediately. Thus, the concentrations of $NaBH_4$, 4-NP, and a catalyst in 2.0 mL of the final catalytic reaction mixture were 2.0 mM, 80 µM, and 18 $mg\,L^{-1}$. The absorption changes of 4-NP after addition of $NaBH_4$ were monitored at scheduled intervals using a temperature-controllable spectrometer.

5.4 Results and discussion

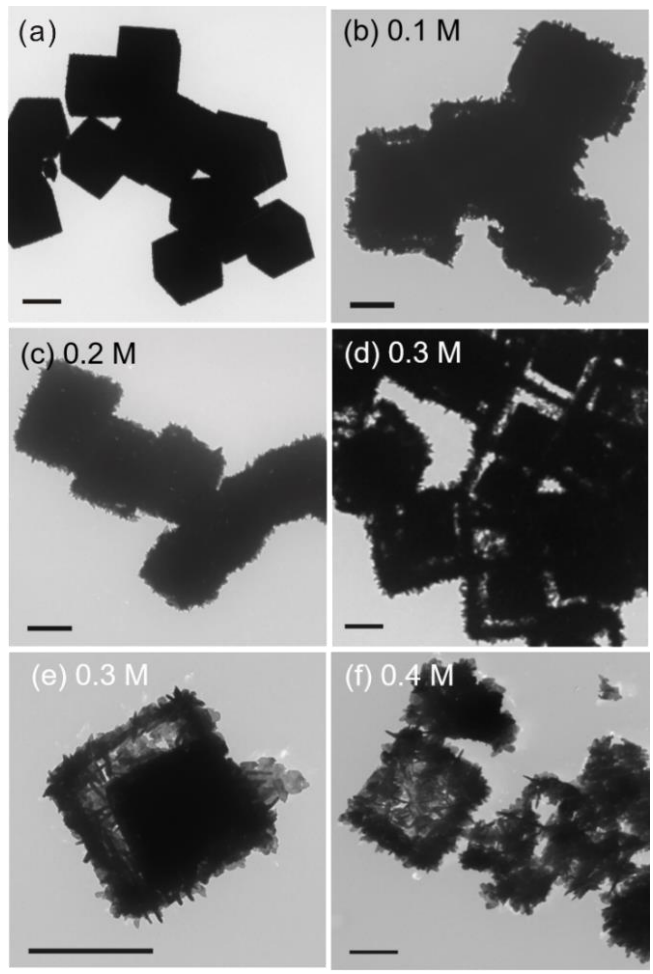

Figure 5-2 TEM images of pristine Cu_2O cubes (a) and CuO/Cu_2O composites prepared at respectively indicated concentrations of NaOH(aq) (b-f). Each scale bar indicates 1 μm.

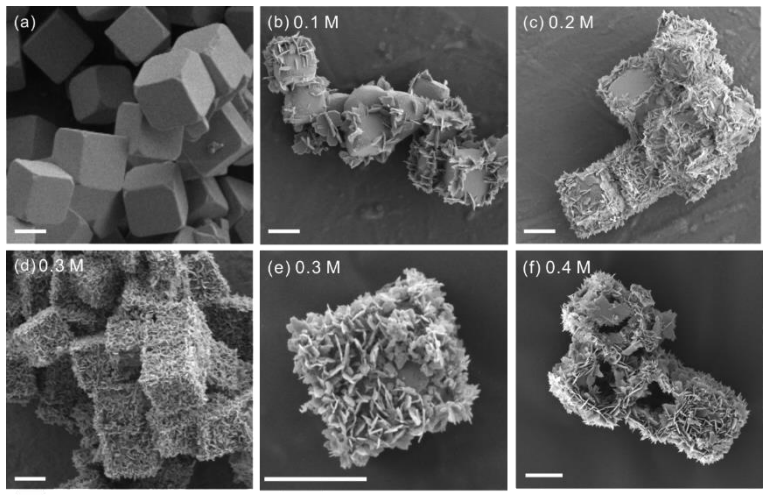

Figure 5-3 FE-SEM images of pristine Cu_2O cubes (a), and CuO/Cu_2O composites prepared at respectively indicated concentrations of NaOH(aq) (b-f). Each scale bar indicates 1 μm.

By controlling the concentrations of NaOH(aq) for the wet etching of Cu_2O cubes, the morphologies of CuO/Cu_2O composites have been controlled. As shown in Figure 5-2, well-defined pristine Cu_2O cubes having smooth surfaces were synthesized and the average edge length of the cubes is about 1.2 μm. As pristine Cu_2O cubes were hydrothermally treated with NaOH(aq), the Cu_2O cubes were transformed into CuO/Cu_2O composites with various morphologies depending on the concentrations of NaOH(aq). FE-SEM images of Figure 5-3 are also helpful to identify the detailed three-dimensional structures of pristine Cu_2O cubes and CuO/Cu_2O composites. In the presence of 0.1 M NaOH(aq), pristine Cu_2O cubes were oxidized to dissolve into the aqueous solution, producing CuO/Cu_2O(0.1 M)

composites where CuO flakes were formed at the corners of Cu_2O cubes as drawn in Figure 5-1. For CuO/Cu_2O(0.2 M) composites, additionally produced CuO flakes cover from the edges to the faces of Cu_2O cubes. For CuO/Cu_2O(0.3 M) composites, each hierarchical CuO box consisting of numerous CuO flakes encloses a Cu_2O cube. The contrast between a CuO box and a smaller Cu_2O cube clearly indicates that each CuO/Cu_2O composite contains a hollow interior as well as a Cu_2O cube. Until the concentration of NaOH(aq) reaches 0.3 M, the outer sizes of CuO/Cu_2O composites are almost the same as the initial sizes of pristine Cu_2O cubes. However, the box-like CuO structures have been collapsed under a harsh alkaline condition of 0.4 M NaOH(aq). According to a previous report by Song et al,[24] this oxidation etching of Cu_2O cubes is consistent with the dissolution-precipitation process and the unique structures may be produced by a synergetic effect of oxidation etching and the Kirkendall effect. By addition of NaOH(aq), the surface of a Cu_2O cube, starting from the edge to the side, is firstly oxidized into copper(II) hydroxide. In strong alkaline conditions, tetrahydroxocuparate(II) anions are produced and then thermodynamically stable CuO precipitates gradually on the inner walls of a hollow CuO structure. Simultaneously, the relatively different diffusion velocities of Cu^{2+} and Cu^{+} at the hydrothermal reaction conditions let CuO/Cu_2O composites have unique structures. The reaction mechanisms of Cu_2O cubes involved in the formation of CuO flakes were

previously proposed as the following equations:[23]

$$2\,Cu_2O(s) + O_2(g) + 4\,H_2O(l) \rightarrow 4\,Cu(OH)_2(s) \quad (1)$$

$$Cu(OH)_2(s) + 2\,OH^-(aq) \rightarrow [Cu(OH)_4]^{2-}(aq) \quad (2)$$

$$[Cu(OH)_4]^{2-}(aq) \rightleftharpoons CuO(s) + 2\,OH^-(aq) + H_2O(l) \quad (3)$$

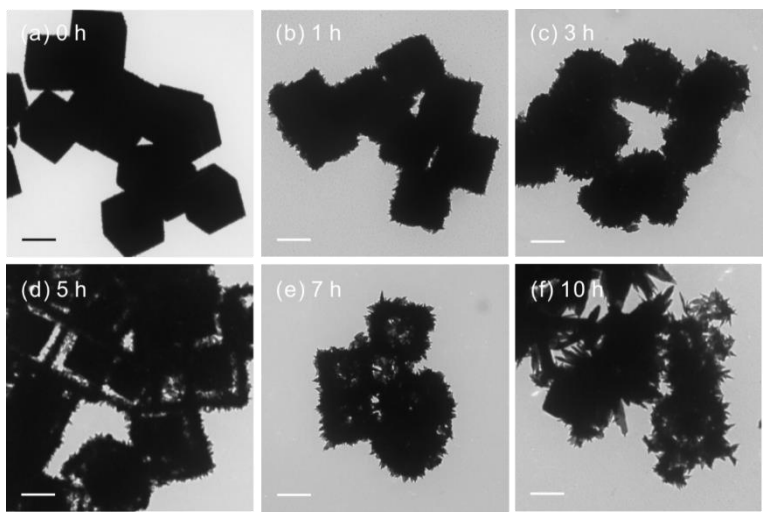

Figure 5-4 TEM images of CuO/Cu_2O(0.3 M) composites prepared via the wet etching of Cu_2O cubes for indicated durations.

On the basis of the above equations, upon further increase of the OH^- concentration to 0.4 M, square planar $Cu(OH)_4^{2-}$ ions become highly stable, slowing down the precipitation rate of CuO(s) through the reverse reaction process of eqn (3). Consequently, such a slow formation of CuO(s) provides enough time for soluble intermediates to diffuse out, resulting in the severe destruction of the

outer structure.[24] On the basis of the literature[24] and our results, the amount of added OH^- ions has been found to have a strong influence on the final structures of CuO/Cu_2O composites. To find out the formation mechanism of CuO/Cu_2O composites, the time-dependent etching process of pristine Cu_2O cubes was also monitored at a 0.3 M concentration of NaOH(aq) (Figure 5-4). At the initial stage, the surfaces of Cu_2O cubes were surrounded by newly formed CuO flakes, which were growing larger until 3 h. After etching for 5 h, a Cu_2O cube became smaller to be enclosed with a cavity in a box of CuO flakes. However, further oxidation for 7 - 10 h crumbled the box structures of CuO flakes, forming featureless CuO/Cu_2O composites. Overall, Figs. 5-2, 5-3, and 5-4 have indicated that the morphologies of CuO/Cu_2O composites have been controlled faciley by adjusting the concentrations of NaOH(aq) during the wet etching of Cu_2O cubes.

Detailed structural analysis has been performed by measuring a HRTEM image of a CuO/Cu_2O(0.3 M) composite (Figure 5-5a); a Cu_2O cube of a reduced size is enclosed in a box of CuO flakes. Thus, the CuO box also contains a hollow interior, which is essential for the high catalytic activity of CuO/Cu_2O(0.3 M) composite (see below). The inner Cu_2O part of a CuO/Cu_2O(0.3 M) composite is too thick to be monitored for lattice fringes. Thus, only the squared part of CuO flakes have been examined closely. Figure 5-5b shows the average d-spacing values of 0.253 nm, which agree very well with the standard spacing of 0.253 nm between the (002)

planes of the CuO lattice (PDF Card No. 00-045-0937). The FFT pattern of CuO flakes (Figure 5-5c) shows the squared spot, which can be indexed to the (002) planes of the CuO lattice. The (002) diffraction is particularly strong in the FFT pattern, indicating that the nanocrystals of CuO flakes have been preferentially precipitated along the [001] direction. The SAED pattern (Figure 5-5d) of a CuO/Cu_2O(0.3 M) composite displays that CuO flakes have the diffraction rings of the (002) and (111) planes, suggesting that CuO flakes correspond well to the polycrystalline phases of CuO. Thus, based on our structural analysis (Figure 5-5), the chemical composition of the newly produced flakes can be identified as CuO.

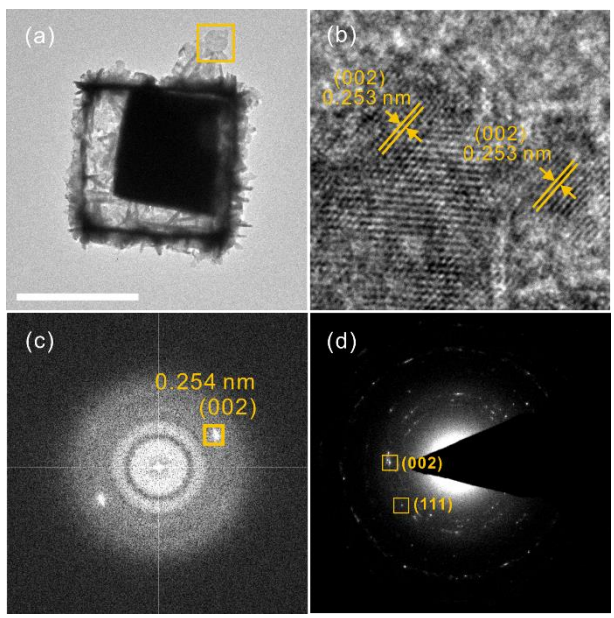

Figure 5-5 HRTEM image (a), enlarged HRTEM image (b), FFT pattern (c), and SAED pattern (d) of a CuO/Cu_2O(0.3 M) composite.

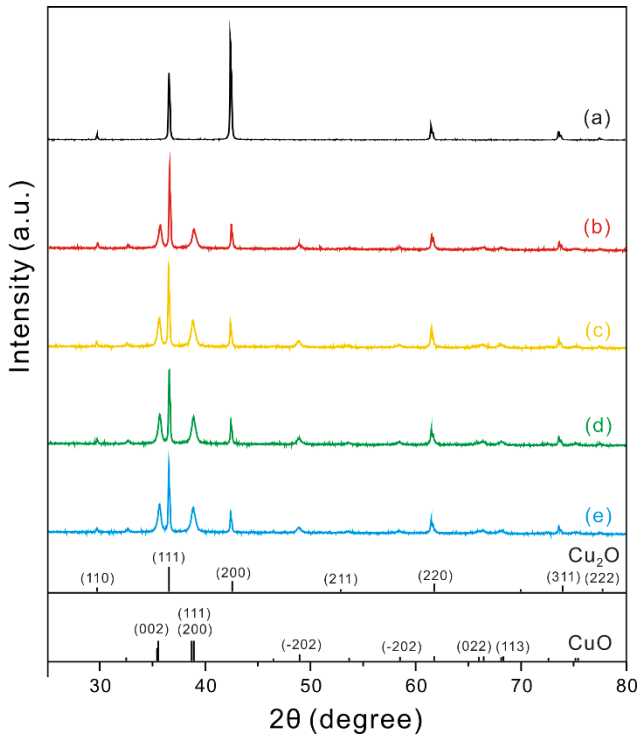

Figure 5-6 XRD patterns of pristine Cu_2O cubes (a) and CuO/Cu_2O(0.1 M) (b), CuO/Cu_2O(0.2 M) (c), CuO/Cu_2O(0.3 M) (d), and CuO/Cu_2O(0.4 M) (e) composites. The standard diffraction patterns of cubic Cu_2O and monoclinic CuO are also shown for comparison.

XRD patterns have been measured to understand the crystal structures of pristine Cu_2O cubes and CuO/Cu_2O composites (Figure 5-6). Pristine Cu_2O cubes have the pure cubic crystal phase (PDF Card No. 00-005-0667), and very sharp diffraction peaks indicate that pristine Cu_2O cubes have a good crystallographic structure. Unlike the reference Cu_2O cubic crystal phase, the intensity of (200) planes is much higher than that of (111) planes, indicating that (200) planes have been largely

exposed in our pristine Cu_2O cubes. Meanwhile, CuO/Cu_2O composites contain mixed phases of cubic Cu_2O and monoclinic CuO (PDF Card No. 00-045-0937), revealing that crystalline Cu_2O and CuO lattices are present simultaneously in our prepared CuO/Cu_2O composites. The XRD patterns of CuO/Cu_2O composites do not show any peaks arising from impurities such as $Cu(OH)_2$, implying that pristine Cu_2O cubes have been converted to CuO/Cu_2O composites successfully via a wet-etching process Whereas the intensity ratio of the $Cu_2O_{(111)}$ peak to the $Cu_2O_{(200)}$ peak is 0.7 for pristine Cu_2O, it is about 3.4 for CuO/Cu_2O composites; note the intensity ratio is 2.7 for the reference cubic Cu_2O. As a result, we can deduce that the highly exposed (200) planes of pristine Cu_2O cubes have been oxidized firstly to form CuO, increasing the intensity fraction of the (111) planes extensively during the wet etching of Cu_2O cubes.

Table 5-1 Crystallite sizes (D) and plane distances (d) in the units of nm, calculated from XRD patterns

Catalyst	D of Cu_2O	D of CuO	$d_{(111)}$ of Cu_2O	$d_{(002)}$ of CuO
reference Cu_2O			0.247	
reference CuO				0.253
pristine Cu_2O	66.1		0.246	
CuO/Cu_2O(0.1 M)	68.2	27.9	0.246	0.250
CuO/Cu_2O(0.2 M)	70.0	28.1	0.246	0.252
CuO/Cu_2O(0.3 M)	70.3	27.7	0.246	0.252
CuO/Cu_2O(0.4 M)	72.1	28.0	0.246	0.252

Using the Scherrer's equation[1] and assuming that peak broadening arises entirely from size effects, we have calculated the respective average crystallite sizes of Cu_2O and CuO in CuO/Cu_2O composites (Table 5-1); the broadening of the $Cu_2O_{(111)}$ peak at 2θ of 36.4° has revealed average crystallite sizes of ~70 nm while the broadening of the $CuO_{(002)}$ peak at 2θ of 35.5° has been calculated to yield average crystallite sizes of ~28 nm. As expected naturally, crystallite sizes of CuO flakes are much smaller than those of Cu_2O cubes. By the way, crystallite sizes of both Cu_2O cubes and CuO flakes are almost invariant regardless of NaOH concentrations, suggesting that Cu_2O and CuO do not have a heterojunction structure in CuO/Cu_2O composites.

Average distances between the adjacent (111) planes of Cu_2O and the (002) planes of CuO obtained using the Bragg's law have been found to be invariant regardless of CuO/Cu_2O composites (Table 5-1). This indicates that the lattice structures of both Cu_2O and CuO crystals remain the same regardless of NaOH concentrations during the wet etching of Cu_2O cubes. This result also suggests that Cu_2O and CuO do not have a heterojunction or alloy structures. Thus, both Cu_2O cubes and CuO flakes have their own respective properties in CuO/Cu_2O composites.

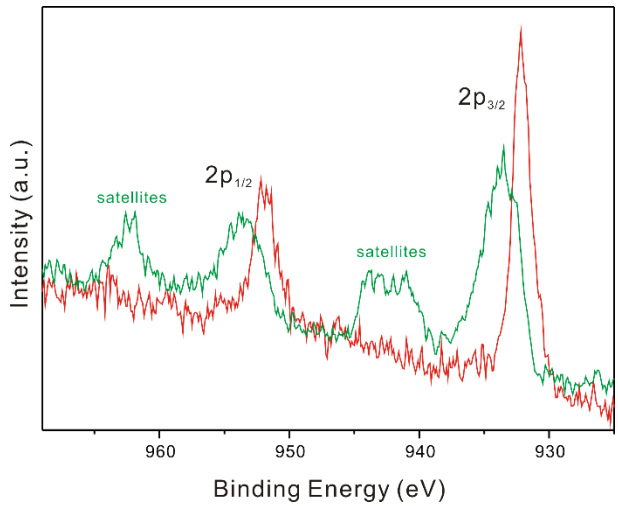

Figure 5-7 Cu 2p XPS curves of pristine Cu_2O cubes (red) and CuO/Cu_2O(0.3 M) composites (green).

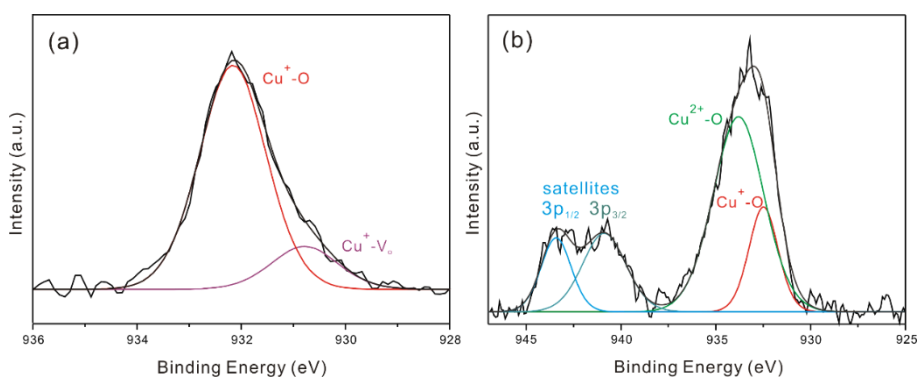

Figure 5-8 Deconvoluted Cu $2p_{3/2}$ XPS curves of pristine Cu_2O cubes (a), and CuO/Cu_2O(0.3 M) composites

To further ascertain the composition of CuO/Cu_2O composites, the binding energies (E_B) of Cu have been obtained by measuring XPS curves (Figure 5-7); the obtained E_B values have been calibrated with the C 1s peak at 284.5 eV of contaminated carbon. The Cu 2p peaks show significantly separated spin-orbit components (Δ = 19.75 eV, intensity ratio = 0.508). It is possible to distinguish the oxidation states of Cu by examining satellite features of Cu $2p_{1/2}$ and Cu $2p_{3/2}$ (Fig 5-7).[25-29] There is a finite probability that an ion will be left in a slightly excited energy state after photoionization. Then kinetic energy of the emitted photoelectron is reduced to yield a shake-up peak at a higher E_B than the main peak. For Cu_2O with fully filled d orbitals (d^{10}), there are no satellite peaks because charge transfer into d states is not allowed. However, in case of CuO having a partially filled d orbital (d^9), satellite peaks can be observed as charge transfer into d states is allowed in the ground electron configuration. Both $2p_{1/2}$ and $2p_{3/2}$ peaks of Cu in CuO/Cu_2O composites have higher E_B values and broad linewidths than the respective ones in pristine Cu_2O cubes because Cu^{2+} has higher E_B values than Cu^+ and the composites contain Cu^{2+} as well as Cu^+.[26,28] The XPS spectra of Figure 5-8 provide in-depth insights into the oxidation states of copper in pristine Cu_2O cubes and CuO/Cu_2O composites. The XPS Cu $2p_{3/2}$ peak of pristine Cu_2O can be deconvoluted into two Gaussian bands arising from Cu^+ with oxygen-vacancy (Cu^+-V_O) having E_B of 930.79 eV and from Cu^+ with oxygen-lattice (Cu^+-O)

having E_B of 932.16 eV.[28,29] CuO/Cu_2O(0.3 M) composites show not only two main bands arising from Cu_2O (Cu^+-O) with E_B of 932.49 eV and CuO (Cu^{2+}-O) with E_B of 933.80 eV but also two satellite bands at 940.89 eV and 943.42 eV; two satellite peaks indicate that there are sudden changes in Coulombic potential as a photoejected electron passes through the valence band electrons of $3p_{1/2}$ (943.42 eV) and $3p_{3/2}$ (940.89 eV). Resultingly, it can be concluded that CuO/Cu_2O composites are composed of CuO and Cu_2O, being in good agreement with the above described HRTEM and XRD results.

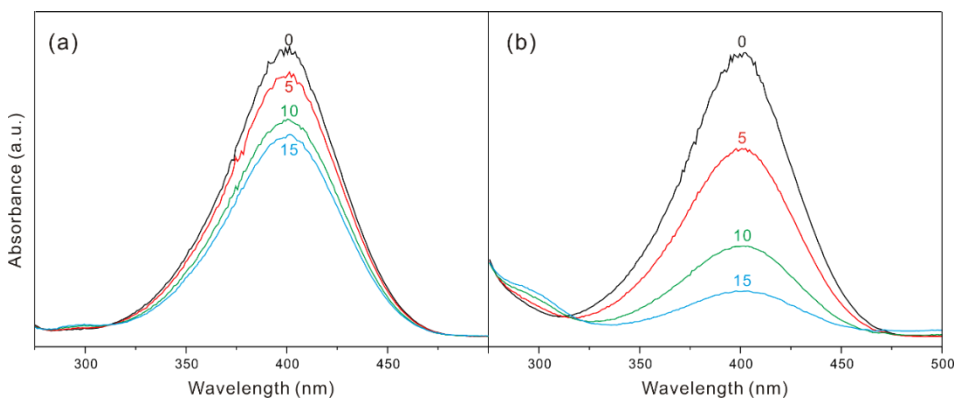

Figure 5-9 Absorption spectra at 30 ºC of $NaBH_4$-added aqueous 4-NP solutions, measured at elapsed times indicated in the units of min after adding aqueous colloidal solutions of pristine Cu_2O cubes (a) and CuO/Cu_2O(0.3 M) composites (b).

Catalytic properties of pristine Cu_2O and CuO/Cu_2O composites have been explored by monitoring absorbance changes of 4-NP via catalysts in the presence

of $NaBH_4$ (Figure 5-9). While 4-nitrophenol (4-NP) at neutral or acidic conditions shows an absorption peak at 317 nm, it is transformed to 4-nitrophenolate in alkaline conditions, resulting in a shift of the absorption peak from 317 nm to 400 nm. The absorption of 4-nitrophenolate anions at 400 nm decreases with a concomitant increase in the 295 nm peak of 4-aminophenol (4-AP) and the isosbestic point at 324 nm means the absence of any side reactions (Figure 5-9). The absorbance of 4-NP at 400 nm decreases much more rapidly with CuO/Cu_2O composites than with pristine Cu_2O cubes; 78% of 4-NP has been reduced in the presence of the composites within 15 min whereas 28% of 4-NP has been reduced with Cu_2O cubes. This suggests that the catalytic activity of CuO/Cu_2O composites is much higher than that of Cu_2O cubes.

The rate constant, k, of the catalytic reduction has been obtained from the slope of $\ln(A/A_0) = -kt$, where A and A_0 are the optical densities of 4-NP at 400 m at times t and 0 (Figure 5-10 and Table 5-2). The k values of CuO/Cu_2O composites are much higher than the k value of Cu_2O cubes, indicating that the wet etching of Cu_2O cubes with NaOH increases catalytic activity extensively. Among CuO/Cu_2O composites, CuO/Cu_2O(0.3 M) composites show the most efficient catalytic activity, suggesting that the catalytic performances of CuO/Cu_2O composites can be controlled by adjusting the concentration of NaOH(aq) during the wet etching of Cu_2O cubes. It has already been shown that a box of CuO flakes encloses a

hollow interior in CuO/Cu_2O(0.3 M) composites. This suggests that the catalytic reduction reaction takes place faster in the interior surfaces of CuO flakes than on the exterior surfaces of CuO flakes (see below). CuO/Cu_2O(0.4 M) composites having destructed structures do not have cavities anymore. Furthermore, Cu_2O cubes are re-exposed in CuO/Cu_2O(0.4 M) composites so the catalytic performances are drastically reduced; as Cu_2O is a p-type semiconductor, electrons hardly transfer from one species to another on its surface under ambient conditions.[19-20] Furthermore, whereas metal oxides possessing d^9 electronic configuration are active for the reduction of 4-NP, metal oxides with d^{10} configuration are found to be inactive, meaning that pure Cu_2O is not catalytically acting for the reduction of 4-NP.[13,19] Overall, the catalytic activity of CuO/Cu_2O composites depends highly on their morphologies, which have been varied by adjusting the concentrations of NaOH during the wet etching of Cu_2O cubes.

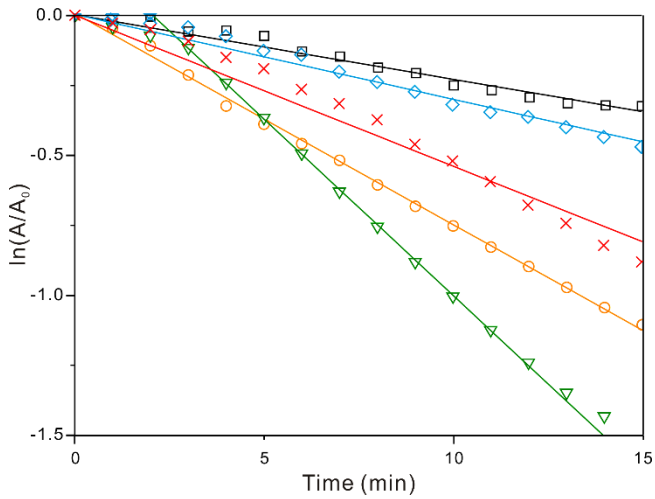

Figure 5-10 ln(A/A$_0$) vs t for the catalytic reduction of 80 μM 4-NP(aq) in the presence of 2.0 mM $NaBH_4$ at 30 ºC, via pristine Cu_2O cubes (squares) and CuO/Cu_2O composites prepared at NaOH concentrations of 0.1 M (crosses), 0.2 M (circles), 0.3 M (triangles), and 0.4 M (diamonds).

Table 5-2 Rate constants (k) at 30 ºC, activation energies (E_a), frequency factors (A), activation enthalpies ($\Delta H^{\ddagger}$), and activation entropies ($\Delta S^{\ddagger}$) for the catalytic reduction of 4-NP

Catalyst	k (min^{-1})	E_a (kcal mol^{-1})	A (min^{-1})	$\Delta H^{\ddagger}$ (kcal mol^{-1})	$\Delta S^{\ddagger}$ (cal mol^{-1} K^{-1})
pristine Cu_2O	0.023	27.0	6.63×10^{17}	110.6	12.9
CuO/Cu_2O (0.1 M)	0.064	23.3	3.82×10^{15}	95.0	2.6
CuO/Cu_2O (0.2 M)	0.075	21.9	4.30×10^{14}	89.2	-1.8
CuO/Cu_2O (0.3 M)	0.126	19.6	1.46×10^{13}	79.5	-8.5
CuO/Cu_2O (0.4 M)	0.037	22.7	8.18×10^{14}	108.4	12.3

A certain period of time, so called the induction time,[4-8] is required to initiate the catalytic reaction of CuO/Cu_2O(0.3 M) composites. Meanwhile, none of pristine Cu_2O cubes and the other CuO/Cu_2O composites show the induction time because none of them have hollow interiors. The induction time is attributed to the diffusion time required for reactant molecules to be adsorbed on active sites.[4-8] Even though a certain period is needed to start the reaction, the overall catalytic process is much faster via CuO/Cu_2O(0.3 M) composites than via any other catalysts. Overall, catalytic activity is dependent strongly on the structures of CuO/Cu_2O composites and it is most efficient for CuO/Cu_2O(0.3 M) composites, which have hollow cavities, suggesting that the catalytic reduction of 4-NP molecules takes place most rapidly in cavities surrounded by the walls of CuO flakes.

Figure 5-11 presents the temperature-dependent first-order reduction profiles of 4-NP catalyzed via Cu_2O cubes and CuO/Cu_2O(0.3 M) composites in the presence of $NaBH_4$. The rate constants of reactions carried out at different temperatures have been calculated, revealing that the catalytic performances of catalysts become enhanced as the reaction temperature increases. So, we can conclude the catalytic reduction of 4-NP via Cu_2O cubes or CuO/Cu_2O composites is an activated process (see below). As mentioned above with Figure 6, a certain period of time was required only for CuO/Cu_2O(0.3 M) composites. The induction time decreases gradually with the increase of the reaction temperatures. The activation energy of

the induction process has been estimated as 15.3 kcal mol^{-1} by using an Arrhenius plot. This suggests that the penetration of reactants through walls of CuO flakes requires overcoming a considerable energy barrier.[5] After the induction time, the reaction follows pseudo-first-order kinetics and the slope gives the rate constant of the catalytic reaction. The results indicate that the catalytic reduction of 4-NP molecules takes place fast in the hollow interior of CuO/Cu_2O(0.3 M) composites.

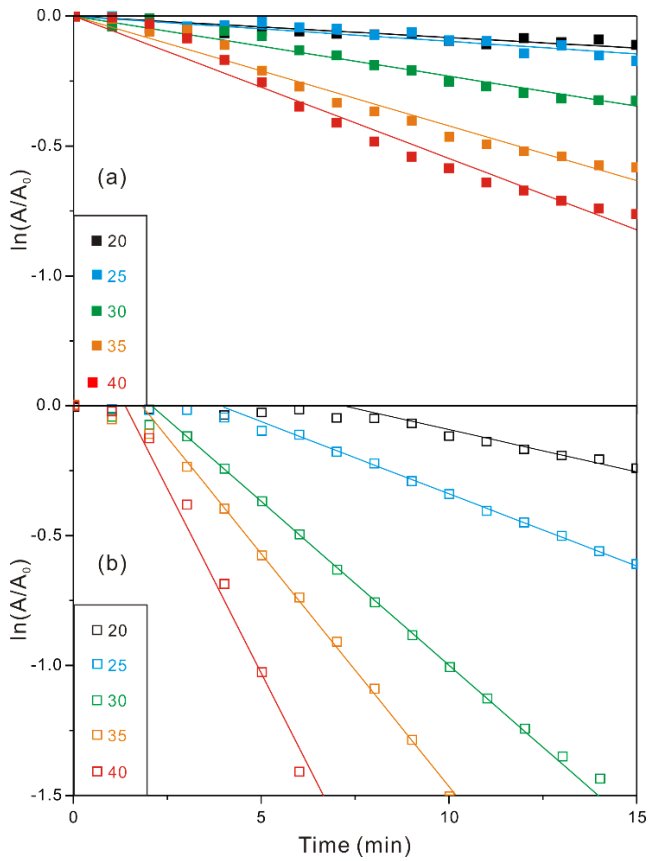

Figure 5-11 First-order kinetics, ln(A/A_0) vs t, for the catalytic reduction of 80 µM 4-NP(aq) in the presence of 2.0 mM $NaBH_4$ at temperatures indicated in ºC via pristine Cu_2O cubes (a) and CuO/Cu_2O(0.3 M) composites.

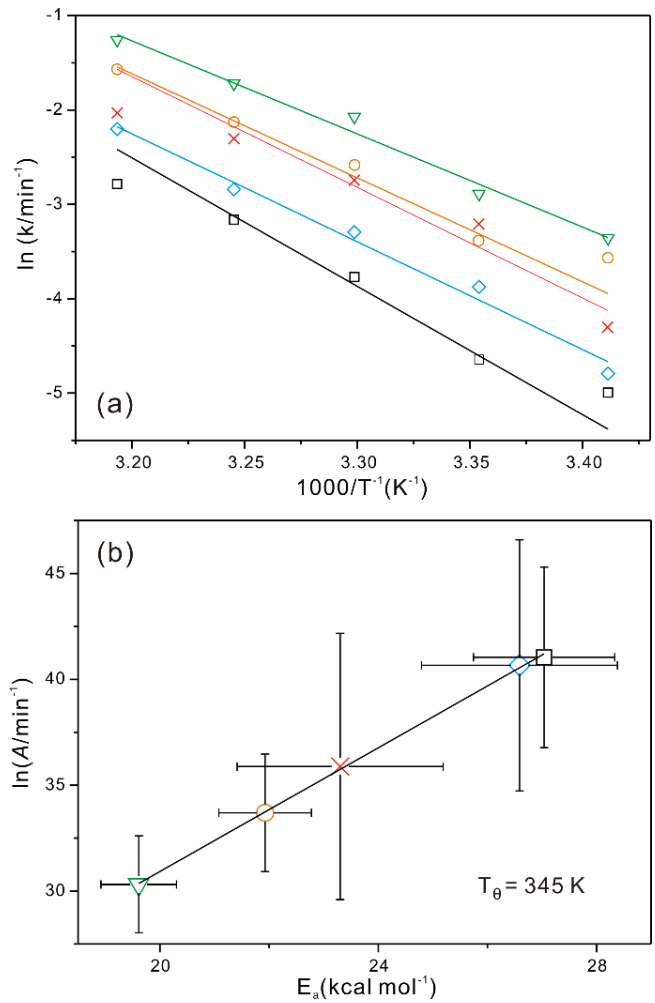

Figure 5-12 Arrhenius plots for the catalytic reduction reaction of 80 µM 4-NP(aq) in the presence of 2.0 mM $NaBH_4$ via pristine Cu_2O cubes (squares) and CuO/Cu_2O composites prepared at NaOH concentrations of 0.1 M (crosses), 0.2 M (circles), 0.3 M (triangles), and 0.4 M (diamonds) (a), and compensation law plot of the activation energies and the frequency factors obtained from the Arrhenius plots (b).

Arrhenius plots have been applied to extract the activation energies (E_a) and frequency factors (*A*) of 4-NP reduction catalyzed via Cu_2O cubes and CuO/Cu_2O composites (Figure 5-12a). Table 5-2 shows that the E_a (19.6 kcal mol^{-1}) and *A* ($1.46x10^{13}$ min^{-1}) of CuO/Cu_2O(0.3 M) composites with cavities are much smaller than the respective ones of any other catalysts without hollow interiors. As discussed above with Figs. 5-10 and 5-11, this also supports that the catalytic reduction reaction takes place much faster in the inner walls of CuO flakes than on the outer surfaces of CuO flakes because confinement effects reduce the energy barrier. During the wet etching of Cu_2O cubes with 0.4 M NaOH(aq), enclosed Cu_2O cubes are re-exposed to hinder the efficient catalytic reduction of 4-NP via CuO flakes, as mentioned above. As a result, E_a becomes large again so the reduction reaction slows down to yield a small k value.

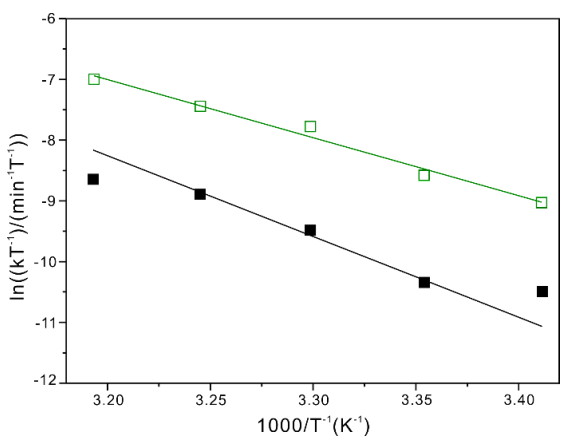

Figure 5-13 Eyring plot for the catalytic reduction reactions of 80 μM 4-NP(aq) catalyzed via pristine Cu_2O cubes (closed) and CuO/Cu_2O(0.3 M) composites (open) in the presence of $NaBH_4$.

The Eyring plots of temperature-dependent rate constants have been used to calculate activation enthalpies ($\Delta H^{\ddagger}$) and activation entropies ($\Delta S^{\ddagger}$) for catalytic reduction reactions via as-prepared catalysts (Fig 5-13 and Table 5-2). The results indicate that among as-prepared catalysts, CuO/Cu_2O(0.3 M) composites have the smallest $\Delta H^{\ddagger}$ (79.5 kcal mol^{-1}) and the smallest $\Delta S^{\ddagger}$ (-8.5 cal mol^{-1} K^{-1}), suggesting that the formation of the activated complex for the catalytic reduction reaction via CuO/Cu_2O(0.3 M) composites is most favorable in energy but most unfavorable in degree of freedom.[8] Thus, these results suggest that the most efficient catalytic reduction of CuO/Cu_2O(0.3 M) composites with the smallest E_a value can be attributed to the energetically most favorable formation of the activated complex within the hollow interior of a CuO/Cu_2O(0.3 M) composite.[4-8] As expected, the catalytic activity of CuO/Cu_2O(0.4 M) composites have been deteriorated rapidly to have $\Delta H^{\ddagger}$ of 108.4 kcal mol^{-1}, which is rather close to $\Delta H^{\ddagger}$ of pristine Cu_2O cubes. Our results suggest that the most efficient catalytic performance and the smallest E_a value of CuO/Cu_2O(0.3 M) composites can be attributed to the energetically most favorable formation of the activated complex within a cavity confined by CuO flakes. Overall, Figure 5-12a and Table 5-2 have also revealed that the catalytic activity depends on the morphologies of CuO/Cu_2O composites, which can be controlled by adjusting the concentration of NaOH during the wet etching of Cu_2O cubes. In particular, CuO/Cu_2O(0.3 M) composites with hollow interiors show the

most efficient catalytic performance for the reduction reaction of 4-NP.

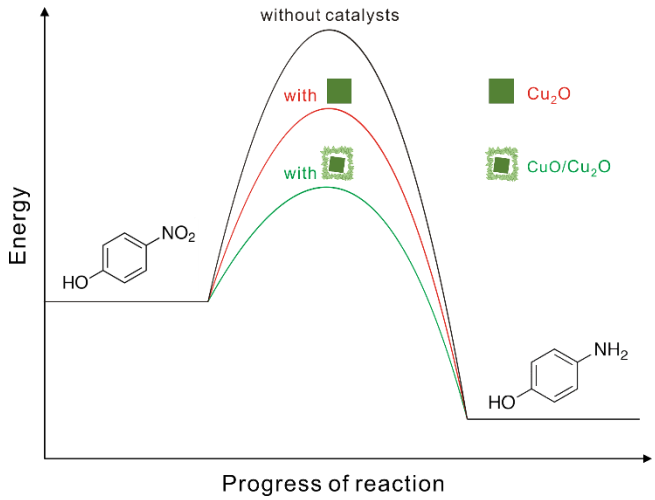

Figure 5-14 Schematically proposed mechanism for the catalytic reduction of 4-NP via CuO/Cu_2O composites in the presence of $NaBH_4$.

Fig 5-12b shows the compensation law plot of $\ln A = \alpha + E_a/(RT_\theta)$,[4-8] where α is a constant and T_θ is called the fictitious isokinetic temperature; theoretically, the catalytic rates of all the catalysts become equal at T_θ. In our experiment, the empirical linear relationship demonstrates the compensation effect in our catalytic systems, where T_θ is 345 K. The compensation effect is related with a switching from a regime where the overall rate is controlled by the activation of the reactant to a regime where the stability of the product becomes more important. Thus, we deduce that for the reduction reactions via CuO/Cu_2O composites with cavities, E_a

is lower while the lower density of active sites is compensated largely by stability of adsorption. Resultingly, CuO/Cu_2O composites act as electron-relaying catalysts for the reduction reaction of 4-NP in the presence of $NaBH_4$. With respect to the most efficient catalytic activity of CuO/Cu_2O(0.3 M) composites, the confinement effect of CuO boxes with hollow interiors is considered to expedite electron relays from BH_4^- to 4-NP extensively by reducing E_a considerably, as shown in Figure 5-14.

5.5 Conclusions

CuO/Cu_2O composites having good catalytic properties for 4-NP reduction have been produced facilely by the wet etching of Cu_2O cubes at various concentrations of NaOH. The catalytic activity of CuO/Cu_2O composites is found to depend highly on their morphologies; in particular, CuO/Cu_2O(0.3 M) composites have shown the strongest catalytic performances for the reduction of 4-NP. Results have indicated that oxidation etching enhances the catalytic performances of Cu_2O cubes extensively without having any noble metals via forming CuO/Cu_2O composites. Furthermore, the catalytic activity of CuO/Cu_2O composites can be optimized by controlling their morphologies. Regarding to the highest catalytic activity of

CuO/Cu_2O(0.3 M) composites with cavities surrounded by CuO flakes, confinement effect is considered to expedite electron transfer from BH_4^- to 4-NP enormously by reducing E_a largely; the energetically favorable formation of the activated complex at the inner walls of a CuO box lowers the energy barrier substantially. In summary, CuO/Cu_2O composites having high catalytic activity for 4-NP reduction have been prepared facilely via a controlled oxidation process of Cu_2O cubes. We consider that our prepared CuO/Cu_2O composites can be applied to treat wastewater in an inexpensive way without employing commonly used noble-metal catalysts.

5.6 Acknowledgements

This work was supported by research grants through the National Research Foundation of Korea funded by the Korea government (2014-057382 and 2015-051798).

5.7 References

[1] Kim, Y., Kim, H.-B., Jang, D.-J, *J. Mater. Chem. A*, **2014**, 2, 5791.

[2] Kim, H.-B., Jeong, D.-W., and Jang, D.-J, *CrystEngComm*, **2016**, 18, 898.

[3] Pozun, Z. D., Rodenbusch, S. E., Keller, E., Tran, K., Tang, W., Stevenson, K. J., Henkelman, G, *J. Phys. Chem. C*, **2013**, 117, 7598.

[4] Kwak, J.-A., Lee, D. K., and Jang, D.-J, *Appl.Catl.B: Environ*., **2013**, 142, 323.

[5] Son, M., Lee, J., and Jang, D.-J, *J. Mol. Catal. A: Chem*., **2014**, 385, 38.

[6] Lee, H., Kwak, J.-A., and Jang, D.-J, *J. Phys. Chem. C*, **2014**, 118, 22792.

[7] Lee, J., Han, K., and Jang, D.-J, *Appl. Catal. A: Gen*., **2014**, 469, 380.

[8] Lee, J., and Jang, D.-J, *J. Phys. Chem. C*, **2016**, 120, 4130.

[9] Pal, J., Mondal, C., Sasmal, A. K., Ganguly, M., Negishi, Y., and Pal, T, *ACS Appl. Mater. Interfaces*, **2014**, 6, 9173.

[10] Zhang, L., Jing, D., Guo, L., & Yao, X, *ACS Sustainable Chem. Eng*., **2014**, 2, 1446.

[11] Yao, W., Li, F.-L., Li, H.-X., and Lang, J.-P, *J. Mater. Chem. A*, **2015**, 3, 4578.

[12] Guo, X., Ma, J., and Ge, H, *Russ. J. Phys. Chem. A*, **2015**, 89, 1374.

[13] Sasmal, A. K., Dutta, S., and Pal, T, *Dalton Trans*., **2016**, 45, 3139.

[14] Kuo, C.-H., Chen, C.-H., and Huang, M. H, *Adv. Funct. Mater*., **2007**, 17, 3773.

[15] Ho, J.-Y., and Huang, M. H, *J. Phys. Chem. C*, **2009**, 113, 14159.

[16] Kuo, C.-H., and Huang, M. H, *Nano Today*, **2010**, 5, 106.

[17] Sun, S., and Yang, Z, *Chem. Commun.*, **2014**, 50, 7403.

[18] Chen, L., Zhang, Y., Zhu, P., Zhou, F., Zeng, W., Lu, D. D., and Wong, C, *Sci. Rep*., **2015**, 5, 9672.

[19] Mandlimath, T. R., and Gopal, B, *J. Mol. Catal. A: Chem*., **2011**, 350, 9.

[20] Ma, Y., Ni, Y., Guo, F., and Xiang, N, *Cryst. Growth Des.*, **2015**, 15, 2243.

[21] Qu, X., Alvarez, P. J., and Li, Q, *Water research*, **2013**, 47, 3931.

[22] T. Aditya, A. Pal and T. Pal, Chem. Commun., 2015, **51**, 9410.

[23] Zhang, L., Cui, Z., Wu, Q., Guo, D., Xu, Y., and Guo, L, *CrystEngComm*., **2013**, 15, 7462.

[24] Park, J. C., Kim, J., Kwon, H., and Song, H, *Adv. Mater*., **2009**, 21, 803.

[25] Poulston, S., Parlett, P., Stone, P., and Bowker, M, *Surf. Interface Anal*., **1996**, 24, 811.

[26] Gan, Z., Yu, G., Tay, B., Tan, C., Zhao, Z., and Fu, Y, *J. Phys. D: Appl. Phys*., **2003**, 37, 81.

[27] Diaz-Droguett, D. E., Espinoza, R., and Fuenzalida, V, *Appl. Surf. Sci*., **2011**, 257, 4597.

[28] Monte, M., Munuera, G., Costa, D., Conesa, J. C., and Martínez-Arias, A, *Phys. Chem. Chem. Phys*., **2015**, 17, 29995.

[29] Kozak, D. S., Sergiienko, R. A., Shibata, E., Iizuka, A., and Nakamura, T, *Sci. Rep*., **2016**, 6, 21178.

Appendices

A.1. List of publications

[1] **Dayeon Choi**, Ji-young Pyo, Yeonho Kim, and Du-Jeon Jang "Facile synthesis of composition-gradient $Cd_{1-x}Zn_xS$ quantum dots by cation exchange for controlled optical properties" *J. Mater. Chem. C*, **2015**, *3*, 3286-3293.

[2] **Dayeon Choi**, Ji-young Pyo, and Du-Jeon Jang "Impurity location-dependent relaxation dynamics of Cu:CdS quantum dots" *Nanoscale Res. Lett.*, **2017,** *12*, 1-8.

[3] **Dayeon Choi** and Du-Jeon Jang "Facile fabrication of CuO/Cu_2O composites with high catalytic performances" *New J. Chem.*, **2017,** *41*, 2964-2972.

[4] **Dayeon Choi**, Sooho Ham, and Du-Jeon Jang "Visible-light photocatalytic reduction of Cr(VI) via carbon quantum dots-decorated TiO_2 nanocomposites" *J. Environ. Chem. Eng.*, **2018,** *6*, 1-8.

[5] **Dayeon Choi** and Du-Jeon Jang "Photodeposition of gold nanoparticles on silica nanospheres using carbon dots as excellent electron donors" *New J. Chem.*, **2018,** *42(18)*, 14717-14720. [IF : 3.201]

[6] Jaewon Lee, Sooho Ham, **Dayeon Choi**, and Du-Jeon Jang "Facile fabrication of porous ZnS nanostructures with controlled amount of S vacancies for enhanced photocatalytic performances" *Nanoscale*, **2018,** *10*,

14254-14263.

[7] Sooho Ham, **Dayeon Choi**, and Du-Jeon Jang "Photodeposition of gold nanoparticles on ZnS nanobelts for enhanced dye decomposition" *Materials Research Bulletin*, **2018**.

[8] **Dayeon Choi**, Sooho Ham, and Du-Jeon Jang " Au-C/SiO_2 nanocomposites with enhanced peroxidase-like activity for colorimetric and fluorometric detection of hydrogen peroxide" *New J. Chem.*, **2018, in progress**

A.2. List of presentations

A.2.1. International presentations

[1] Dayeon Choi, Ji-Young Pyo, Yeonho Kim, and Du-Jeon Jang "Composition-Gradient $Cd_{1-x}Zn_xS$ Quantum Dots with Enhanced Optical Properties" International Union of Pure and Applied Chemistry, General Assembly, Busan, Korea **(2015)**.

[2] Dayeon Choi, Ji-Young Pyo, Yeonho Kim, and Du-Jeon Jang "Facile synthesis of composition-gradient $Cd_{1-x}Zn_xS$ quantum dots by cation exchange for controlled optical properties" The International Chemical Congress of Pacific Basin Societies 2015, Honolulu, Hawaii, USA **(2015)**.

[3] Dayeon Choi, Ji-Young Pyo, Hyung-Bae Kim, and Du-Jeon Jang "Structure-Dependent Relaxation Dynamics of Cu:CdS Nanocrystals" Gordon Research Conference – Structural Nanomaterials, Hong Kong, China **(2016)**.

A.2.2. Domestic presentations

[1] Dayoen Choi, Yeonho Kim, and Du-Jeon Jang "Synthesis of Composition-Gradient $Cd_{1-x}Zn_xS$ Quantum Dots by Facile Cation Exchange to Controlled Their Optical Properties" The 113rd Korea Chemical Society, Goyang, Korea (**2014**).

[2] Dayeon Choi and Du-Jeon Jang "Cation Exchange of CdS Quantum Dots to Control Optical Properties" The 115th Korea Chemical Society, Goyang, Korea (**2015**).

[3] Dayeon Choi and Du-Jeon Jang "Fabrication of Hierarchical Hollow Cu_2O-CuO Composites with Well-Designed Structures to Enhance Their Catalytic Performances" The 116th Korea Chemical Society, Daegu, Korea (**2015**).

[4] Dayeon Choi and Du-Jeon Jang "Carrier Relaxation Dynamics of Cu:CdS Quantum Dots" The 117th Korea Chemical Society, Goyang, Korea (**2016**).

[5] Dayeon Choi and Du-Jeon Jang "Cu_2O/CuO Composites Designed for Wastewater Treatment" The 119th Korea Chemical Society, Goyang, Korea (**2017**).

Abstract (Korean)

탄소점을 기반으로 하는 하이브리드 나노물질의 합성하고 응용하는 연구를 하였다. 수열 방법으로 손쉽게 합성한 탄소점을 TiO_2 와 SiO_2와 같은 반도체 나노물질에 접합시켜 하이브리드 나노구조를 만들었다. 도입된 탄소점은 광촉매 시스템에서 광 증감제 역할을 하였고, 광증착 시스템에서는 전자주개 역할을 하였다. 또한 구조를 조절한 산화구리복합체를 합성하고 구조에 따른 촉매효율을 조사해 보았다. 1장에서는 사이즈에 따라 달라지는 나노사이즈 물질에 대해 간략히 설명하였다. 특히 반도체가 벌크 사이즈일 때와 비교하여 나노사이즈에서만 보이는 광학적 특성에 대해 기술하였다. 또한 탄소점의 특징과 다양한 합성법, 응용분야를 서술하였다.

2 장에서는 탄소점-이산화타이타늄 나노복합체 (C/TiO_2 nanocomposites)를 탄소점을 수열방법으로 합성하고 탄소점 양에 따른 크롬6가 환원 광촉매 실험에 응용하였다. 가시광영역의 빛 조사 하에 크롬6가 환원 광촉매 효율은 도입된 탄소점의 양과 큰 상관 관계가 있음을 밝혀냈다. 탄소점이 가시광 영역의 빛에 여기되어 생성된 전자는 탄소양자점에서 TiO_2의 전도띠로 옮겨 가고, 옮겨진 전자는 순차적으로 크롬 6가 이온을 크롬 3가 이온으로 환원시킨다. Dyade

구조를 가진 이 복합체에서 탄소점은 TiO_2가 가시광 영역에서 감응 할 수 있도록 하는 광증감제 역할을 하였으며 합성된 C/TiO_2 나노복합체는 크롬 6가의 효율적으로 환원시키는 광촉매 시스템임이 밝혀졌다. 개발된 C/TiO_2 나노복합체는 어떠한 환원제 없이 태양빛을 사용하여 산업폐수를 경제적인 방법으로 정화시키는데 응용 될 수 있을 것이다.

3 장에서는 탄소양자점을 이산화규소에 수열방법으로 도입하여 Cdots-SiO_2 nanocomposites을 합성하고, 금 나노입자를 표면위에 직접적으로 광증착 하여 Au/Cdots-SiO_2 nanocomposites룰 최종적으로 합성하였다. 빛이 조사되면 탄소점에서 발생하는 전자는 금 전구체 $AuCl_4^-$ 를 SiO_2 표면에서 환원시킨다. 이때 탄소점은 전자주개와 반응사이트 역할을 통시에 수행한다. 부도체인 SiO_2 표면에 탄소양자점을 전자 주개와 반응사이트로써 도입한 이 방법은 기반물질의 광 반응 여부에 관계 없이 금속-반도체 하이브리드 나노구조체를 합성하는 효율적인 방법임을 밝혀냈다.

4 장에서는 앞장에서 합성한 Au/Cdots-SiO_2 nanocomposites의 과산화효소(peroxidase)로써의 응용과 과산화수소의 기질 3,3',5,5'-tetramethylbenzidine를 활용하여 수용액 상의 과산화수소를 색검출 법으로 검출하는 센서로의 응용에 대해 서술하였다. 또한 표면에 광증착된 금 나노입자가 탄소점의 빛흡수체 역할을 하기때문에, 과산화

수소에 의해 금 나노입자를 식각시키게 되면 탄소점의 형광 세기의 변화가 생기게 된다. 다시 말해, Au/Cdots-SiO_2 nanocomposites를 이용하여 수용액 상의 과산화 수소 농도를 색과 형광세기 두가지를 이용하여 감지 가능하다. 따라서 다양한 검출분야, 촉매, 임상진단등의 분야에 응용 가능함을 서술 하였다.

5 장에서는 다양하게 구조를 변화시킨 산화구리 복합체를 합성하고 환원제 첨가하에 4-나이트로페놀 촉매실험을 했다. 촉매효율은 산화구리 복합체의 구조에 크게 영향을 받는 결과를 보였다. 표면을 감싸고 있는 산화구리 조각들은 내부 산화구리 지지체와 함께 제한효과를 일으켜 활성화 에너지를 크게 낮춰 BH_4^- 에서 4-나이트로페놀 분자로의 전자 이동을 용이하게 하는 것으로 밝혀졌다. 결과적으로 이 연구를 통해 구조제어된 산화구리 복합체는 일반적으로 쓰이는 귀금속 촉매를 대신하여 폐수처리 촉매로 이용 가능함을 기술하였다.

주요어: 탄소점, 금 나노입자, 하이브리드 나노구조, 광촉매, 광증착

학번: 2013-22943